DEVELOPING TOOLS FOR PAPER-BASED CULTURES TO INTERROGATE OXYGEN'S ROLE IN CANCER PROGRESSION

Matthew William Boyce

A dissertation submitted to the faculty at University of North Carolina at Chapel Hill in partial fulfillment of the requirements for the degree of Doctor of Philosophy in the Department of Chemistry in the School of Arts and Sciences.

Chapel Hill
2018

Approved by:

Matthew Lockett

Jim Jorgenson

Amanda Hummon

Gary Glish

Glenn Walker

ABSTRACT

Matthew William Boyce: Developing tools for paper-based cultures to interrogate oxygen's role in cancer progression
(Under the direction of Matthew R. Lockett)

Oxygen contributes to cellular phenotypes and invasiveness through hypoxia-inducible transcription factors. These factors, which induce signaling pathways at low-oxygen tensions, are involved with the maintenance of healthy tissue and the progression of cancer. Poor vascularization within rapidly growing tumors leads to the production of atypical gradients of oxygen. Cells experiencing these gradients develop into heterogeneous populations and develop increasingly aggressive phenotypes. To better understand the relationship between extracellular oxygen tension and cancer cell phenotype, *in vitro* models are needed that can easily relate these variables while providing experimental control over the environment.

Paper-based cultures (PBCs) are an emerging platform capable of generating thick, tissue-like constructs of cells by stacking cell-laden paper scaffolds. Controlling the diffusion of medium into these cultures results in the formation of oxygen, nutrient, and waste gradients through diffusion-consumption mechanisms similar to tumorous tissue. After prolonged incubation, these cultures can be peeled apart into individual scaffolds analyzed. The ease of generating gradients and disassembling the cultures into individual layers makes this platform well suited comparing cell phenotype local oxygen environment.

In this work, PBCs were used to explore the relationship between oxygen gradients and cancer chemosensitivity. Quantification of oxygen gradients within PBCs was performed using luminescent oxygen-sensors. These sensors were developed and characterized, then used to measure oxygen gradients in PBCs containing different densities of a colon carcinoma cell line, HCT-116. Dosing these cultures with a cytotoxic molecule, SN-38, showed regional differences in chemosensitivity, with hypoxic cells exhibiting increased chemoresistance.

In addition to studying gradients in PBCs, I also fabricated a fluidic device capable of generating oxygen gradients across static three-dimensional (3D) cultures. The PBCs used to date were unable to generate oxygen gradients across the culture without also generating concurrent gradients of nutrients and waste products. With this device, oxygen gradients can be decoupled from nutrient and waste gradients. These oxygen gradients are imposed on the cultures and are not dictated by cellular consumption.

The culmination of my doctoral work is a suite of tools and sensors that enable the quantitative study of cellular phenotype in three-dimensional cultures relative to the cell's local oxygen environment.

To my family, friends, and mentors who have helped me through this journey.

Thank you for your support.

ACKNOWLEDGEMENTS

I would like thank the many people who have made this work possible. Chief amongst them is my advisor, Dr. Matthew Lockett, who has provided thoughtful guidance throughout my graduate career. Thank you for challenging me to grow as a scientist and providing me the freedom to explore research topics that I found interesting. I also want to acknowledge our collaborator, Dr. Amanda Hummon, and her graduate student, Gabe LaBonia, who have significantly contributed to research presented in this dissertation.

I would like to thank Eli Lilly, the Eastman Chemical Company, and the UNC Graduate School for helping fund this research. In addition, I want to recognize the Chapel Hill Analytical and Nanofabrication Lab (CHANL), Microscopy Services Laboratory (MSL), and UNC Be A Maker (BEAM) facilities, all of which provided the necessary resources to conduct this research.

Thank you to my undergraduate research advisors Dr. Maury Howard, Dr. John Molloy, and Dr. Phillip Rock for introducing me to research and putting me on this path in life.

Thank you to the members of the Lockett lab for providing thoughtful discussions, assistance with scientific ventures, and comradery throughout my time at UNC. Specifically, I would like to thank Rachael Kenney, who has helped me with a number of research projects and whose friendship has been a boon throughout graduate school.

I would like to thank my family, whose continued support has made this possible. And I want to especially thank Kelsey Miller, whose support, friendship, encouragement, and overall silliness have been a beacon. I look forward to our continued adventures.

TABLE OF CONTENTS

LIST OF TABLES

LIST OF FIGURES

LIST OF ABBREVIATIONS AND SYMBOLS

ºC	Degree(s) Celsius
$[O_2]$	Concentration of oxygen
2D	Two-dimensional
3D	Three-dimensional
7-AAD	7-aminoactinomycin D
$\frac{\partial C}{\partial x}$	Partial derivative of concertation with respect to x-axis
µg	Microgram(s)
µL	Microliter(s)
µm	Micrometer(s)
µM	Micromolar
ρ	Corrected volumetric density
ABC	ATP-binding cassette protein
ABS	Acrylonitrile styrene
ANOVA	Analysis of variance
ATCC	American type cancer collection
ATP	Adenosine triphosphate
BLOCC	Block-layered oxygen-controlling chip
CAIX	Carbonic anhydrous 9
cc	Cubic centimeters
cm	Centimeter(s)
cm^2	Centimeters squared

CO_2	Carbon dioxide
CTG	CellTiter-Glo™
CXCR4	Chemokine receptor 4
D	Diffusion coefficient
DMSO	Dimethyl sulfoxide
DNA	Deoxyribonucleic acid
EDTA	Ethylenediaminetetraacetic acid
eGFP	Enhanced green fluorescent protein
ELISA	Enzyme-linked immunosorbent assay
EMT	Epithelial-to-mesenchymal transition
FDA	Fluorescein diacetate
FIJI	FIJI Is Just ImageJ
GFP	Green fluorescent protein
GLUT1	Glucose transporter 1
h	Length
h, hr	Hour(s)
HCT116-mCHR	HCT-116 cells engineered with an mCHR vector
HIF	Hypoxia-inducible factor
HRE	Hypoxia-responsive element
I_0	Sensor intensity in the absence of oxygen
$I_=$	Sensor intensity in the presence of oxygen
IC_{50}	Half maximal inhibitory concertation
IHC	Immunohistochemistry

in	Inch
Ir(II)	Iridium ion
J_{in}	Flux in
J_{out}	Flux out
K_{sv}	Stern-Volmer constant
LED	Light-emitting diode
LOQ	Limit of quantitation
M231	Parental MDA-MB-231 cells
M231-eGFP	MDA-MB-231 cells engineered with an eGFP vector
M231-HRE	MDA-MB-231 engineered with the 5HRE/GFP vector
M231-mCHR	MDA-MB-231 cells engineered with an mCHR vector
mCHR	mCherry
MDR	Multidrug resistance
min	Minute(s)
mL	Milliliter(s)
mm	Millimeter(s)
mM	Millimolar
mmHg	Millimeters mercury
MMP2	Matrix metalloproteinase 2
mol	Mole(s)
ms	Millisecond(s)
MTT	3-(4,5-dimethylthiazol-2-yl)-2,5-diphenyltetrazolium bromide
MW	Molecular weight

N_2	Diatomic nitrogen
nm	Nanometer(s)
nM	Nanomolar
O_2	Diatomic oxygen
OEP	Octaethylporphyrin
OEPK	Octaethylporphyrin ketone
PBC	Paper-based culture
PBS	Phosphate buffer saline
Pd(II)	Palladium ion
PDMS	Polydimethylsiloxane
PdTFPP	Palladium (II) tetrakis(pentafluorophenyl)porphyrin
PET	Polyethylene terephthalate
pH	-log of hydronium ion concertation
PI	Propidium iodide
PMMA	Poly(methyl methacrylate)
ppi	Pulses per inch
PS	Polystyrene
Pt(II)	Platinum ion
PVC	Poly(vinyl chloride)
Q	Cellular oxygen consumption rate
qPCR	Quantitative polymerase chain reaction
ROI	Region of interest
rpm	Rotations per minute

RPMI	Roswell Park Memorial Institute
Ru(II)	Ruthenium ion
SD	Standard deviation
sec	Second(s)
SEM	Standard error of the mean
SN-38	7-ethy-10-hydroxy-camptothecin
t	Time
TME	Tumor microenvironment
UV	Ultraviolet
v/v	Volume to volume ratio
VEGF	Vascular endothelial growth factor
w/w	Weight to weight ratio

CHAPTER 1: ADAPTING PAPER-BASED CULTURES AS A TUMOR MODEL

Oxygen concentrations within the tumor microenvironment play a critical role in the growth, survival, and eventual metastasis of cancers.[1–3] Despite the decades of research showing oxygen's role in cancer progression, translating *in vitro* findings to *in vivo* behavior has been difficult due to a reliance on two-dimensional (2D) cell culture models.[4] While these models provide a convenient and high-throughput platform for studying cancer biology, they fail to replicate the complex three-dimensional (3D) physiochemical environments within tumors.[5,6] To better recapitulate the tumor environment and improve the biological relevancy of *in vitro* studies, 3D cultures have been developed that emulate the diffusion-limited environment of tumors.[7,8] By reproducing the mass-transport limitations found within poorly vascularized tumors, hydrogel slab and multicellular tumor spheroid cultures promote the formation of heterogeneous cell populations whose phenotypes are determined by their chemical environment.[9,10] Unfortunately, isolating these phenotypically distinct populations of cells from three-dimensional cultures is difficult, and often requires laborious histological sectioning which prevents recovery of live cell populations for continued culture or downstream analyses. Paper-based cultures (PBCs) are an emerging cell culture platform that can overcome the limitations of current 3D models by providing a novel approach towards culture construction and deconstruction.[11] In PBCs, tissue-like cultures are constructed by stacking call-laden paper scaffolds. After prolonged incubation, cell populations are separated by simply peeling apart the

paper scaffolds. Isolated cell populations can then be recovered for further culturing or used in a number of downstream analyses.

To outline the motivation for this dissertation, this chapter will describe the role oxygen plays in cancer progression and common approaches for generating oxygen gradients in culture systems. The chapter will also cover the application of paper-based culture for studying cancer and highlight methods for interrogating cellular responses for down-stream assays.

1.1 Oxygen and cancer progression

The development of malignant tumors and subsequent invasion to secondary sites (i.e., metastasis) is estimated to be responsible for 90% of cancer-associated deaths.[12] To develop strategies that mitigate cancer-related deaths, cellular and environmental mechanisms that affect tumorigenesis must be understood at both the molecular and cellular level. Initiation of tumors begins with the accumulation of genetic mutations that lead to uncontrolled proliferation, ultimately allowing a mutated cell to propagate into a large mass of cells (Fig. 1.1).[13] If left unchecked, these cells will develop a unique microenvironment, known as the tumor microenvironment (TME). This environment is poorly vascularized and provides environmental conditions necessary to promote the development of a metastatic phenotype.[14–16] Though genetic dysregulation is understood as the underlying mechanism that initiates cancer, understanding the TME is vital for understanding the progression of cancer towards malignancy.

1.1.1 Tumor microenvironment

The TME is composed of a diverse mixture of cellular and non-cellular components that contribute to the progression of cancer. Cellular elements include vascular endothelial cells,

infiltrating immune cells, and cancer-associated fibroblastic cells.[17] The vascular endothelial cells help modulate cancer cell invasion[18] and take part in angiogenesis, which provides nutrients to maintain tumor growth[19] and vasculature for cancer dissemination.[20] Infiltrating immune cells recruited by the tumor produce cytokines that act as immunosuppressers and allow tumors to escape immune destruction.[21] Fibroblasts remodel the extracellular matrix to promote cellular growth and survival,[22] and release cytokines that recruit immune cells and direct cellular invasion.[23,24]

Non-cellular elements of the TME include the evolving extracellular matrix and atypical gradients of ambient metabolites (e.g., glucose and oxygen), signaling factors, and waste products. Of the non-cellular elements present within tumors, atypical gradients play a significant role in tumor progression by applying spatially distinct selection pressures.[25] These pressures lead to the development of heterogeneous populations of cells and promote the development of a metastatic phenotype.[26,27]

The formation of these atypical gradients within the tumor is the result of an imbalance between cellular growth and tumor vascularization: rapid cellular proliferation outpaces angiogenesis and leads to cellular metabolism outpacing diffusional delivery of nutrients. The inability of vasculature to adequately sustain tumor growth results in regions of depleted nutrients (glucose and oxygen) and accumulated waste products. Of the metabolites found within the TME, oxygen has been of particular interest in cancer progression research due to its role in reprogramming metabolism towards anaerobic respiration,[28] promoting genetic instability,[29] and instigating the epithelial-to-mesenchymal transition (EMT) via transcriptional regulation.[3]

1.1.2 Oxygen's role in tumor progression

Regions of low oxygen tension (i.e., hypoxia) are common within solid tumors, forming at ranges of 70 - 200 μm from vasculature.[30] The extent of hypoxia within tumors is indicative of poor patient outcomes[31] due to hypoxia's role in i) increasing the production of reactive oxygen species (ROS), which damage deoxyribonucleic acid (DNA) and cause genetic intability,[32,33] and ii) coordinating transcriptional changes, which promote the development of a metastatic phentoype.[3,34] While the specific mechanism that increases ROS production under hypoxic conditions are not fully understood, studies have shown that complexes I, II, and III of the electron transport chain are involved.[35,36] Hypoxia-dependent transcriptional regulation, which is coordinated through hypoxia-inducible transcription factors (HIFs), has been thoroughly studied in literature and is heavily implicated in cancer progression.[2]

HIFs are constitutively expressed transcription activators that serve as regulators of oxygen homeostasis in mammalian cells. There are three known HIF isoforms, HIF-1α, HIF-2α, and HIF-3α, which form heterodimer pairs with a single β-subunit. Of these isoforms, HIF-1α and -2α has been thoroughly studied in mammalian cells and are regulated through post-transcriptional processes. Under normal oxygen tensions (i.e., normoxia), these transcription factors are hydroxylated by prolyl-hydroxylases.[1,37] Hydroxylated HIFs are recognized by von Hippel Landau proteins and marked for proteasomal degradation via ubiquitination.[38] Under hypoxic conditions, the HIF-α subunits are allowed to accumulate in the cytosol, where they eventually translocate into the nucleus, dimerize with a HIF-1β subunit, and bind to promoter sequences known as hypoxia responsive elements (HREs).[39] These promoter sequences have been found on 70 genes, but studies suggest that these sequences modulate over 200 genes.[39] Stabilization of HIF promotes the expression of vascular endothelial growth factor (VEGF;

angiogenesis),[40] glucose transporter 1 (GLUT1; anaerobic metabolism),[41] carbonic anhydrous IX (CAIX; intracellular pH regulation),[42] chemokine receptor (CXCR4; chemokine gradient detection),[43] matrix metalloproteinase 2 (MMP-2, extracellular matrix remodeling),[44] p21 (cell cycle arrest),[45] and p53 (DNA repair).[46] HIF-1α also promotes the expression of TWIST, a gene sequence responsible for coordinating the EMT.[34,47] In addition to orchestrating transcriptional regulation, *in vitro* studies using A549, a non-small lung carcinoma, and MDA-MB-231, a breast carcinoma, suggest that oxygen gradients can help direct cellular invasion.[48–51]

1.2 Oxygen gradients *in vitro*

Oxygen's role as a regulatory metabolite extends beyond cancer regulation, as it plays a vital role in sustaining normal metabolic function for most living organisms. Far-reaching involvement of oxygen in biological systems has spurred research to develop *in vitro* assays that emulate the oxygen gradients found *in vivo*. This section will discuss current methods for imposing oxygen gradients along 2D and 3D cultures, as well as strategies to quantify the oxygen gradients within these systems.

1.2.1 Oxygen gradients in 2D cultures

In 2D cultures, cells are grown on a planar surface submerged in nutrient-rich medium. To generate chemical gradients within these cultures, microfluidic devices have been developed that impose lateral oxygen gradients along the cell culture plane. Generation and maintenance of oxygen gradients in 2D cultures have relied on two different designs: network mixer and parallel flow models (Fig 1.2). In both of these designs, gasses are flown through channels in close proximity to a cell-containing bioreactor. A gas-permeable membrane separates the flow

channels from the bioreactor, allowing oxygen to freely diffuse between the structures. Equilibration between the bioreactor's medium and flow channels' gasses allow oxygen gradients to form along the cell culture.

Network mixers combine deoxygenated and oxygenated gasses prior to flowing over the bioreactor. In the mixing region, gas inputs are partitioned in a stepwise manner to produce a concentration gradient. The resulting oxygen gradients can be linear, exponential, or sigmoidal depending on the chip design, and can be further modulated by adjusting gas flow rates.[52,53] While these chip designs are less commonly used, in part, due to their design complexity, they provide exquisite spatiotemporal control over the oxygen gradients.

Parallel flow microfluidic chips are the more common approach to generating oxygen gradients in cell cultures. In these chips, oxygenated and deoxygenated gasses are flown in parallel channels, which flank the bioreactor region. Equilibrium between the gas channels results in the formation of linear oxygen gradients across the bioreactor region.[52,54–56] The steepness of the oxygen gradients can be modulated by changing the gasses used or adjusting the distance between the gas flow channels.[55] In lieu of deoxygenated gas, oxygen scavenging solutions have also been used to generate oxygen gradients in a similar source-sink fashion.[48,57]

1.2.2 Oxygen gradients in 3D cultures

While 2D cultures provide a convenient platform for studying cancer biology, cells grown in 2D formats exhibit morphologies and behaviors distinctly different than cells grown in 3D environments.[58] These phenotypic differences make it difficult to use 2D cultures to predict the range of responses or phenotypes in a tumor, and highlight the need for 3D cultures that introduce tissue-like architectures. There are a number of 3D culture formats, ranging from cells

embedded in a hydrogel slab to freestanding cellular masses (i.e., spheroids or organoid). To generate oxygen gradients across hydrogel slab cultures seeded at low cell densities and correspondingly low oxygen consumption rates, microfluidic devices similar to the methods outlined in section 1.2.2 are needed.[59,60] Spheroids and hydrogel slab cultures seeded at high cell densities passively generate oxygen gradients via cellular consumption—oxygen must penetrate into the interior of the culture, and equilibrium between cellular consumption and the diffusional delivery results in the formation of gradients in a manner similar to poorly vascularized tumors.[61,62]

Studies investigating large spheroids (> 500 μm diameter) have shown that oxygen and glucose gradients induce the stratification cell subpopulations similar to those of tumors: proliferative cells near an oxygen-rich source (e.g., medium or vasculature), senescent cells in the oxygen-poor interior, and necrotic cells in the nutrient-depleted core.[7,63] Each of these subpopulations exhibit distinctly different phenotypes, and recapitulating them allows spheroids to serve as a model for evaluating cancer chemotherapeutic resistance,[7,64,65] proliferation,[66] and gene regulation.[67]

Identifying how oxygen gradients affect the development of stratified phenotypes in 3D cultures often relies on histological sectioning.[68] This technique partitions 3D cultures into thin cross sections, reaching sub-10 μm thicknesses, and is complimented with histological staining.[61,69] Using histological sectioning, oxygen gradients have been related to increases in DNA repair[70] and chemotherapeutic resistance,[71] and decreases in proliferation.[61,69,72] While this technique provides a highly-resolved readout between cellular hypoxia and protein expression, sample preparation is laborious and requires cell fixation. Inability to isolate intact live cell

populations after sectioning is an obstacle to 3D cultures and prevents downstream analysis of the cell populations.

1.2.3 Quantifying oxygen gradients in vitro

Emulating oxygen conditions found within tumors requires generating oxygen gradients that span from normoxia (140-40 mmHg O_2) to anoxia (< 1 mmHg O_2). Sections 1.2.1 and 1.2.2 outlined cell culture formats in which oxygen gradients can be generated *in vitro*, and this section will outline validation and characterization of these oxygen gradients via direct quantification.[52,59,73] Measurement of oxygen gradients in cell cultures is primarily performed using optodes, which consist of an oxygen-sensitive dye suspended in polymer matrix. Electroanalytical approaches have also been used to quantify oxygen in spheroids and hydrogel slabs via Clarke-type electrodes;[62] however, optical techniques are preferred because they do not consume oxygen during measurement, and can be easily applied to planar surfaces for two-dimensional (2D) mapping of oxygen gradients. Oxygen-sensing particles can also be incorporated into 3D cultures to enable mapping of 3D oxygen gradients.[74]

A myriad of oxygen-sensitive luminescent dyes have been developed since their conception in the 1930's, and can be grouped into two categories: i) organic and ii) metalloporphyrin.[75] The organic dyes consist of polycyclic hydrocarbons and include pyrene, anthracene, and fullerene. The metalloporphyrin dyes consist of metal-ligand complexes with Ru(II)-, Pd(II)-, Ir(II)-, and Pt(II) metal centers with incomplete coordination spheres. Both categories of dyes sense oxygen through a similar mechanism: the dyes are normally luminescent but are dynamically quenched by oxygen. The emission of these dyes can be related to environmental oxygen concentrations via the Stern-Volmer expression:

$$I_0/I = 1+K_{sv}[O_2] \quad \text{Eq. [1.1]}$$

where I_0 and I represent the emission intensity in the absence and presence of oxygen, and K_{sv} is an empirically derived Stern-Volmer constant.

Metalloporphyrin dyes, rather than their organic counterparts, have been exclusively used for oxygen quantification in cell cultures due to their increased sensitivity, photostability, and phosphorescence lifetimes.[75] These dyes are also easily sequestered into films or particles with minimal leeching and can be measured using luminescence intensity or lifetime imaging microscopy.[76] Integration of these dyes into cell cultures is typically done via thin-film membranes, where the dye is dispersed throughout a thin polymeric film and placed in close proximity to the cell culture. These films enable the mapping of 2D oxygen gradients along cell cultures, [48,52,73,79,80] or can also be coated onto the tip of an optical fiber for point measurements. [77,78] In cases where the dyes are susceptible to leaching or insoluble in the polymer matrix's solvent, they can be encapsulated into particles. These micron- to nanosized particles can then be dispersed throughout a substrate/film,[59,81] suspended in solution,[82] or even sequestered by cells to quantify intracellular oxygen concentrations.[83]

1.3 Paper-based cultures as a tumor model

Current 3D cell culture models are limited in their ability to selectively isolate subpopulations of cells based on their location. Histological sectioning coupled with immunostaining have been used to correlate regional cell phenotype with local oxygen tensions in 3D cultures; however, this technique requires extensive sample preparation and is relatively laborious. Laser capture microdissection has been used to isolate single cells from tissue and cell cultures, but this technique also requires extensive sample preparation prior to laser dissection.

To better understand adaptations of cancer cell behavior to environmental conditions, a new culture format is needed that is capable of i) replicating the TME in a controllable manner, and ii) isolating viable cell subpopulations for downstream analysis.

Paper-based cultures (PBCs) are an emerging 3D culture platform that overcomes limitations of current 3D models by providing a modular approach towards culture (de)construction (**Fig. 1.3**). Within these cultures, cell-laden paper scaffolds are stacked together to form tissue-like constructs. After prolonged incubation, these scaffolds are partitioned by simply peeling the scaffolds apart. Cells within the individual scaffolds can be recovered for continued culture or analyzed via a number of techniques: microscopy,[49] fluorescence imaging,[11,73,84,85] quantitative polymerase chain-reaction (qPCR),[84] mass spectrometry,[86] or enzyme-linked immunosorbent assays (ELISAs).[50] By stacking enough paper scaffolds together, PBCs can be assembled to resemble poorly-vascularized tumorous tissue and enable mechanistic studies into cancer invasion and chemoresistance.[51,87,88]

1.3.1 Paper-based cultures

Paper-based cultures consist of porous sheets of paper infused with a cell-laden hydrogel. The hydrogel provides a biomimetic 3D environment for the cells and the paper fibers provide structural support to the fragile hydrogel matrix. Infusion of the hydrogel into the paper scaffolds is straightforward, as the hydrophilic fibers readily wick and retain the hydrogel. These cultures have high aspect ratios with heights equivalent to the thickness of the paper scaffolds, and individual scaffolds to be stacked together to form tissue-like constructs. By exchanging the type of paper used, the thickness and porosity can be modulated.[89] Assembling cultures by stacking together cell-laden scaffolds provides exceptional control over the spatial arrangement, density,

and type of cells in a single stack. Cells can be also be confined to discrete regions along individual paper scaffolds by patterning the paper with hydrophobic materials such as wax, polydimethylsiloxane (PDMS), photoresist, or polyvinyl chloride.[11,90–93] The simplicity of wax-patterning paper allows novel culture designs to be readily prototyped with nothing more than a commercial printer, eliminating the need for photolithography or embossing setups.

A common strategy in PBCs is to incorporate selectively permeable barriers along the outer periphery of the culture. By placing barriers along one side of a stacked culture and leaving the opposite side open to nutrient-rich medium, monotonic gradients of nutrients, oxygen, and wastes are formed across the thickness of the culture. Barriers made of gas-permeable materials, such as PDMS, can be used to effectively decouple gradients of oxygen from gradients of nutrient and waste.[49,50,87] Because stacked cultures require disassembly to analyze cell populations within individual scaffolds, stacked PBCs are suited for end-point assays rather than kinetic studies.

To overcome the limitations of stacked cultures, channel shaped cultures have also been developed. In channel-shaped PBCs, cells are seeded throughout the channel or in discrete locations. Selectively permeable barriers are interfaced with the channel-shaped culture and restrict the free-exchange of medium into the culture. Openings in the barriers allow medium to diffuse into the culture at spatial defined locations, and cause metabolite gradients to form laterally along the channel of seeded cells. Because cells and gradients exist in a single lateral plane in channel-shaped cultures, microscopy can be used to interrogate changes in cell distribution[49,94] and map chemical environments via planar sensors.[73,95] This culture design is suited for real-time imaging and kinetic studies, but the inability to spatially isolate cells limits it application to end-point assays.

1.3.2 Using paper cultures to replicate the tumor

Gradients in PBCs form via diffusion-consumption mechanisms similar to the gradients that form in poorly vascularized tumors. However, unlike tumorous tissue, PBCs provide a level of control over the gradients that form *in situ*. By changing cellular placement and density within a stacked or channel-shaped culture, cellular consumption can be spatially modulated to control the shape and steepness of resulting chemical gradients.[88] Likewise, interchanging barriers along the culture's periphery allow gradients to be decoupled from one another. Experimental control over gradient formation in PBCs enables mechanistic studies to be performed that relate cellular behavior within an individual scaffold to that scaffold's local chemical environment.

Mosadegh *et al*. capitalized on PBCs' ability to modulate the formation of chemical gradients by developing a paper-based invasion assay.[51] In this assay, oxygen gradients were modulated within a stacked PBC by adjusting the gas permeability of the peripheral barriers and changing cell proximity to a nutrient-rich source within a stacked PBC. Their findings indicate that A459 lung carcinoma cells preferentially invade toward higher oxygen tensions, which was contradictory to previous findings in 2D culture.[48] Truong *et al*. and Kenney *et al*. followed-up on this invasion assay using a MDA-MB-231 breast carcinoma cells, and found similar trends in invasion towards oxygen sources.[49,84] Hypoxia probes and HIF signaling were used to confirm differences in extracellular oxygen tensions within the invasion assays, and confirm that gradients of oxygen were necessary for directing cellular invasion.[50]

Prolonged incubation in PBCs under oxygen and nutrient gradients also leads to cell stratification into distinct subpopulations. Early work by the Whitesides laboratory showed that cancer cells located at the interior of the a stacked culture exhibit increased death, while cells along the nutrient-rich exterior proliferated.[89] McGuigan *et al.* used liquid chromatography-mass

spectrometry to map metabolites of a stacked culture, and found that cells experiencing hypoxia at the interior of a stacked culture exhibited significant increases in anaerobic glycolysis-associated metabolites.[86] Further confirmation of the stratification of cell populations were shown by Simon *et al*, who found that cells within the interior of a stacked culture escaped radiotherapy in an oxygen-dependent manner.[96]

The ability of PBCs to mimic the tumor environment and measure cancer invasion, proliferation, metabolism, and radiosensitivity in a spatially-defined readout demonstrates the versatility of this platform. Currently, PBCs are limited to a relatively low throughput; however, efforts are being made to increase throughput to match 96-well assays.[97] The accessibility of paper and simplicity in assembling these cultures make PBCs a promising platform for continued study of cancer progression.

1.4. Interrogating cellular responses in paper cultures

To confirm that heterogeneous environments of stacked and channel-shaped cultures are responsible for changes in cell phenotypes, new assays are needed. Initial assays for PBCs focused on identifying and enumerating viable cell populations (**Fig. 1.4)**. These assays were used to substantiate the presence of oxygen and nutrient gradients, as viable cells are located in close proximity to the nutrient source while necrotic cells are at the interior of the culture. To validate that cells within the interior of the stacked cultures were experiencing intracellular hypoxia, cell-based hypoxia readouts were developed that utilized HRE activation of fluorescent proteins and hypoxia-dependent stains (**Fig. 1.5)**.

1.4.1 Enumerating viable cells

To determine whether cell populations are changing within PBCs, methods are needed that can accurately enumerate viable cells within paper scaffolds. Early approaches towards cell quantification in paper relied on cell lines engineered to constitutively express fluorescent proteins. Fluorescent flatbed scanners were used to image entire scaffolds, and calibration curves relate the average fluorescent intensity to the total number of cells within a cell-seeded region. This method preserves cells for further analysis, and has a reported limit of quantification (LoQ) as low as 2000 cells.[84] It is important to note that this technique has difficultly discriminating live and dead cells, as protein fluorescence can persist during cellular death.[98]

Adenosine triphosphate (ATP) bioluminescence assays (e.g., CellTiter-Glo®) provide an alternative approach towards enumerating viable cells in PBCs.[96] In these assays, cells are lysed and ATP released from the cell fuels a bioluminescent reaction involving luciferase.[99] The resulting luminescence is indicative of the number of metabolically active cells and can be related to cell number using calibration curves. While this approach is more selective in identifying viable cells than fluorescent protein expression, this technique requires cell lysis which prevents downstream analysis of the cells. Additionally, this technique requires ATP levels to be comparable between cell populations for an accurate analysis; however, cells experiencing hypoxia have diminished ATP levels due to changes in metabolic pathways,[100] which limits these techniques accuracy for cell enumeration in stacked cultures. Another common cell-based assay designed to quantify cells involves the metabolic conversion of 3-(4,5-dimethylthiazol-2-yl)-2,5-diphenyltetrazolium bromide (MTT) to insoluble formazan crystals.[101] While this assay is commonly considered the gold-standard to enumerating cells in 2D cultures, it has not been adapted for use in PBCs.

Efforts to develop a cell enumeration assay independent of fluorescent protein expression and environmental oxygen led to conception of a quantitative polymerase chain-reaction (qPCR) assay.[84] In this assay, DNA is extracted from cells within zones along a single paper scaffold and qPCR is used to determine the amount of genetic material present within that culture. Calibration curves are used to convert qPCR readouts to the number of cells in a scaffold. This technique has a LoQ one order of magnitude lower than fluorescent protein expression and is independent of environmental conditions; however, intact genetic material of dead cells cannot be discerned from living cells, which can lead to an overestimation of viable cells.

Discrimination between live and dead cell populations within paper scaffolds has been done via counterstaining with fluorescent molecules.[89] Viable cells with intact membranes are identified using fluorescein derivatives that are metabolized by intracellular esterases (e.g., calcein AM and fluorescein diacetate). Prior to metabolization, these molecules are non-fluorescent and freely pass through the cell membrane; however, they become fluorescent and cell-permanent upon hydrolysis. Dead cell identification is performed using DNA intercalating dyes, such as propidium iodide or 7-aminoactinomycin D. These dyes are normally unable to pass through the cell membrane of living cells; however, membranes of dying cells are commonly compromised, allowing these dyes to intercalate into the DNA.

1.4.2 Cell-based hypoxia readouts

Quantifying the distribution of viable and non-viable cell populations can indicate the presence of oxygen and nutrients gradients in paper-based cultures; however, confirmation that cells are experiencing these gradients requires cell-based assays. To validate intracellular

hypoxia within stacked cultures, three approaches have been used: expression of a HRE reporter gene, immunostaining for HIFs, and bioreactive hypoxia probes.

Vordermark *et al*. first described the use of a genetic vector to identify cells experiencing hypoxia via the production of green fluorescent protein (GFP).[102] This vector, known as 5HRE/GFP, contains five HRE promotor sequences followed by a GFP reporter sequence. Under hypoxic conditions, HIFs binds to the HRE sequences and upregulate the expression of GFP for easy identification of intracellular hypoxia. Truong *et al*. utilized MDA-MB-231 cells transfected with the 5HRE/GFP vector to identify differences in environmental oxygen tensions for cells in stacked PBCs.[50] In this work, it was found that cells further from the nutrient-rich medium exhibited increased GFP expression, and therefore experienced increasingly lower oxygen concentrations.

Accumulation of HIFs in the nucleus is indicative of cellular hypoxia and can be used to identify hypoxia within cells. In this assay, cells are fixed and stained with two dyes: a DNA intercalating dye, and a fluorescently labeled anti-HIF antibody. The DNA stain is used to identify the nucleus, and the ratio between cytosolic-localized HIF to nuclear HIF provides a relative indication of intracellular hypoxia.[103] While this technique is qualitative, it has been used to identify differences in HIF localization of MDA-MB-231 cells in stacked and channel-shaped cultures.[49,50]

Hypoxia-sensing molecules, pimonidazole and EF5, provide an alternative approach to identifying hypoxic cells.[104,105] Under low oxygen conditions, these nitroimidazole-containing molecules undergo reduction and covalently bond to thiol-containing proteins. The resulting adducts are stained with fluorescently labeled antibodies, allowing for qualitative analysis of intracellular hypoxia.[105,106] Comparisons between pimonidazole staining and microelectrodes

have shown that staining efficiency significantly increases at oxygen tensions less than 10 mmHg, which corresponds to hypoxia.[107] Pimonidazole has been used in stacked PBCs to confirm that cells deeper in a stacked culture experienced reduced oxygen tensions.[50]

1.5. Overview of the dissertation

The work in this thesis focuses on developing new methods to quantify oxygen gradients in PBCs, and correlate these gradients to changes in cancer cell chemoresistance. Chapter 2 describes the fabrication, characterization, and integration of planar oxygen sensors into paper-based cultures. Chapter 3 outlines the fabrication and characterization of a modular fluidic chip capable of generating oxygen gradients across 3D cell cultures. In Chapter 4, a paper-based tumor model was developed to study the relationship between regional oxygen tensions and chemoresistance of a colon carcinoma cell line. The dissertation concludes with Chapter 5, which outlines preliminary work using flow cytometry to characterize cell populations extracted from paper scaffolds.

1.6 Figures

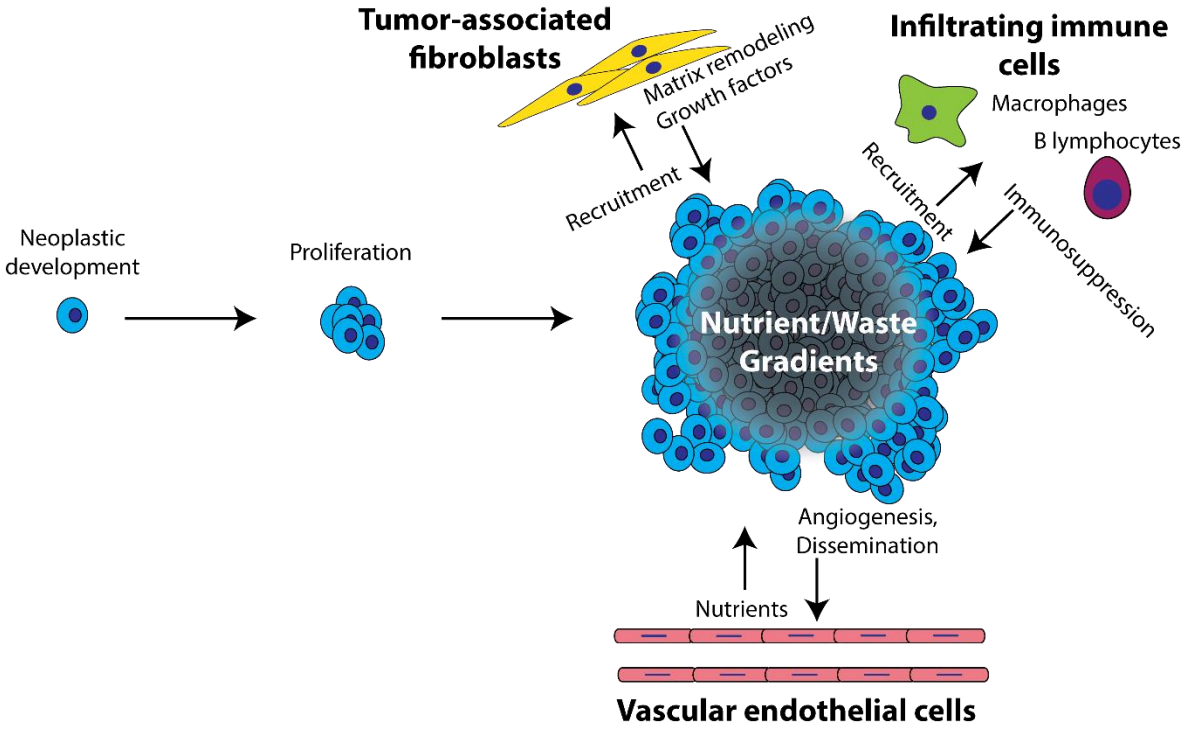

Fig 1.1 Diagram of the progression of cancer from initial development of a neoplastic cell to the growth and evolution of a TME. Interactions between cancer cells and tumor-associated fibroblasts, infiltrating immune cells, and vascular endothelial cells contribute the TME and aid in the progression of the tumor. Gradients of nutrients and waste extend from the vasculature and act as abiotic components of the TME.

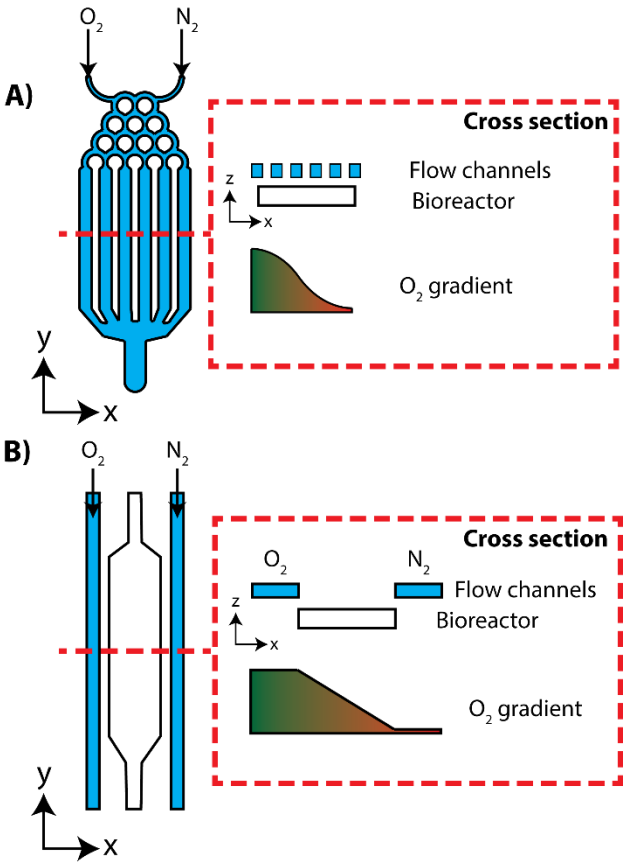

Fig 1.2 Design examples of microfluidic oxygen gradient generators. (A) Network mixing devices have two gas inputs and mix them together in series of split channels. The flow channels are adjacent to a bioreactor with a gas permeable membrane separating the two regions. Sigmoidal oxygen gradients are imposed across the culture, but the shape of these gradients can be modulated by adjusting flow rates, channel design, and input gasses. (B) Parallel flow devices flow two gasses in parallel channels to impose linear oxygen gradients across the cell culture. The shape of the gradients can be modulated by adjusting the distance between flow channels and the gasses used.

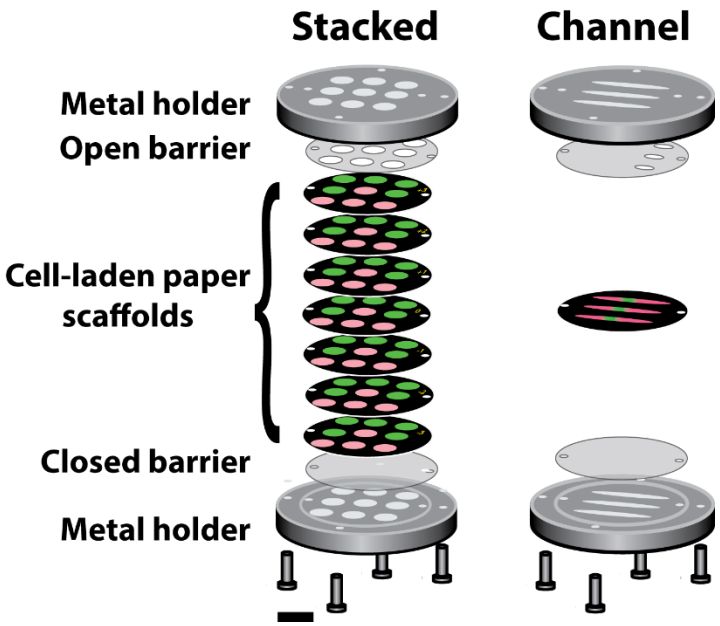

Fig 1.3 Schematic of stack- and channel-shaped paper-based cultures. In these cultures, cell-laden paper scaffolds are sandwiched between an open barrier (top) and closed barrier (bottom). Green regions indicate zones seeded with cells, and pink regions indicate zones seeded with cell-free Matrigel. Nutrient-rich medium is able to enter the culture through the open barrier, while the closed barrier prevents diffusion into the cultures. The metal holders enclose the entire assembly and keep each layer in conformal contact. A single culture can fit into the well of a 6-well plate. Scale bar = 6 mm.

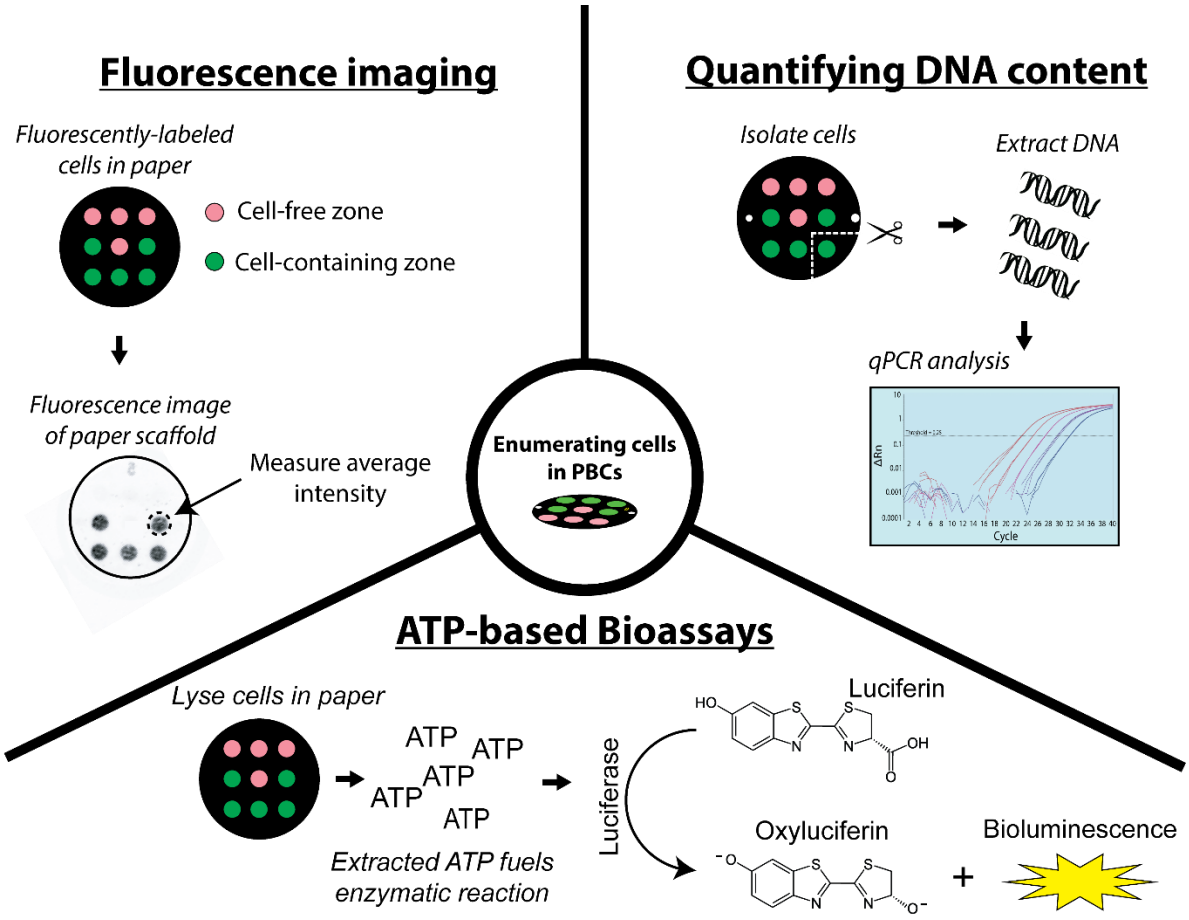

Fig 1.4 Overview of common techniques used to enumerate viable cells in PBCs. These techniques include measuring the average fluorescence of fluorescently-labeled cell populations, the extraction and quantification of DNA via qPCR, and the use of a bioassay to relate ATP to cell number.

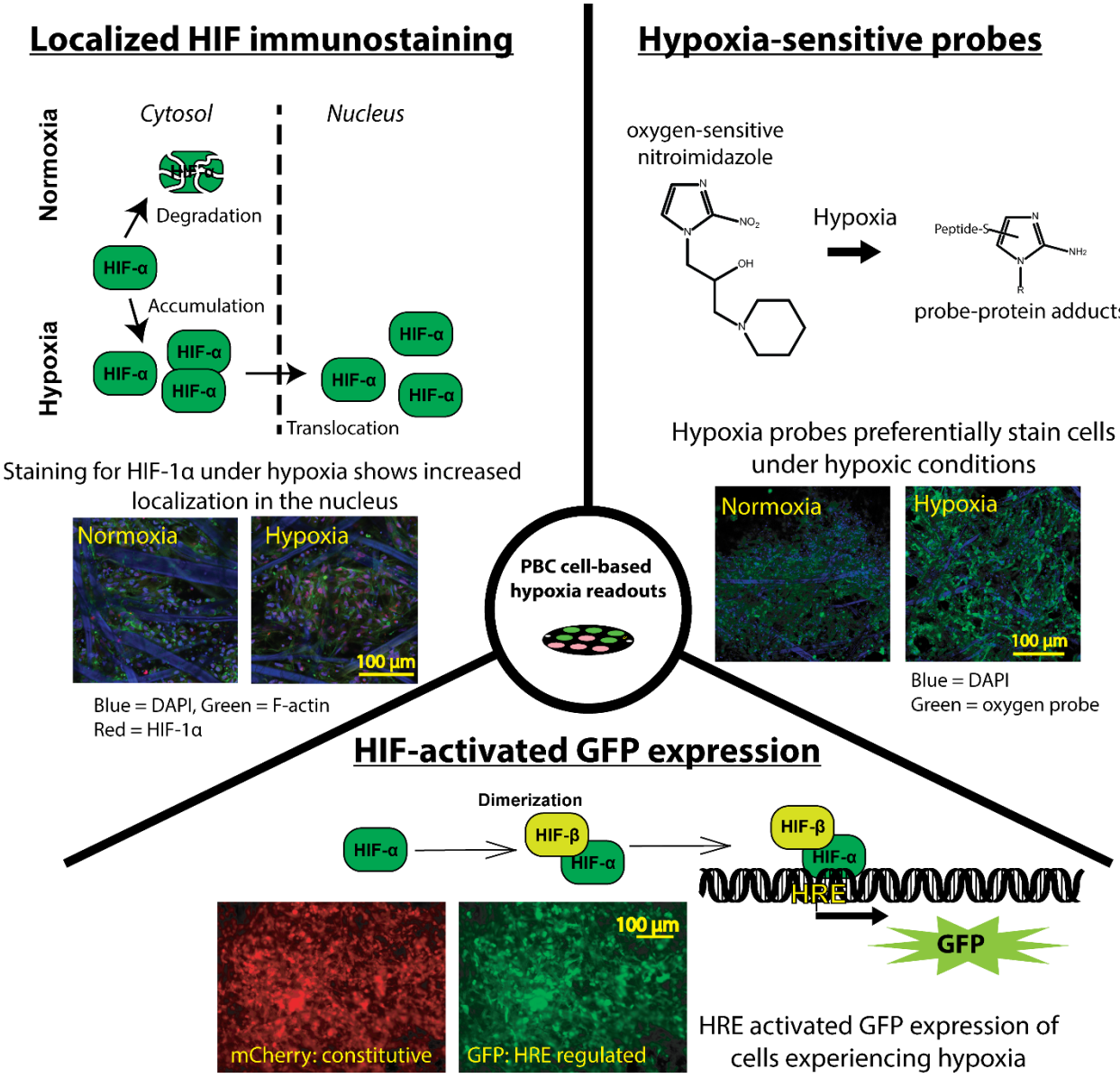

Fig 1.5 Overview of cell-based assays designed to identify intracellular hypoxia in PBCs. These assays utilize three techniques: HIF immunostaining to identify localization within cells, staining with hypoxia-sensitive probes that bind to proteins under hypoxic conditions, and measuring HRE activation by the expression of fluorescent proteins.

REFERENCES

(1) Semenza, G. L. *Physiology* **2009**, *24*, 97–106.

(2) Semenza, G. L. *Trends Pharmacol Sci.* **2013**, *33* (4), 207–214.

(3) Semenza, G. L. *Biochim. Biophys. Acta - Mol. Cell Res.* **2015**, *1863* (3), doi: 10.1016/j.bbamcr.2015.05.036.

(4) Edmondson, R.; Broglie, J. J.; Adcock, A. F.; Yang, L. *Assay Drug Dev. Technol.* **2014**, *12* (4), 207–218.

(5) Schmeichel, K. L. *J. Cell Sci.* **2003**, *116* (12), 2377–2388.

(6) Kenny, P. A.; Lee, G. Y.; Myers, C. A.; Neve, R. M.; Semeiks, J. R.; Spellman, P. T.; Lorenz, K.; Lee, E. H.; Barcellos-Hoff, M. H.; Petersen, O. W.; Gray, J. W.; Bissell, M. J. *Mol. Oncol.* **2007**, *1* (1), 84–96.

(7) Hirschhaeuser, F.; Menne, H.; Dittfeld, C.; West, J.; Mueller-Klieser, W.; Kunz-Schughart, L. A. *J. Biotechnol.* **2010**, *148* (1), 3–15.

(8) Tibbitt, M W., Anseth, K. S. *Biotec* **2010**, *103* (4), 655–663.

(9) Sutherland, R. M.; Sordat, B.; Bamat, J.; Gabbert, H.; Bourrat, B.; Mueller-Klieser, w. *Cancer Res.* **1986**, *46* (October), 5320–5329.

(10) Szot, C. S.; Buchanan, C. F.; Freeman, J. W.; Rylander, M. N. **2011**, *32* (31), 7905–7912.

(11) Derda, R.; Laromaine, A.; Mammoto, A.; Tang, S. K. Y.; Mammoto, T.; Ingber, D. E.; Whitesides, G. M. *Proc. Natl. Acad. Sci. U. S. A.* **2009**, *106* (44), 18457–18462.

(12) Chaffer, C.; Weinberg, R. *Science (80-.).* **2011**, *331* (6024), 1559–1564.

(13) Chaffer, C.; Weinberg, R. *Cancer Discov.* **2015**, *5* (1), 22–24.

(14) Wang, M.; Zhao, J.; Zhang, L.; Wei, F.; Lian, Y.; Wu, Y.; Gong, Z.; Zhang, S.; Zhou, J.; Cao, K.; Li, X.; Xiong, W.; Li, G.; Zeng, Z.; Guo, C. *J. Cancer* **2017**, *8* (5), 761–773.

(15) Quail, D. F.; Joyce, J. A. *Nat. Med.* **2013**, *19* (11), 1423–1437.

(16) Whitesides, T. *Oncogene* **2008**, *27* (45), 5904–5912.

(17) Hanahan, D.; Coussens, L. M. *Cancer Cell* **2012**, *21* (3), 309–322.

(18) Cooke, V.; LeBleu, V.; Keskin, D.; Khan, Z.; O'Connel, J.; Teng, Y.; Duncan, M.; Xie, L.; Maeda, G.; Vong, S.; Sugimoto, H.; Rocha, R.; Damascena, A.; Brentani, R.; Kalluri,

R. *Cancer Cell* **2014**, *21* (1), 66–81.

(19) Folkman, J.; Watson, K.; Ingber, D.; Hanahan, D. *Nature*. 1989, pp 58–61.

(20) Nishida, N.; Yano, H.; Nishida, T.; Kamura, T.; Kojiro, M. *Vasc. Health Risk Manag.* **2006**, *2* (3), 213–219.

(21) Ruffell, B.; DeNardo, D. G.; Affara, N. I.; Coussens, L. M. *Cytokine Growth Factor Rev.* **2010**, *21* (1), 3–10.

(22) Lu, P.; Takai, K.; Weaver, V. M.; Werb, Z. *Cold Spring Harb. Perspect. Biol.* **2011**, *3* (12), a005058.

(23) Dirat, B.; Bochet, L.; Dabek, M.; Daviaud, D.; Dauvillier, S.; Majed, B.; Wang, Y. Y.; Meulle, A.; Salles, B.; Le Gonidec, S.; Garrido, I.; Escourrou, G.; Valet, P.; Muller, C. *Cancer Res.* **2011**, *71* (7), 2455–2465.

(24) Erez, N.; Truitt, M.; Olson, P.; Hanahan, D. *Cancer Cell* **2010**, *17* (2), 135–147.

(25) Marusyk, A.; Polyak, K. *Biochim Biophys Acta* **2011**, *1805* (1), 1–28.

(26) Condeelis, J.; Singer, R. H.; Segall, J. E. *Annu. Rev. Cell Dev. Biol.* **2005**, *21* (1), 695–718.

(27) Kelley, L. C.; Lohmer, L. L.; Hagedorn, E. J.; Sherwood, D. R. *J. Cell Biol.* **2014**, *204* (3), 291–302.

(28) Semenza, G. L. **2011**, *20* (1), 1–10.

(29) Papp-Szabó, E.; Josephy, P. D.; Coomber, B. L. *Int. J. Cancer* **2005**, *116* (5), 679–685.

(30) McKeown, S. R. *Br. J. Radiol.* **2014**, *87* (1035), 1–12.

(31) Jubb, A. M.; Buffa, F. M.; Harris, A. L. *J. Cell. Mol. Med.* **2010**, *14* (1–2), 18–29.

(32) Kondoh, M.; Ohga, N.; Akiyama, K.; Hida, Y.; Maishi, N.; Towfik, A. M.; Inoue, N.; Shindoh, M.; Hida, K. *PLoS One* **2013**, *8* (11), 1–14.

(33) Lluis, J. M.; Buricchi, F.; Chiarugi, P.; Morales, A.; Fernandez-Checa, J. C. *Cancer Res.* **2007**, *67* (15), 7368–7377.

(34) Yang, M. H.; Wu, M. Z.; Chiou, S. H.; Chen, P. M.; Chang, S. Y.; Liu, C. J.; Teng, S. C.; Wu, K. J. *Nat. Cell Biol.* **2008**, *10* (3), 295–305.

(35) Tafani, M.; Sansone, L.; Limana, F.; Arcangeli, T.; De Santis, E.; Polese, M.; Fini, M.; Russo, M. A. *Oxid. Med. Cell. Longev.* **2016**, *2016*.

(36) Wang, Q.; Zheng, Y.; Dong, L.; Ho, Y.; Guo, Z. *Free Radic. Biol. Med.* **2007**, *42* (5), 642–653.

(37) Semenza, G. L. *Annu. Rev. Cell Dev. Biol.* **1999**, *15* (1), 551–578.

(38) Ivan, M.; Kondo, K.; Yang, H.; Kim, W.; Valiando, J.; Ohh, M.; Salic, A.; Asara, J. M.; Lane, W. S.; Kaelin, W. G. *Science (80-.).* **2001**, *292* (5516), 464–468.

(39) Wenger, R. H.; Stiehl, D. P.; Camenisch, G. *Sci. Signal.* **2005**, *2005* (306), re12-re12.

(40) Liu, Y.; Cox, S.; Morita, T.; Kourembanas, S. *Circ. Res.* **1995**, *77*, 638–643.

(41) Ebert, B. L.; Firth, J. D.; Ratcliffe, P. J. *J. Biol. Chem.* **1995**, *270* (49), 29083–29089.

(42) Kaluz, S.; Kaluzová, M.; Liao, S. Y.; Lerman, M.; Stanbridge, E. J. *Biochim. Biophys. Acta - Rev. Cancer* **2009**, *1795* (2), 162–172.

(43) Schioppa, T.; Uranchimeg, B.; Saccani, A.; Biswas, S. K.; Doni, A.; Rapisarda, A.; Bernasconi, S.; Saccani, S.; Nebuloni, M.; Vago, L.; Mantovani, A.; Melillo, G.; Sica, A. *J. Exp. Med.* **2003**, *198* (9), 1391–1402.

(44) Jing, S. W.; Wang, Y. D.; Chen, L. Q.; Sang, M. X.; Zheng, M. M.; Sun, G. G.; Liu, Q.; Cheng, Y. J.; Yang, C. R. *Dis. Esophagus* **2013**, *26* (1), 75–83.

(45) Goda, N.; Ryan, H. E.; Khadivi, B.; McNulty, W.; Rickert, R. C.; Johnson, R. S. *Mol. Cell. Biol.* **2003**, *23* (1), 359–369.

(46) Schmid, T.; Zhou, J.; Brüne, B. *J. Cell. Mol. Med.* **2004**, *8* (4), 423–431.

(47) Wang, Y.; Liu, J.; Ying, X.; Lin, P. C.; Zhou, B. P. *Sci. Rep.* **2016**, *6* (April), 1–10.

(48) Chang, C.-W.; Cheng, Y.-J.; Tu, M.; Chen, Y.-H.; Peng, C.-C.; Liao, W.-H.; Tung, Y.-C. *Lab Chip* **2014**, *14* (19), 3762–3772.

(49) Kenney, R. M.; Boyce, M. W.; Truong, A. S.; Bagnell, C. R.; Lockett, M. R. *Analyst* **2015**, *141*, 661–668.

(50) Truong, A. S.; Lockett, M. R. *Analyst* **2016**, 3874–3882.

(51) Mosadegh, B.; Lockett, M. R.; Minn, K. T.; Simon, K. A.; Gilbert, K.; Hillier, S.; Newsome, D.; Li, H.; Hall, A. B.; Boucher, D. M.; Eustace, B. K.; Whitesides, G. M. *Biomaterials* **2015**, *52* (1), 262–271.

(52) Lo, J. F.; Sinkala, E.; Eddington, D. T. *Lab Chip* **2010**, *10* (18), 2394–2401.

(53) Polinkovsky, M.; Gutierrez, E.; Levchenko, A.; Groisman, A. *Lab Chip* **2009**, *9* (8), 1073.

(54) Shiwa, T.; Uchida, H.; Tsukada, K. *Am. J. Biomed. Eng.* **2012**, *2* (4), 175–180.

(55) Rexius-Hall, M. L.; Rehman, J.; Eddington, D. T. *Integr. Biol.* **2017**, *9*, 742–750.

(56) Uchida, H.; Sato, A.; Miyayama, A.; Tsukada, K. *Adv. Biomed. Eng.* **2013**, *2*, 143–149.

(57) Wang, L.; Liu, W.; Wang, Y.; Wang, J.; Tu, Q.; Liu, R.; Wang, J. *Lab Chip* **2013**, *13* (4), 695–705.

(58) Gurski, L.; Petrelli, N.; Jia, X.; Farach-Carson, M. *Oncol. Issues* **2010**, *25* (1), 20–25.

(59) Acosta, M. a; Jiang, X.; Huang, P.-K.; Cutler, K. B.; Grant, C. S.; Walker, G. M.; Gamcsik, M. P. *Biomicrofluidics* **2014**, *8* (5), 54117.

(60) Funamoto, K.; Zervantonakis, I. K.; Liu, Y.; Ochs, C. J.; Kim, C.; Kamm, R. D. *Lab Chip* **2012**, *12* (22), 4855.

(61) Grimes, D. R.; Kelly, C.; Bloch, K.; Partridge, M. *J. R. Soc. Interface* **2014**, *11* (92), 20131124.

(62) Colom, A.; Galgoczy, R.; Almendros, I.; Xaubet, A.; Farré, R.; Alcaraz, J. *J. Biomed. Mater. Res. - Part A* **2014**, *102* (8), 2776–2784.

(63) Evans, S. M.; Hahn, S. M.; Magarelli, D. P.; Koch, C. J. *Am. J. Clin. Oncol.* **2001**, *24* (5), 467–472.

(64) Friedrich, J.; Seidel, C.; Ebner, R.; Kunz-Schughart, L. A. *Nat. Protoc.* **2009**, *4* (3), 309–324.

(65) Karlsson, H.; Fryknäs, M.; Larsson, R.; Nygren, P. *Exp. Cell Res.* **2012**, *318* (13), 1577–1585.

(66) Chignola, R.; Schenetti, A.; Andrighetto, G.; Chiesa, E.; Foroni, R.; Sartoris, S.; Tridente, G.; Liberati, D. *Cell Prolif.* **2000**, *33* (4), 219–229.

(67) Zschenker, O.; Streichert, T.; Hehlgans, S.; Cordes, N. *PLoS One* **2012**, *7* (4).

(68) Kabadi, P. K.; Vantangoli, M. M.; Rodd, A. L.; Leary, E.; Madnick, S. J.; Morgan, J. R.; Kane, A.; Boekelheide, K. *Biotechniques* **2016**, *59* (2), 279–286.

(69) Grimes, D. R.; Fletcher, A. G.; Partridge, M. *R. Soc. Open Sci.* **2014**, *1* (1), 140080–140080.

(70) Riffle, S.; Pandey, R. N.; Albert, M.; Hegde, R. S. *BMC Cancer* **2017**, *17* (1), 1–12.

(71) Roberts, D. L.; Williams, K. J.; Cowen, R. L.; Barathova, M.; Eustace, A. J.; Brittain-Dissont, S.; Tilby, M. J.; Pearson, D. G.; Ottley, C. J.; Stratford, I. J.; Dive, C. *Br. J. Cancer* **2009**, *101* (8), 1290–1297.

(72) Gomes, A.; Guillaume, L.; Grimes, D. R.; Fehrenbach, J.; Lobjois, V.; Ducommun, B. *PLoS One* **2016**, *11* (8), 1–11.

(73) Boyce, M. W.; Kenney, R. M.; Truong, A. S.; Lockett, M. R. *Anal. Bioanal. Chem.* **2016**, *408* (11), 2985–2992.

(74) Lesher-pérez, S. C.; Kim, G.; Kuo, C.; Leung, B. M.; Mong, S.; Kojima, T.; Moraes, C.; Thouless, M. D.; Luker, G. D.; Takayama, S. *Biomater. Sci.* **2017**, *5*, 2106–2113.

(75) Wang, X.; Wolfbeis, O. S. *Chem. Soc. Rev.* **2014**, *43* (10), 3666–3761.

(76) Grist, S. M.; Chrostowski, L.; Cheung, K. C. *Sensors (Basel).* **2010**, *10* (10), 9286–9316.

(77) Klimant, I.; Meyer, V.; Kühl, M. *Limnol. Oceanogr.* **1995**, *40* (6), 1159–1165.

(78) Park, E. J.; Reid, K. R.; Tang, W.; Kennedy, R. T.; Kopelman, R. *J. Mater. Chem.* **2005**, *15* (27–28), 2913.

(79) Kocincová, A. S.; Nagl, S.; Arain, S.; Krause, C.; Borisov, S. M.; Arnold, M.; Wolfbeis, O. S. *Biotechnol. Bioeng.* **2008**, *100* (3), 430–438.

(80) Naciri, M.; Kuystermans, D.; Al-Rubeai, M. *Cytotechnology* **2008**, *57* (3), 245–250.

(81) Itoh, T.; Yaegashi, K.; Kosaka, T.; Kinoshita, T.; Morimoto, T. *Am. J. Physiol.* **1994**, *267* (5 Pt 2), H2068-78.

(82) Borisov, S. M.; Klimant, I. *Microchim. Acta* **2009**, *164* (1–2), 7–15.

(83) Koo, Y. E. L.; Cao, Y.; Kopelman, R.; Koo, S. M.; Brasuel, M.; Philbert, M. A. *Anal. Chem.* **2004**, *76* (9), 2498–2505.

(84) Truong, A. S.; Lochbaum, C. A.; Boyce, M. W.; Lockett, M. R. *Anal. Chem.* **2015**, *87* (22), 11263–11270.

(85) Lloyd, C. C.; Boyce, M. W.; Lockett, M. R. *Curr. Protoc. Chem. Biol.* **2017**, *9*, 1–20.

(86) Rodenhizer, D.; Gaude, E.; Cojocari, D.; Mahadevan, R.; Frezza, C.; Wouters, B. G.; McGuigan, A. P. *Nat. Mater.* **2016**, *15* (2), 227–234.

(87) Mosadegh, B.; Dabiri, B. E.; Lockett, M. R.; Derda, R.; Campbell, P.; Parker, K. K.; Whitesides, G. M. *Adv Heal. Mater* **2014**, *3* (7), 1036–1043.

(88) Boyce, M. W.; LaBonia, G. J.; Hummon, A. B.; Lockett, M. R. *Analyst* **2017**, *142* (15), 2819–2827.

(89) Derda, R.; Tang, S. K. Y.; Laromaine, A.; Mosadegh, B.; Hong, E.; Mwangi, M.; Mammoto, A.; Ingber, D. E.; Whitesides, G. M. *PLoS One* **2011**, *6* (5).

(90) Juvonen, H.; Määttänen, A.; Laurén, P.; Ihalainen, P.; Urtti, A.; Yliperttula, M.; Peltonen, J. *Acta Biomater.* **2013**, *9* (5), 6704–6710.

(91) Camci-Unal, G.; Newsome, D.; Eustace, B. K.; Whitesides, G. M. *Adv. Healthc. Mater.* **2016**, *5* (6), 641–647.

(92) Kim, Y. S.; Yang, Y.; Henry, C. S. *Sensors Actuators, B Chem.* **2018**, *255*, 3654–3661.

(93) Martinez, A. W.; Phillips, S. T.; Whitesides, G. M. *Proc. Natl. Acad. Sci.* **2008**, *105* (50), 19606–19611.

(94) Kenney, R. M.; Lloyd, C. C.; Whitman, N. A.; Lockett, M. R. *Chem. Commun.* **2017**, *53* (53), 7194–7210.

(95) Kenney, R. M.; Boyce, M. W.; Whitman, N.; Kromhout, B. P.; Lockett, M. R. **2018**.

(96) Simon, K. A.; Mosadegh, B.; Minn, K. T.; Lockett, M. R.; Mohammady, M. R.; Boucher, D. M.; Hall, A. B.; Hillier, S. M.; Udagawa, T.; Eustace, B. K.; Whitesides, G. M. *Biomaterials* **2016**, *95*, 47–59.

(97) Deiss, F.; Mazzeo, A.; Hong, E.; Ingber, D. E.; Derda, R.; Whitesides, G. M. *Anal. Chem.* **2013**, *85*, 8085–8094.

(98) Steff, A. M.; Fortin, M.; Arguin, C.; Hugo, P. *Cytometry* **2001**, *45* (4), 237–243.

(99) Crouch, S. P. .; Kozlowski, R.; Slater, K. .; Fletcher, J. *Jounal Immunol. Methods* **1993**, *160*, 81–88.

(100) Moriyama, E. H.; Niedre, M. J.; Jarvi, M. T.; Mocanu, J. D.; Moriyama, Y.; Subarsky, P.; Li, B.; Lilge, L. D.; Wilson, B. C. *Photochem. Photobiol. Sci.* **2008**, *7* (6), 675.

(101) Tonder, A. Van; Joubert, A. M.; Cromarty, A. D. **2015**, 1–10.

(102) Vordermark, D.; Shibata, T.; Brown, J. M. *Neoplasia* **2001**, *3* (6), 527–534.
(103) Groulx, I.; Lee, S. **2002**, *22* (15), 5319–5336.

(104) Varia, M. A.; Calkins-Adams, D. P.; Rinker, L. H.; Kennedy, A. S.; Novotny, D. B.; Fowler, W. C.; Raleigh, J. A. *Gynecol. Oncol.* **1998**, *71* (2), 270–277.

(105) Evans, S. M.; Fraker, D.; Hahn, S. M.; Gleason, K.; Jenkins, W. T.; Jenkins, K.; Hwang, W. T.; Zhang, P.; Mick, R.; Koch, C. J. *Int. J. Radiat. Oncol. Biol. Phys.* **2006**, *64* (3), 922–927.

(106) Raleigh, J. A.; Miller, G. G.; Franko, A. J.; Koch, C. J.; Fuciarelli, A. F.; Kelly, D. A. *Br. J. Cancer* **1987**, *56* (4), 395–400.

(107) Gross, M.; Karbach, U.; Groebe, K.; Franko, A.; Mueller-Klieser, W. *Int J Cancer* **1995**, *16* (61 (4)), 567–573.

CHAPTER 2: QUANTIFYING OXYGEN IN PAPER-BASED CELL CULTURES WITH LUMINESCENT THIN FILM SENSORS

2.1 Introduction

Rapid cellular proliferation and the aberrant vasculature associated with solid tumors result in a microenvironment that is markedly different than surrounding tissue. Regions of low pH, increased interstitial fluid pressure, and decreased oxygen tension (i.e., hypoxia) act as selective forces that promote the development of a metastatic phenotype. [1–3] Hypoxia directly induces chemical signaling pathways through the regulation of hypoxia inducible factors. These transcription factors alter rates of cellular metabolism and proliferation, promote the metastasis of tumorigenic cells, and increase resistance to chemo- and radiation-based treatments.[4–8]

Two recent studies found oxygen, in addition to orchestrating transcriptional and phenotypic changes in the cell, has chemotactic properties.[9,10] Both studies showed A549 cells—adenocarcinoma epithelial cells derived from human alveoli—preferentially move along an oxygen gradient. Tung and colleagues found the A549 cells, when cultured as a monolayer in a microfluidic channel containing a static oxygen gradient, migrated to regions of lower oxygen tension.[9] Whitesides and colleagues found the A549 cells invaded regions of higher oxygen tension when cultured in a three-dimensional (3D) format.[10] These cultures were prepared by sandwiching a paper scaffold, which contained cells suspended in a hydrogel, between scaffolds containing only hydrogel. This stack formed a thick, tissue-like culture, which was placed

holder that limited the exchange of fresh medium into the culture and resulted in the formation of an oxygen gradient spanning the thickness of the stack.

The diffusion-limited environment formed in the 3D paper-based cultures mimic the microenvironment of a solid tumor, because gradients of nutrients, waste products, and signaling molecules result from cellular metabolism and lack of exchange with the nutrient-rich culture medium. Previous works have relied on cellular responses (e.g., viability, directed invasion, and hypoxia inducible transcripts) to confirm the presence of *in situ*-generated oxygen gradients.[10–13] These responses allowed for relative comparisons of oxygen tension throughout the culture, but do not directly quantify the shape or steepness of the oxygen gradients in the paper-based cultures. To better correlate cellular response with the formation of oxygen gradients in paper-based cultures, there is a need for a sensor that: detects small changes in oxygen tension, especially in the regions associated with hypoxia (0 – 10 mmHg); quickly responds to changes in oxygen tension, to provide good temporal resolution; and possesses good spatial resolution to provide an accurate picture of the gradient.

Optical-based sensors, unlike electrochemical analogs, are preferred for continuous monitoring ("sensing") of oxygen because they do not consume oxygen or generate byproducts that can alter the chemical composition of the culture environment.[14–17] When encapsulated in biocompatible materials (e.g., sol-gels or cross-linked matrices), these oxygen-sensitive dyes are compatible with the prolonged culture of mammalian cells and have been used to measure cellular oxygen consumption,[18] intracellular oxygen concentrations,[17,19] and interstitial oxygen gradients.[20–22] Integration of these dyes into microfluidic devices has provided a quantitative means of mapping oxygen gradients formed in a channel,[5,20–25] and has elucidated the temporal and spatial consumption of oxygen in static cultures.[18,26]

In this work, we prepared polystyrene thin films containing palladium tetrakis (pentafluorophenyl)porphyrin (PdTFPP) molecules, which are dynamically quenched by oxygen. We calibrated the oxygen sensing films, which had a linear response between 0 and 160 mmHg O_2 and an overall sensitivity (I_0/I_{160}) of ~35. Placing the oxygen sensing film in contact with the cell-containing paper scaffolds allowed us to measure changes of oxygen tension in the culture through changes in the luminescence intensity of the film. We prepared paper-based scaffolds with 11 x 2.5 mm channels (**Fig. 2.1**); the scaffolds were wax patterned, providing defined hydrophilic regions that readily wick cell-laden hydrogels. We limited the free exchange between the paper-scaffolds and the culture medium to discrete locations along the channels, causing chemical gradients to form laterally along the scaffold. This format allowed us to monitor changes in the luminescence of the oxygen sensing film with a fluorescence microscope. Placing the oxygen sensing films in contact with paper-based scaffolds containing fluorescently labeled cells allowed us to measure the spatial and temporal evolution of the oxygen gradient in the culture with respect to cell location. We used the oxygen gradient profiles obtained at different times to estimate the cellular oxygen consumption rate of the cells in different locations of the channel.

2.2 Materials and Methods

2.2.1 Thin film preparation

Polystyrene thin films were prepared by combining stock solutions of 25% (w/w) polystyrene (280,000 MW, Sigma-Aldrich) in toluene (Fisher Scientific) and 4 mM PdTFPP (Sigma-Aldrich) in toluene to make a working solution of 1 mM PdTFPP. The working solution was pipetted onto an 18 mm round glass coverslip (Warner Instruments) in 0.5 mL aliquots, and

then spin coated in a two-step process: i) 2,000 rpm for 3 sec, ii) 5,500 rpm for 2.5 sec. The thin films were placed under vacuum overnight to ensure complete removal of solvent and then sterilized by ultraviolet (UV) irradiation for 1 hr prior to usage. New thin films were prepared for each experiment. Film thickness was measured with a stylus profilometer (KLA Tencor P-6).

2.2.2 Sensor characterization

Sensors were calibrated in polydimethylsiloxane (PDMS) flow cells that were prepared by pouring a degassed mixture (10:1 ratio) of PDMS prepolymer and curing agent (Sylgard 184, Dow-Corning) into a 3D printed acrylonitrile butadiene styrene (ABS) mold. The PDMS was cured overnight at 50 ºC. The ABS mold was designed with a web-based computer assisted design application, TinkerCAD, and printed with a Makerbot® Replicator 2.

The PDMS flow cells were bonded to 75 mm glass microscope slides (Fisher Scientific) with uncured PDMS. Oxygen concentrations in the flow cell were modulated by controlling the flow rates of a two-gas mixture: balanced air with 5% CO_2, and a 95% N_2 with 5% CO_2 gas. The complete apparatus is depicted in **Fig. 2.2**. A polystyrene thin film without dye was used as a blank to account for background signal arising from the experimental setup. Reported emission intensities are the average of three locations along three different sensors.

2.2.3 Cell culture

MDA-MB-231 cells (ATCC) were transduced with lentiviral particles (LPP-eGFP-Lv105-025, GeneCopoeia) to constitutively express enhanced green fluorescent protein (M231-eGFP). The cells were transduced according to the manufacturer's protocol, and maintained in puromycin-containing medium (1 μg/mL). The cells were cultured in RPMI 1640 medium

supplemented with 10% (v/v) fetal bovine serum and 1% (v/v) penicillin-streptomycin. M231-eGFP cells were maintained at 5% CO_2 and 37 ºC, and their medium was exchanged every 48 hr. The cells were passed when the culture reached 70-80% confluency: the cells were detached from their tissue culture flask with Trypsin-EDTA (5 minutes, 37ºC), washed with serum-containing medium, pelleted, and cultured in a fresh flask at the appropriate dilution. All cell culture reagents, unless otherwise stated, were acquired from Gibco, Life Technologies.

2.2.4 Paper-based scaffold preparation

Paper-based scaffolds were prepared by wax patterning sheets of Whatman 105 lens paper with a ColorQube 8570 printer (Xerox). The scaffolds were wax-patterned on both sides, cured for 15 min at 150 ºC, and then sterilized with UV light overnight. Two designs were used in this work: i) a "channel scaffold", which contained three 11 x 2.5 mm elliptical zones, and ii) an "imprint scaffold", which contained three 3 x 2.5 mm rectangular zones. The different paper scaffolds are portrayed in **Fig. 2.1**. Detailed schematics of each design are included in **Fig. A2.1**.

Cellulose acetate sheets (overhead transparency, Staples) were cut using a Silver Bullet® cutting machine. The sheets were autoclaved before use. Detailed schematics of the cellulose acetate sheets are provided in **Fig. A2.2**.

2.2.5 Sensor cytotoxicity

Cytotoxicity assays were performed in paper-based scaffolds containing nine circular zones, 3 mm in diameter, in a 3 x 3 arrangement. Corresponding cellulose acetate sheets were designed to contain five 3 mm diameter circles, which allowed for the free exchange between the culture medium and the cell-containing zones. The culture setup used in these experiments, as

well as detailed schematics of the paper-based scaffolds, cellulose acetate sheets, and custom stainless-steel holder are provided in **Fig. A2.3**.

The paper-based scaffolds and cellulose acetate sheets were prepared as described in section 2.2.4. Three different glass supports were used in this assay to distinguish which component (if any) of the oxygen sensing films were cytotoxic: i) an 18 mm diameter glass coverslip; ii) an 18 mm diameter glass coverslip with a polystyrene thin film; and iii) an 18 mm diameter glass coverslip with a PdTFPP-containing polystyrene film (i.e., an oxygen sensor).

Prior to seeding M231-eGFP cells into the scaffolds, the cells were detached from their culture flask and resuspended in Matrigel (Corning) at a density of 75,000 cells/μL. Cell suspensions were stored on ice to prevent gelation during the seeding process. Five zones of the scaffold, which corresponded to the openings cut in the cellulose acetate film, were seeded with 0.5 μL of cells suspended in Matrigel. The remaining four zones were seeded with 0.5 μL of Matrigel. After seeding, the scaffolds were incubated in culture medium overnight (37ºC, 5% CO_2) and assembled into stacks the following day. Stacks were layered—cellulose acetate sheet (top), cell-containing paper-based scaffold, glass support (bottom)—enclosed in the custom stainless-steel holder and incubated for 24 or 48 hr in culture medium at 37 ºC in 5% CO_2.

The stacks were disassembled, and the paper-based scaffolds were imaged on a Typhoon 9400 variable mode laser scanner (GE Healthcare): the M231-eGFP cells were imaged with a 488 nm laser and a 526 nm short pass filter. The fluorescence intensities of the cell-containing zones in a single scaffold were measured with ImageJ[27] and averaged; the average fluorescence intensity of the zones containing only Matrigel was used as a background subtraction. All intensities were normalized to an additional set of seeded scaffolds that were measured after

overnight incubation in medium. Measurements were taken across three different cell passages, with each passage including 5 replicates.

2.2.6 Cell culture with sensor integration

Prior to seeding M231-eGFP cells into paper scaffolds, the cells were detached from their culture flask and resuspended in Matrigel (Corning) at a cell density of 170,000 cells/µL. The suspensions were stored on ice to prevent gelation during the seeding process. The rectangular regions of the imprint scaffolds were seeded with 0.44 µL of cell suspension, and the channel scaffolds seeded with 1.62 µL of Matrigel. Seeded scaffolds were incubated in medium overnight, and assembled into stacks the following day. Each stack consisted of a cellulose acetate sheet (top), a cell-containing imprint scaffold, a Matrigel-containing channel scaffold, and an oxygen sensing film on a glass coverslip (bottom). The entire stack was placed in a custom-made stainless-steel holder (**Fig. 2.1**). Assemblies were maintained at room temperature and the reported values represent averaged values from three different channels. Detailed schematics of the stainless-steel holders are provided in **Fig. A2.4**.

2.2.7 Image acquisition and processing

Fluorescence intensities of the M231-eGFP cells and the oxygen sensors, assembled in the holder, were imaged with an inverted microscope (Axiovert 40 CFL, Zeiss) equipped with a mercury arc lamp light source. The M231-eGFP cells were imaged with 470 ± 20 nm light and a 540 ± 25 nm emission filter. The oxygen sensors were excited with 546 ± 12 nm light and the emission was filtered with a 590 nm long pass filter. Images were captured with a monochrome

12-bit camera (QIC-F-M-12-C, QImaging) with 4X (0.1 NA) objective at an exposure time of 280 ms. Images were processed with ImageJ.[27]

2.2.8 Statistical Analysis

All reported values are the average and standard deviation of at least 3 replicates. Data sets were analyzed with Graphpad Prism v.6.07: a two-way ANOVA with Tukey's multiple comparison post-test was used to compare different data sets. A p-value of < 0.05 was considered significant.

2.3 Results and Discussion

2.3.1 Oxygen sensor characterization

Palladium- and platinum-based metalloporphyrins have been widely used for oxygen sensing due to their commercial availability, solvent compatibility, and large Stokes shift.[28–30] We chose PdTFPP to quantify oxygen tension in the paper-based cultures, because Pd(II)-based metalloporphyrins exhibit longer luminescence lifetimes than Pt(II)-based dyes, resulting in an increased sensitivity to oxygen;[31] and the pentafluorophenyl molecules appended to the porphyrin ring greatly improve the photostability of the dye.[28] A number of support matrices have been previously described for Pt(II)- and Pd(II)-based dyes (Table 2.1); we chose polystyrene because it is optically clear, stable in aqueous solutions, compatible with cell culture,[26,32,33] and moderately permeable to oxygen. Polystyrene has an oxygen permeability coefficient, *P*, of 0.88×10^{-15} mol/sN;[30] increased permeability of the support matrix coincides with larger diffusion coefficients, and can decrease the spatial resolution of the sensor.

Oxygen sensors were prepared by spin coating mixtures of PdTFPP and polystyrene dissolved in toluene onto of 18-mm round glass coverslips. The resulting films (3.61 ± 0.07 μm thick) were ideal for our application because they were easily incorporated into our culture setup (**Fig. 2.1**). Oxygen can rapidly diffuse through these thin films, decreasing the response time of the film by decreasing the time needed for the film to equilibrate with the apposing environment. Response times were measured to be on the order of ~15 secs to fully equilibrate. Glass coverslips were used as a support substrate for the polystyrene thin films for three reasons: i) they provide rigidity to the sensor; ii) they are impermeable to oxygen and medium, which prevents oxygen diffusion into the assembled culture and maintains gradients formed within the scaffolds; and iii) they are optically transparent and compatible with fluorescence microscopy, allowing us to measure both the luminescence intensity of the oxygen sensing film and fluorescence intensity of the M231-eGFP cells in the paper-based scaffolds.

To calibrate the sensor's response to different oxygen tensions, we placed the sensors in the gas flow apparatus depicted in **Fig. 2.2**. The relationship between oxygen tension and luminescence intensity was determined with a Stern-Volmer relationship, modeled by the equation:

$$\frac{I_0}{I} = 1 + K_{sv}[O_2] \qquad \text{Eq[2.1]}$$

I_0 and I represent the emission intensity of the film in the absence and presence of oxygen, respectively; K_{SV} is the Stern-Volmer constant relating emission intensity to oxygen concentration. We measured the luminescence intensity of the film from 0 to 160 mmHg, and derived a K_{sv} = 0.239 ± 0.003 mmHg O_2^{-1} from the Stern-Volmer plot (**Fig. 2.3A**). The sensitivity of these films surpasses values previously reported for Pd(II)- and Pt(II)-based dyes encapsulated in polystyrene (Table 2.1).[26,28,34,35] The standard deviation of the luminescence

intensities of the oxygen sensing films increased with increasing oxygen tension. This trend is expected, as emission intensity is non-linearly related to oxygen tension and significant quenching at higher oxygen tensions lead to diminished differences in signal. While this variation in intensity limits our ability to differentiate oxygen tensions at high concentrations, the sensors provide a linear response across oxygen tensions used for cell culture, and is particularly sensitive to small changes in oxygen tension near hypoxic conditions (i.e., values < 10 mmHg).

To ensure cell culture conditions did not affect the responsiveness of the oxygen sensing films, we incubated the sensor for 7 days in a flow cell containing medium collected from an overly confluent culture flask. This setup emulated the nutrient-exhausted environment seen in static, diffusion-limited cultures. After 7 days, the luminescence intensity of the films in oxygen tensions ranging from 0 to 79 mmHg was measured. No significant difference in emission intensity was observed for films incubated in culture medium and films maintained in dry conditions (**Fig. 2.3B**). Furthermore, there was no significant difference between emission intensities of sensors measured prior to and after 7 days of incubation in cell medium. These results indicate a number of observations: i) the gas-phase Stern-Volmer calibration is suitable for quantifying oxygen tensions in liquids; ii) the sensors are stable in culture medium for at least one week, and iii) relative to oxygen, soluble components of the culture medium do not impact sensor response.

The photostability of the oxygen sensing films was also evaluated. Sensors were placed in flow cells and continuously illuminated for 1 hr at 0 or 160 mmHg O_2. Images were taken in 1 min increments across three sensors, and the intensities were normalized to t = 0 (**Fig. 2.3C**). After 1 hr, there was no significant change in emission at either oxygen tension indicating that

these sensors are photostable. These results agree with a previous study done with PtTFPP in polystyrene, which found these films were stable after 50 hr of continuous illumination.[28]

2.3.2 Sensor cytotoxicity

To ensure that the sensors were compatible with cell culture, we seeded M231-eGFP cells in paper scaffolds; placed them in contact with a glass coverslip, a glass coverslip with a polystyrene thin film, or a glass coverslip with a PdTFPP-containing polystyrene thin film (i.e., an oxygen sensing film); and cultured the cells for 24 or 48 hr. The experimental setup is provided in **Fig. A2.3a**. After incubation, the devices were disassembled and fluorescence intensities of the seeded zones measured with a fluorescence flatbed scanner. Others have demonstrated that the emission intensity of fluorescently labeled cells seeded in paper scaffolds is directly related to total number of cells present,[12] and decreases in green fluorescent protein (GFP) emission can be used to monitor cell death.[36]

No significant difference in fluorescence intensity was observed for cells cultured in the presence of the glass, polystyrene, or the PdTFPP-containing polystyrene substrates after 24 or 48 hr of culture (**Fig. 2.4**). The fluorescence intensity of each zone, prior to and post-culture, were also not significantly different. These results suggest the oxygen sensing films are not cytotoxic over the duration of our experiments.

2.3.3 Oxygen tension in channel culture

To visualize the formation of an oxygen gradient in a diffusion-limited environment, we assembled the cultures shown in **Fig. 2.1**. In this setup a cellulose acetate sheet, an imprint scaffold, a channel scaffold, and an oxygen sensing film were stacked together and enclosed in a

stainless-steel holder. The cellulose acetate sheet and the glass coverslip are both impermeable to oxygen and liquids; these materials allowed us to spatially limit nutrient and waste exchange between the culture and culture medium to one end of the channel. Each imprint scaffold provided a rectangular region in which we could reproducibly seed cells and place them in the same position along the channel. The Matrigel-filled channels provided a path for nutrients and waste to diffuse along the enclosed stack. In this arrangement, the cell-seeded imprint region at the center of the channel should act as an oxygen sink, and cause an oxygen gradient to form across the length of the channel from source (opening in the cellulose acetate sheet) to sink.

The assembled devices were incubated for 48 hr, and images of the M231-eGFP cells and the oxygen-sensing films were obtained with an inverted fluorescence microscope. The captured images provided a 2D landscape of oxygen tension across the cell-seeded imprint region. To reduce the 2D images into a one-dimensional dataset, we used ImageJ to generate "column average plot profiles". The readout of these profiles is the average intensities of all y-pixels per x-pixel in a selected region of interest (ROI). We chose an ROI (4.6 x 1.5 mm) that spanned the width of the channel, and maintained the size and location of the ROI between images.

Images of the oxygen sensing film allowed us to quantify spatial changes of oxygen tension across the channel **(Fig. 2.5A**); acquiring images at different time points allowed us to quantify the temporal changes of the oxygen tension across the channel. The oxygen profiles generated across the length of the channel resemble those predicted for spheroids and solid tumor masses.[37,38] Oxygen gradients also formed along the borders of the cell-seeded imprint region, and the interior portion of the cell-seeded region consistently reached oxygen tensions of less than 10 mmHg (hypoxia), similar to regions of a tumor greater than ~50 μm from a blood vessel.[39] Column average plot profiles of the channels (**Fig. 2.5B**) indicate the *in situ* generated

oxygen gradients are reproducible, rapidly formed (less than 1 hr), and persistent for up to 48 hr. One distinction to note is the difference in error between the imprint region's borders proximal and distal to the oxygen source, which arose from averaging gradients which were not completely overlapped. This highlights the need to further characterize parameters which influence the formation of oxygen gradients, but confirms the ability of the oxygen sensors to discern spatial and temporal differences in oxygen.

The stability of the gradients suggests the culture, during the course of the experiment, was under steady state conditions in which the diffusive flux of oxygen into the cell seeded region, J_{in}, was equal to consumption in that same region, J_{out}. Diffusive flux into the system can be approximated using the one-dimensional steady state solution to Fick's first law:

$$J_{in} = -D\frac{\partial C}{\partial x} \qquad \text{Eq.[2.2]}$$

where D is the diffusion coefficient of oxygen in Matrigel (1.5×10^{-5} cm^2/s),[15] and $\frac{\partial C}{\partial x}$ is the change of oxygen tension running laterally across the channel. Oxygen flux out of the system due to cellular consumption can be characterized with:

$$J_{out} = Q\rho h \qquad \text{Eq.[2.3]}$$

where Q is the oxygen consumption rate per cell, ρ is the corrected volumetric cell density, and h is the length of the region in the channel being measured. To ensure gradients were formed by a static cell population, images of M231-eGFP cells were also obtained. The fluorescence intensity of the cell-containing regions did not change over the 48 hr period of the experiment (**Fig. 2.6**), indicating that the gradient profiles are maintained by the same total number of cells throughout the incubation. Under steady state conditions, equations [2.2] and [2.3] can be rearranged to solve for the oxygen consumption rate per cell (Q):

$$Q = \frac{-D\frac{\partial C}{\partial x}}{\rho h} \quad \text{Eq.[2.4]}$$

D is the experimentally determined diffusion coefficient of oxygen in Matrigel ($1.5x10^{-5}$ cm^2/sec).[15] The change of oxygen across the seeded region was determined from the linear portion of the oxygen gradient profiles (**Fig. 2.7**). The slopes of these gradients, converted to concentrations, are 170 ± 8 and 105 ± 6 μM/mm for the proximal and distal borders, respectively. Rather than using the volumetric cell density used for seeding each imprint zone, a corrected cellular volumetric density value, ρ, was used for calculations. This correction was done because the cell distribution was not uniform across the imprint region (**Fig. 2.7**). To calculate the corrected cellular volumetric density, two assumptions were made: i) that the cell population did not change over time, validated by the constant fluorescence intensity of the M231-eGFP cells measured throughout the 48 hr experiment (**Fig. 2.6**). ii) That the cellular distribution is uniform along the width (y-axis) of the imprint region. Given the uniformity of the cell distribution along the length of the imprint region, this assumption appears reasonable. By making this second assumption, the column average plot profile of the M231-eGFP cells can be integrated to spatially quantify cells along the length of the channel. Using the boundaries established for the linear range of the oxygen profiles (**Fig. 2.7**), the total cells in this region were calculated to be 3400 ± 500 and 4900 ± 700 cells for the proximal and distal borders, respectively. A corrected volumetric density is calculated using the imprint dimensions of 0.25 x 2.5 x 0.07 mm (two scaffolds are stacked for this assay, and each scaffold has a thickness of 35 μm), in this case, the length dimension is determined by the length of the linear portion of the oxygen gradients (**Fig. 2.7**, 0.25 mm) and is represented by *h* in Eg. [2.3]. Having defined all pertinent variables, the oxygen consumption rates for the proximal and distal borders of the imprint region were $1.3 \pm 0.2 \times 10^{-17}$ and $0.56 \pm 0.08 \times 10^{-17}$ mol/cell•sec.

The calculated oxygen consumption rates are within the range of previously reported oxygen consumption rates of cancerous cells lines.[18,40] While the estimated values of cellular consumption suggest that cells at the distal edge are consuming oxygen at a slower rate than cells at the proximal front, further experiments are needed to determine the statistical significance of these differences. We also acknowledge that complimentary measurements—both extra- and intracellular—are needed to determine if the rates are of oxygen consumption are different. This data does demonstrate, however, that incorporating the oxygen sensing films into the paper-based cultures provides a means of quantifying the spatial and temporal changes of an oxygen gradient.

2.4 Conclusion

This work describes the preparation and characterization of an oxygen sensing film that, when imaged with a fluorescence microscope, provides spatial and temporal information about the oxygen gradients formed in three-dimensional cell cultures in paper-based scaffolds. These sensors, which are spin-coated onto 18 mm diameter glass supports, are polystyrene films containing an oxygen-sensitive metalloporphyrin dye, PdTFPP. Oxygen readily diffuses into these thin films, resulting in rapid changes in luminescence intensity with changes in the surrounding oxygen tension. The sensors are compatible with optical- and fluorescence-based microscopies, sensitive to small changes in oxygen tension (a K_{sv} of 0.239 ± 0.003 mmHg O_2) with a linear response between 0 and 160 mmHg O_2, photostable after 1 hr of continuous emission, and not cytotoxic. We utilized these oxygen sensitive films, after characterization, in conjunction with M231-eGFP cells to visualize oxygen gradients formed along cell-containing channels of paper-based scaffolds, whose free exchange with the culture medium was limited.

These oxygen gradients developed within 1 hr of culture assembly and were unchanged over a period of 48 hr. The steady state nature of this gradient allowed us to estimate oxygen consumption of the cells in different locations of the channel.

These sensors will allow us to determine the effects of culture conditions (e.g., cell density, cell type, distance from the source of oxygen) on the oxygen gradients established in the paper-based cultures. Establishing an analytical model relating these variables with oxygen gradients will afford better experimental control in the design of more complicated cultures.

2.5 Tables and Figures

Table 2.1 Pd(II)- and Pt(II)-based oxygen sensors

Matrix	Dye	Sensitivity (I_0/I_{air})	Ref
PDMS	PtTFPP	~120	18
PS	PdOEPK	9.5	33
	PtOEPK	3.76	
	PdTFPP	35	This work
	PtTFPP	1.9	29
PVC	PdOEPK	29	33
	PtOEPK	2.05	
PMMA	PdOEP	21	34
	PtOEP	1.78	

PS = polystyrene, PVC = poly(vinyl chloride), PMMA = poly(methyl methacrylate), OEP = octaethylporphyrin, OEPK = octaethylporphyrin ketone

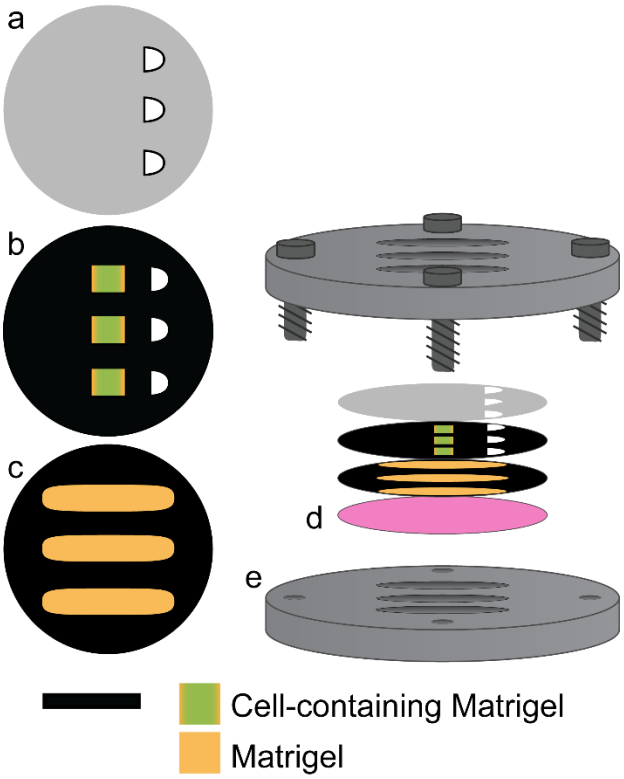

Figure 2.1 Schematic of the experimental setup used in this chapter. A layered structure consisting of: (a) a cellulose acetate film, which was cut to contain openings; (b) a wax-patterned sheet of paper containing rectangular zones in which suspensions of cells in hydrogel were seeded; (c) a wax-patterned paper containing channels, which were seeded with hydrogel. (d) An oxygen sensor was added to the bottom of the stack before it was placed in (e) a custom-made stainless-steel holder, which was held together with four screws. The glass backing of the oxygen sensing film and the cellulose acetate transparency allowed us to control exchange between the medium and the culture. Scale bar = 9 mm.

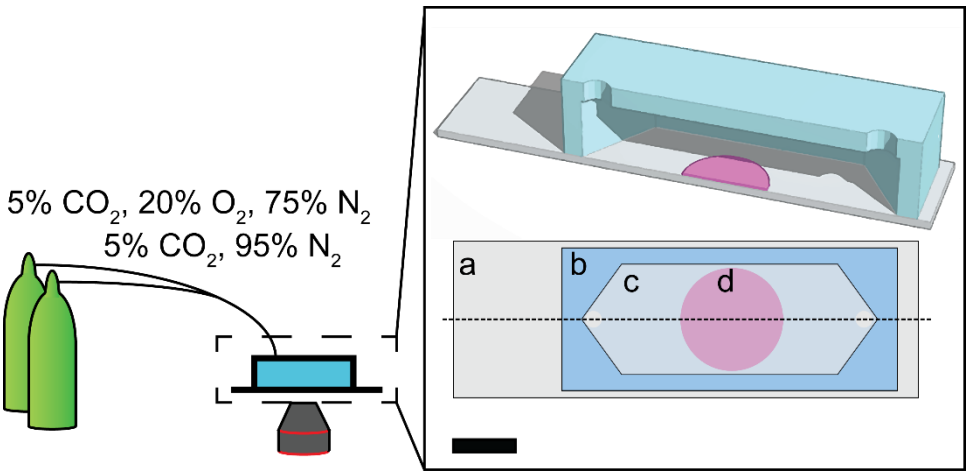

Figure 2.2 Schematic of the flow cell apparatus used to characterize the fluorescence intensity of the oxygen sensors exposed to different concentrations of oxygen. A mixture of two gases was introduced to the flow cell, and the fluorescence intensity of the film was measured from images captured on an inverted fluorescence microscope. The figure inset is a (a) glass microscope slide to which a (b) PDMS flow cell was bonded. The (c) center of the flow cell is hollow and the gas mixture introduced through one of the two ports. An (d) oxygen sensor was placed inside the flow cell. The dotted-line of the top-view image indicates the beginning of the cross-sectional image. Scale bar = 10 mm.

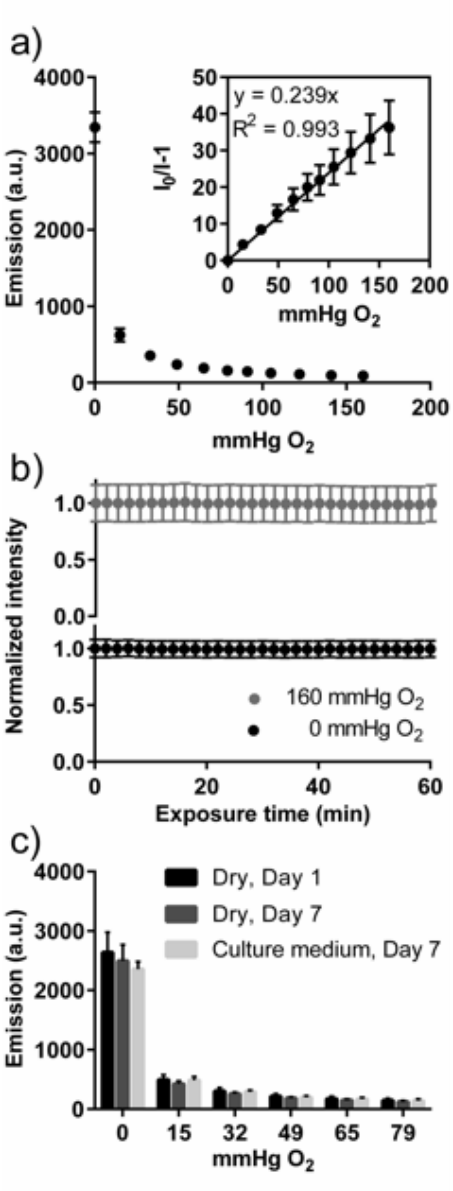

Figure 2.3 Sensor characterization. a) Fluorescence intensity of the PdTFPP-containing thin films exposed to different concentrations of oxygen, and the Stern-Volmer plot (inset) with a linear regression plot used to derive the K_{sv}. Each data point is the average of nine measurements from three independently prepared thin films; the error bars represent a standard deviation. b) Emission intensities of sensors stored for 7 days in culture medium or in a dark, dry environment. No significant change in emission was measured. Each data bar represents the average of three independently prepared thin films; error bars represent a standard deviation. c) Photostability of the sensors, exposed to 0 or 160 mmHg O_2, under continuous illumination for 1 hour. Images were taken in one-minute increments, and no significant change in emission was measured. Each data point is the average of three measurements from three independently prepared thin films; error bars represent a standard deviation.

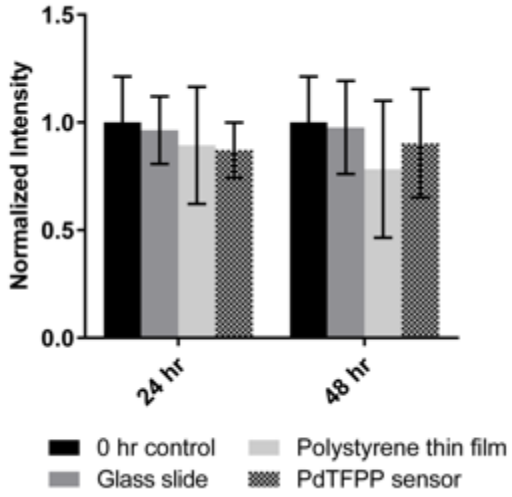

Figure 2.4 Sensor cytotoxicity. Paper scaffolds seeded with M231-eGFP cells were placed in contact with a glass support—a glass coverslip, a coverslip coated with a polystyrene thin film, or an oxygen sensor—and enclosed in a metal holder. The assembled culture was incubated for 24 or 48 hr. After incubation, the cultures were disassembled and the fluorescence intensity of the cell-containing regions measured. Intensities were normalized to scaffolds measured prior to stacking, and no significant difference was measured between any data set. These results indicate that the oxygen sensors are not cytotoxic. Each bar is the average of fifteen measurements from three independently prepared experiments; error bars represent a standard deviation.

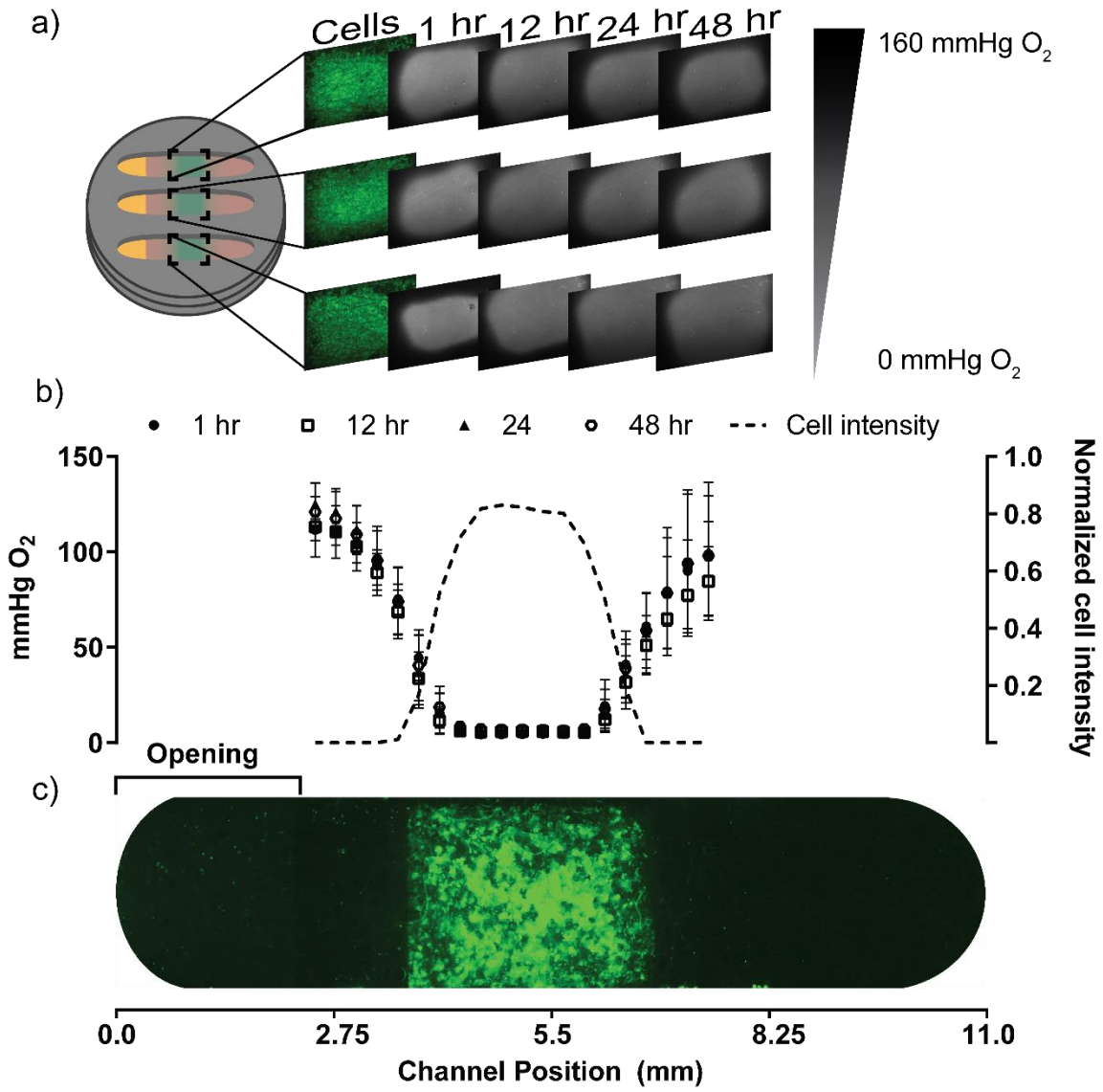

Figure 2.5 *In situ* oxygen quantification. a) Fluorescence images of the assembled holders, detailed in **Fig. 2.1**, were acquired at different time points of a 48 hr experiment. Images of both the M231-eGFP cells and the oxygen sensor were taken at each time interval. b) The fluorescence intensity across the channel (i.e., the oxygen gradient), measured along the channel for each time point. Gradients were overlaid with the normalized cell intensity at 48 hr (dashed line) to spatially correlate the oxygen gradient profile with cell location. Each data point is the average of three replicate experiments. The bars correspond to a standard deviation. c) A representative fluorescence micrograph of the M231-eGFP cells in the assembled channel.

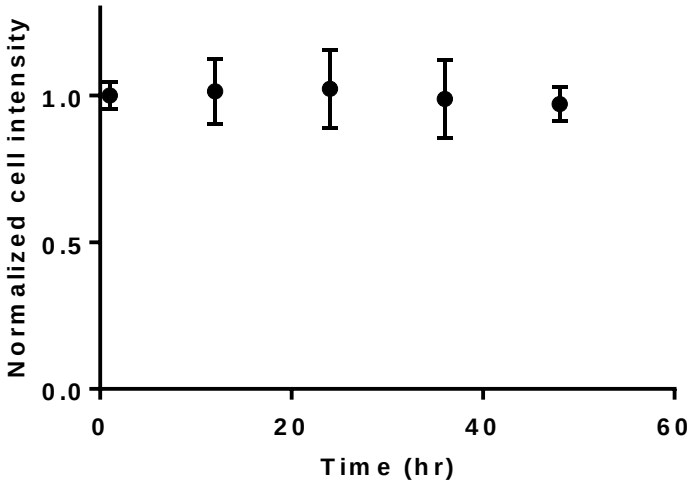

Figure 2.6 Average fluorescence intensity of M231-eGFP cells during gradient analysis. M231-eGFP fluorescence intensities along the imprint regions were normalized to background signal, and then normalized to the fluorescence intensity of the cells after 1 hr of incubation. No significant change in intensity was measured throughout the 48 hr incubation, and indicates that the total cell populations are unchanging after 2 days. This data further corroborates the biocompatibility of the oxygen sensors previously measured in the cytotoxicity assay. Each data point is the average of three measurements from three independently prepared thin films; error bars represent a standard deviation.

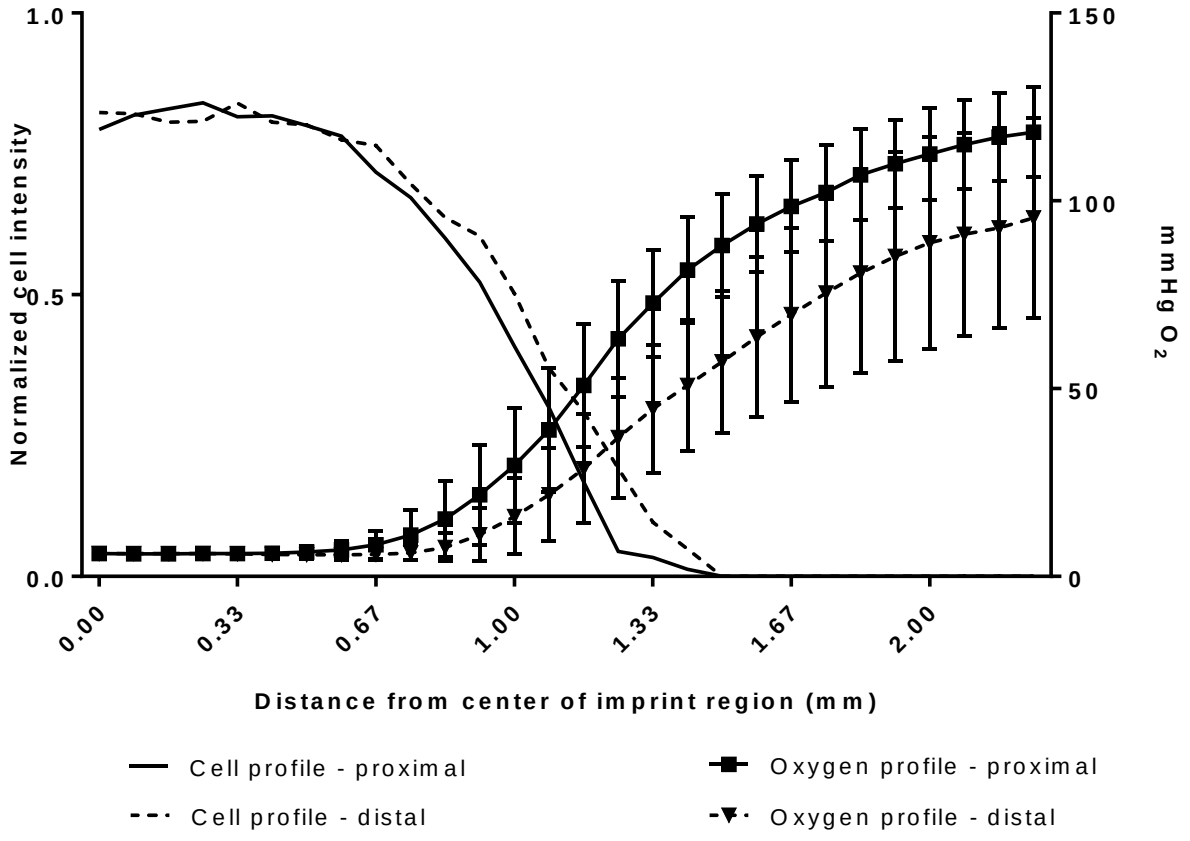

Figure 2.7 Overlay of the oxygen gradients formed at the cell fronts proximal and distal to the cellulose acetate openings in the paper-based cultured. To better visualize differences between the proximal and distal borders of the imprint regions, cell fronts and their respective oxygen gradients were overlaid. The distributions of each cell front indicate that cells are not seeded uniformly along the edges, which causes the resulting oxygen gradients to deviate from linearity. To simplify cellular oxygen consumption rate calculations, only the linear portions of the oxygen gradients—from 1 to 1.25 mm for the proximal, and 1.17 to 1.33 mm for the distal borders—were used to calculate the change of oxygen along the proximal and distal borders ($\frac{\partial C}{\partial x}$), which were 136 ± 6 and 84 ± 5 mmHg O_2/mm, respectively.

REFERENCES

(1) Lunt, S. J.; Chaudary, N.; Hill, R. P. *Clin. Exp. Metastasis* **2008**, *26* (1), 19–34.

(2) Rofstad, E. K.; Galappathi, K.; Mathiesen, B. S. *Neoplasia* **2014**, *16* (7), 586–594.

(3) Gatenby, R. A.; Gillies, R. J. *Nat. Rev. Cancer* **2004**, *4* (11), 891–899.

(4) Rexiusa, M. L.; Mauleona, G.; Malikb, A. B.; Rehmanb, J.; Eddington, D. T. *Natl. Institutes Heal.* **2010**, *5* (8), 3045–3056.

(5) Polinkovsky, M.; Gutierrez, E.; Levchenko, A.; Groisman, A. *Lab Chip* **2009**, *9* (8), 1073.

(6) Sullivan, R.; Graham, C. H. *Cancer Metastasis Rev.* **2007**, *26* (2), 319–331.

(7) Harris, A. L. *Nat. Rev. Cancer* **2002**, *2* (1), 38–47.

(8) Semenza, G. L. *N. Engl. J. Med.* **2012**, *365* (6), 537–547.

(9) Chang, C.-W.; Cheng, Y.-J.; Tu, M.; Chen, Y.-H.; Peng, C.-C.; Liao, W.-H.; Tung, Y.-C. *Lab Chip* **2014**, *14* (19), 3762–3772.

(10) Mosadegh, B.; Lockett, M. R.; Minn, K. T.; Simon, K. A.; Gilbert, K.; Hillier, S.; Newsome, D.; Li, H.; Hall, A. B.; Boucher, D. M.; Eustace, B. K.; Whitesides, G. M. *Biomaterials* **2015**, *52* (1), 262–271.

(11) Mosadegh, B.; Dabiri, B. E.; Lockett, M. R.; Derda, R.; Campbell, P.; Parker, K. K.; Whitesides, G. M. *Adv Heal. Mater* **2014**, *3* (7), 1036–1043.

(12) Derda, R.; Laromaine, A.; Mammoto, A.; Tang, S. K. Y.; Mammoto, T.; Ingber, D. E.; Whitesides, G. M. *Proc. Natl. Acad. Sci. U. S. A.* **2009**, *106* (44), 18457–18462.

(13) Derda, R.; Tang, S. K. Y.; Laromaine, A.; Mosadegh, B.; Hong, E.; Mwangi, M.; Mammoto, A.; Ingber, D. E.; Whitesides, G. M. *PLoS One* **2011**, *6* (5).

(14) Milosevic, M.; Fyles, A.; Hedley, D.; Hill, R. *Semin. Radiat. Oncol.* **2004**, *14* (3), 249–258.

(15) Colom, A.; Galgoczy, R.; Almendros, I.; Xaubet, A.; Farré, R.; Alcaraz, J. *J. Biomed. Mater. Res. - Part A* **2014**, *102* (8), 2776–2784.

(16) Feng, Y.; Cheng, J.; Zhou, L.; Zhou, X.; Xiang, H. *Analyst* **2012**, *137* (21), 4885.

(17) Park, E. J.; Reid, K. R.; Tang, W.; Kennedy, R. T.; Kopelman, R. *J. Mater. Chem.* **2005**, *15* (27–28), 2913.

(18) Thomas, P. C.; Halter, M.; Tona, A.; Raghavan, S. R.; Plant, A. L.; Forry, S. P. *Anal. Chem.* **2009**, *81* (22), 9239–9246.

(19) Koo, Y. E. L.; Cao, Y.; Kopelman, R.; Koo, S. M.; Brasuel, M.; Philbert, M. A. *Anal. Chem.* **2004**, *76* (9), 2498–2505.

(20) Lo, J. F.; Sinkala, E.; Eddington, D. T. *Lab Chip* **2010**, *10* (18), 2394–2401.

(21) Acosta, M. a; Jiang, X.; Huang, P.-K.; Cutler, K. B.; Grant, C. S.; Walker, G. M.; Gamcsik, M. P. *Biomicrofluidics* **2014**, *8* (5), 54117.

(22) Peng, C.-C.; Liao, W.-H.; Chen, Y.-H.; Wu, C.-Y.; Tung, Y.-C. *Lab Chip* **2013**, *13* (16), 3239.

(23) Wang, L.; Liu, W.; Wang, Y.; Wang, J.; Tu, Q.; Liu, R.; Wang, J. *Lab Chip* **2013**, *13* (4), 695–705.

(24) Grist, S. M.; Oyunerdene, N.; Flueckiger, J.; Kim, J.; Wong, P. C.; Chrostowski, L.; Cheung, K. C. *Analyst* **2014**, *139* (22), 5718–5727.

(25) Chen, Y.-A.; King, A. D.; Shih, H.-C.; Peng, C.-C.; Wu, C.-Y.; Liao, W.-H.; Tung, Y.-C. *Lab Chip* **2011**, *11* (21), 3626.

(26) Sinkala, E.; Eddington, D. T. *Lab Chip* **2010**, *10* (23), 3291.

(27) Rayband, W. National Institutes of Health, Bethesda, Maryland, USA.

(28) Lee, S.-K.; Okura, I. *Anal. Commun.* **1997**, *34* (June), 185–188.

(29) Koren, K.; Borisov, S. M.; Klimant, I. *Sensors Actuators, B Chem.* **2012**, *169*, 173–181.

(30) Wang, X.; Wolfbeis, O. S. *Chem. Soc. Rev.* **2014**, *43* (10), 3666–3761.

(31) Russell, M. D.; Gouterman, M. *Spectrochim. Acta Part A Mol. Spectrosc.* **1988**, *44* (9), 857–861.

(32) Nock, V.; Blaikie, R. J.; David, T. *Lab Chip* **2008**, *8* (8), 1300.

(33) Lam, R. H. W.; Kim, M.; Thorsen, T. *Society* **2009**, *81* (14), 5918–5924.

(34) Hartmann, P.; Trettnak, W. *Anal. Chem.* **1996**, *68* (15), 2615–2620.

(35) Mills, A.; Lepre, A. *Anal. Chem.* **1997**, *69* (22), 4653–4659.

(36) Steff, A. M.; Fortin, M.; Arguin, C.; Hugo, P. *Cytometry* **2001**, *45* (4), 237–243.

(37) Cochran, D. M.; Fukumura, D.; Ancukiewicz, M.; Carmeliet, P.; Jain, R. K. *Ann. Biomed. Eng.* **2006**, *34* (8), 1247–1258.

(38) Grimes, D. R.; Kelly, C.; Bloch, K.; Partridge, M. *J. R. Soc. Interface* **2014**, *11* (92), 20131124.

(39) Herst, P. M.; Berridge, M. V. *Biochim. Biophys. Acta - Bioenerg.* **2007**, *1767* (2), 170–177.

CHAPTER 3: BLOCCS, AN INEXPENSIVE AND MODULAR FLUIDIC CHIP CAPABLE OF GENERATING LINEAR OXYGEN GRADIENT IN THREE-DIMENSIONAL CULTURES

3.1 Introduction

Oxygen plays a vital role in maintaining cellular homeostasis, acting as both a metabolite and a transcriptional regulator. Low physiological oxygen tensions (i.e., hypoxia) occur during the development of normal tissue, promoting angiogenesis and cellular movement.[1] Hypoxia also occurs in disease states associated with blood vessel occlusion or high rates of cellular proliferation.[2,3] Cellular reprogramming in response to oxygen stresses is coordinated by hypoxia-inducible factors (HIFs). Under low oxygen tensions, the α-subunits are stabilized within the cytosol and translocate to the nucleus to dimerize with a HIF-1β subunit.[4] Once HIF transcription complexes are assembled, they target genes with upstream hypoxia-responsive elements. In cancer cells, HIF-mediated gene products increase the cell's reliance on glycolysis,[5] increase the expression of angiogenic growth factors,[6] and halt cell-cycle progression.[7] The prevalence of hypoxia in poorly vascularized tumors have also implicated HIFs in cancer progression and increased mortality,[8,9] as prolonged exposure to hypoxic conditions promotes the development of chemoresistant and metastatic phenotypes.[10–12]

Hypoxia chambers have been widely used to study HIF activation and transcriptional regulation.[13–16] These devices allow cells to be cultured at defined oxygen tensions for prolonged periods of time. A previous study used hypoxia chambers to relate extracellular oxygen tensions to HIF stabilization within a number of cell lines, and found that tensions of less than 2% O_2 (15

mmHg) were necessary for HIF stabilization and accumulation in the nucleous.[17] This estimation, which was obtained from four different oxygen tensions, highlights a limitation of hypoxia chambers: only a single oxygen tension can be imposed across an individual culture, making it difficult to study a wide range of oxygen tensions in an efficient manner.

Rather than studying HIF stabilization under a single static oxygen tension, exposing cells to an oxygen gradient greatly increases the amount of information that can be derived from a single experiment. Microfluidic devices capable of imposing an experimentally controlled oxygen gradient across two-dimensional (2D) and three-dimensional (3D) cultures have been developed,[18,19] making this platform well suited for relating oxygen tension to HIF stabilization and downstream cellular responses. Recent examples of such devices have studied cancer cell invasion,[20,21] HIF stabilization and downstream expression,[22–24] and the production of reactive oxygen species[25] in oxygen gradients.

Microfluidic chip fabrication requires expertise and equipment not commonly found in tissue culture laboratories. Despite the multitude of microfluidic chips capable of precisely controlling oxygen gradients *in vitro*, engineering obstacles have hindered the widespread adoption of these devices.[26] For these devices to be widely adopted by laboratories pursuing biological questions centered around oxygen gradients and hypoxia, they must i) be simple to fabricate, assemble, maintain, and analyze; ii) allow easy manipulation of oxygen gradients, with or without the aid of digital flow controllers, and; iii) be able to support three-dimensional (3D) tissue-like culture environments. While there are examples of microfluidic devices in the literature that overcome the complexity of previous iterations,[22,27] they require cells be cultured as monolayers, which do not accurately recapitulate the morphology or behavior of cells in tissue.[28–30]

The *maker movement* and ready accessibility of tools such as 3D printers and laser cutters have empowered many laboratories to generate customizable devices and pieces of equipment.[31] Here we describe the fabrication and characterization of an easy-to-make, and inexpensive static culture device referred to as a **B**lock-**L**ayered **O**xygen-**C**ontrolling **C**hip (BLOCC). The device is constructed by stacking layers of laser-cut silicone and acrylic, (**Fig. 3.1**) and is readily modified to suit experimental needs by adjusting the design of an individual layer or rearranging the order of assembled layers. The gas-permeable silicone gaskets enabled the generation of oxygen gradients across 3D cultures within the device, and oxygen-sensing films were used to characterize the gradients. By incorporating a cell line engineered to express a fluorescent protein upon HIF activation, we are able to relate HIF transactivation to the oxygen tension in the local culture environment.

3.2 Materials and Methods

3.2.1 Cell lines and culture reagents

This study used both parental and engineered MDA-MB-231 cells (M231, American Type Culture Collection). The engineered cells (M231-HRE), which we detailed previously,[32,33] express mCherry fluorescent protein (mCHR) constitutively and enhanced green fluorescent protein (eGFP) under hypoxic conditions. The 5HRE/GFP plasmid[34] used to engineer the M231 cells was a gift from Martin Brown and Thomas Foster (Addgene plasmid # 46926).

All cells were maintained as monolayers at 37 ºC and 5% CO_2 in RPMI 1640 medium supplemented with 5% (v/v) fetal bovine serum and 1% (v/v) penicillin-streptomycin, until needed. Culture medium was changed every two days and the cells passaged at 70-80%

confluence. Unless otherwise stated, all reagents used for cell culture were obtained from Gibco (Life Technologies) and used as received.

3.2.2 Chip fabrication and assembly

Figure 3.1 outlines the fabrication and assembly of a BLOCC. Each component was purchased from McMaster-Carr and laser cut using 100% power, 10% speed, and 1000 ppi (Universal Laser Systems, ILS9.75). The inner acrylic components were cut from 0.25-inch-thick sheets of clear cast acrylic and the outer acrylic components were cut from 0.125-inch-thick sheets of clear cast acrylic. The silicone gaskets were cut from 0.03125-inch-thick sheets of 50A food-grade silicone. All components were sterilized by ultraviolet exposure for 1 h prior to culture assembly.

The BLOCC was loaded with cells then assembled in the following order. First, 1 µL of cell-free Matrigel (Corning) was loaded into the seeding region and allowed to gelate for 1 min. Next, 1 µL of a 2,000 cell/µL Matrigel suspension was loaded directly onto the gelated Matrigel. The medium reservoirs of the BLOCC were then filled with 1 mL of medium, and the entire device was held together with six 1-inch stainless steel screws with 4-40 threading and matching nuts (McMaster-Carr). The assembled BLOCCs were incubated for up to 72 h at 37 ºC. Prior to imaging cells within the BLOCCs, the top acrylic component was removed and the reservoir regions were washed twice with 1X PBS.

3.2.3 Oxygen gradient generation and quantification

Deoxygenated and oxygenated gasses were interfaced with the BLOCCs using a wall-plug design,[35] and flown through the channels at a rate of 35 cc/min. The deoxygenated gas

mixture contained 95% nitrogen and 5% carbon dioxide. Two different oxygenated gas mixtures were used: a high-oxygen mixture containing 75% nitrogen, 20% oxygen, and 5% carbon dioxide, and; a low-oxygen mix containing 90% nitrogen, 5% oxygen, and 5% carbon dioxide. All gasses were supplied and validated by Airgas.

Oxygen sensors were prepared by coating the bottom-most acrylic component of the BLOCC assembly (component G, **Fig. 3.1**) with a 3-µm-thick oxygen sensing film. Preparation and characterization of these oxygen sensing films were detailed previously.[36] Briefly, a 1 mM solution of palladium (II) tetrakis (pentafluorophenyl) porphyrin in a 18.75% (w/w) polystyrene-toluene solution was spun coat onto the acrylic component. Prior to usage, the oxygen sensor-coated acrylic components were sterilized by ultraviolet exposure for 1 h.

3.2.4 Image acquisition and analysis

Fluorescence micrographs of both the fluorescently labeled cells and the oxygen sensors were obtained on an Axiovert 40 CFL (Zeiss) inverted widefield fluorescence microscope equipped with a LED light source (wLS-LG-MB, QImaging) and monochrome 12-bit camera (QIC-F-12-C, QImaging). Fluorescein was imaged with a 470/20 nm excitation filter and 540/40 nm emission filter, with a 500 ms exposure. PI and the oxygen sensors were imaged with a 546/12 nm excitation filter and 590 nm long pass filter, with either a 600 ms or 1400 ms exposure, respectively. Transmitted light images were also taken and were used to identify the boundaries of individual cells within a single image. The Trainable Weka Segmentation plugin in FIJI was used to identify cell boundaries.[37–39] The percentage of viable cells was determined by dividing the number of fluorescein positive cells by the total number of cells measured in a

single image. Cells that were positive for both fluorescein and PI were considered dead and not included in the viable cell count.

Fluorescence micrographs of the M231-HRE cells were obtained on an Olympus IX70 inverted widefield fluorescence microscope. Images were captured with a Hamamatsu Flash 4.0 V2+ sCMOS camera with a 10X/0.30 Ph1 UPlanFL objective. Fluorescence of mCHR was imaged with a 555/25 nm excitation and a 605/52 nm emission filter, with 400 ms exposure. Fluorescence of eGFP was imaged with a 490/20 nm excitation and a 525/36 nm emission filter, with 200 ms exposure. Z-stack images were constructed by scanning vertically in 10 µm increments. The Imaris imaging software package was used to identify mCHR expressing cells in the Z-stack images using the following settings: XY diameter 20 µm, Z diameter 40 µm, background subtraction, quality above 10.5, region growing type was set to local contrast. Outlines of the mCHR cells were applied to the eGFP Z-stack images, and the center intensity values of the outlines were extracted from the eGFP images.

3.2.5 Statistical analysis

Datasets were analyzed with GraphPad Prism® v.7.01: Welch's t-tests were used to compare datasets, and Pearson correlation coefficients were used to define correlations. A p value of < 0.05 was considered significant.

3.3 Results and Discussion

3.3.1 BLOCCs are an inexpensive and simple-to-fabricate cell culture platform

Block-**l**ayered **o**xygen-**c**ontrolling **c**hips (BLOCCs) are able to support both 2D and 3D cultures in defined oxygen gradients. The chips are composed of an alternating series of acrylic

and silicone components. Each component is laser cut separately to incorporate a pattern of interest and then stacked to form a complex chip architecture. This stackable format makes the design modular and able to support a number of configurations. The acrylic components provide structural rigidity to the chip, and their optical transparency enables real-time fluorescence imaging of cells within the chip. Acrylic is also biocompatible and impermeable to oxygen,[40] preventing oxygenated medium from affecting the generation of oxygen gradients along the cell culture region. The silicone components are highly compressible and act as gaskets, which provide water-tight seals between the acrylic layers without the need for solvent bonding the acrylic components. The silicone is also highly permeable to oxygen, and enables the formation oxygen gradients along the cell culture region by flowing gasses with varying oxygen tensions through parallel channels. Once the components are assembled, the BLOCC devices are compressed using screws. The robust materials used to construct BLOCCs and ease of (dis)assembly allow these chips to be reused.

The particular BLOCC design we used in this study has seven layers (A through G, **Fig. 3.1**). The top (A) and bottom (G) acrylic pieces enclosed the entire device, isolating the cell culture from external conditions. Layers B–D acted as a culture medium reservoir, holding a total volume of 1 mL. Layer E connected the culture medium to the five 1.5 x 1.5 x 0.8 mm cell culture-containing regions in layer F. Layer F also contained two gas flow channels, which flanked the cell-containing regions. We found that the hydrogel readily wicked along the walls of the silicone gasket, generating a concave structure that sequestered cells along the perimeter of the cell-seeded regions. To ensure cells were uniformly spread throughout the cell-seeded regions and evenly distributed along the oxygen gradients formed in the BLOCC, we added cell-free hydrogel before adding the cell-laden hydrogel. Once stacked, Layers A–F form integrated

inlet and outlet ports, through which we introduced different gas mixtures into the parallel channels in layer F.

BLOCCs are attractive for both prototyping and manufacturing due to their simplicity in design. Fabrication of this device and others is straightforward and requires two essential tools: i) a vector drawing program (e.g., Abode Illustrator, Coral Draw, or Vectr), and ii) a laser cutter. The vector drawing program allows users to readily convert two-dimensional images in a unique vector-file format, which can then be read as a series of x- and y-coordinates by the laser cutter. Laboratories with minimal resources to invest in these tools can find free-ware vector drawing programs online and tabletop laser cutters for less than $500. The materials needed to fabricate these chips are also low cost—a single BLOCC described in this work costs about $1.70 in raw materials to fabricate.

3.3.2 BLOCCs are compatible with prolonged cell culture

Before using the BLOCCs for cell culture, we tested the biocompatibility of the laser cut silicone and acrylic components. In this assay, parental M231 cells were suspended in Matrigel (2000 cells/ μL) and seeded into a 96-well plate. After a 24 h incubation in culture medium, 30 mg sections of the acrylic or silicone were added to the wells. After a 48 h incubation period, the cells in each well were stained with fluorescein diacetate (5 mg/mL, FDA) and propidium iodide (2 mg/mL, PI). The FDA stain allowed us to identify viable cells and the PI stain identified the dead cells. Cells that stained for both fluorescein and PI were considered dead. The percentage of viable cells in the acrylic- and silicone-containing wells was normalized to control wells. No significant differences in cellular viability were observed (**Fig 3.2**) in any of the wells,

confirming the silicone and acrylic components were suitable for culturing mammalian cells for up to 48 h.

3.3.3 Oxygen gradients are reproducible, tunable, and persistent across 3D cell cultures

Oxygen gradients were generated in the BLOCCs by flowing oxygenated and deoxygenated gasses through two parallel channels in layer F (**Fig 3.1a**). By coating the bottom acrylic component (Layer G) of the BLOCC with an oxygen-sensing film, we were able to map oxygen gradient formation *in situ* across the cell culture-containing regions in layer F (**Fig. 3.3a**). The oxygen-sensing films used in this study were composed of a thin layer of polystyrene impregnated with PdTFPP. These films are ideal for mapping gradients in cell cultures as they are biocompatible and are highly sensitive between 0 – 5% O_2, the range of oxygen tensions found in physiological tissues. We have used these films previously to map oxygen gradients in paper-based cultures.[41,42] Micrographs collected on an inverted fluorescence microscope were used to map the oxygen gradients formed across the chip. The film's luminescence intensity was converted to oxygen tension with an experimentally determined Stern-Volmer relationship. For these analyses, oxygen gradients are always orientated perpendicular to the parallel flow channels.

To generate oxygen gradients of different steepness across the cell culture-containing regions of the BLOCC, two different oxygenated gas mixtures were used in this study: a high-oxygen mixture with 20% O_2, and a low-oxygen mixture with 5% O_2. Each of these gasses, when flowed in parallel with a deoxygenated gas mixture, was able to reach equilibrium within 1 h (**Fig. B3.1**). The high-oxygen mixture had a slope of -8.87 ± 0.03% O_2/mm and an oxygen range extending from 17.4% to 4.2% O_2. The low-oxygen gas had a slope of -2.45 ± 0.02%

O_2/mm and an oxygen range of 4.6% to 0.9% O_2 (**Fig. 3.3c**). These gradient profile differences show that the oxygen gradients across the cell culture-containing region of the BLOCCs can be modulated by simply exchanging the gasses flown through the parallel channels. Recent work by the Eddington group also showed that the oxygen profiles can be modulated by adjusting the distance between the parallel flow channels.[22]

To map cellular responses in an oxygen gradient, we chose the low-oxygen mixture. While the high-oxygen gas would allow cells in a single BLOCC to experience a more diverse oxygen environment due to the steeper slope and wider oxygen range, it was unable to reach oxygen tensions below 4%. Cellular hypoxia and subsequent hypoxic signaling have been measured to occur between 2%–0.5% O_2,[13,43] which makes the low-oxygen gas better suited for evaluating cellular responses to hypoxia.

To ensure oxygen gradients persisted in the presence of cells, BLOCCs were assembled with an oxygen-sensing acrylic component and 2,000 parental M231 cells per seeding region. Oxygen gradients were imposed across the seeding region using the low-oxygen mixture, and were measured over a 12 h period. The resulting oxygen gradients were not only stable throughout the duration of the experiment, but their steepness and dynamic range also did not significantly differ from those formed in the absence of cells (**Fig. 3.3d**). These results confirm that oxygen gradients were unaffected by the presence of cells.

3.3.4 Oxygen gradients in BLOCCs can be correlated to HIF activation in MDA-MB-231 cells

With the oxygen-sensitive films, we were able to map oxygen gradients along a single plane at the bottom of the cell-seeded region. To ensure cells throughout the 3D culture were experiencing oxygen gradients, we loaded hypoxia-responsive M231-HRE cells into the seeding

region. The M231-HRE cells were engineered to express two fluorescent proteins: mCHR and eGFP. The mCHR protein is expressed constitutively and served as a marker to identify cell location within the seeded regions. The gene coding for eGFP is downstream from five hypoxia-response element (HRE) promoter sequences and is only expressed under hypoxic conditions. The two fluorescent proteins enabled cellular location and relative hypoxia to be assessed with fluorescence microscopy.

BLOCCs seeded with M231-HRE cells were incubated for 24 h in the presence of an oxygen gradient or at ambient oxygen conditions. Afterwards, confocal microscopy was used to construct z-stack representations of mCHR and eGFP expression. To identify cell location within the z-stack images, we used the Imaris software package to extract the center intensity mCHR and eGFP values. We chose to use center intensity values because the optical point spread along the z-axis required us to overestimate cell volume when identifying cell location. This overestimation led to the formation of cell boundaries that incorporated non-uniform amounts of background signal and made averaged intensities inconsistent.

The center intensity values of eGFP and mCHR were correlated to their x-axis placement in BLOCCs (**Fig. 3.4**). Of these data, only BLOCCs cultured in the presence of an oxygen gradient showed a significant correlation between eGFP intensity and position in the cell seeded region. M231-HRE cells incubated in BLOCCs cultured at ambient oxygen tensions did not show a significant correlation. Additionally, no correlation was observed for mCHR intensity and cell location for BLOCCs cultured with or without oxygen gradients. The lack of correlation for mCHR expression suggests that oxygen gradients did not affect global protein expression, and that differences in eGFP expression seen within BLOCCs was due to differences in intracellular hypoxia.

To better visualize the relationship between eGFP expression and local oxygen tensions, cell populations across the seeded regions were pooled into four stratified populations (**Fig. 3.4**): stratum 1 corresponds to cells located between 0-0.375 mm, with an oxygen tension range of 4.5-3.6% O_2; stratum 2 corresponds to cells between 0.376-0.750 mm, with an oxygen tension range of 3.6-2.7% O_2; stratum 3 corresponds to cells between 0.751-1.125 mm, with an oxygen tension range of 2.7-1.8% O_2, and; stratum 4 corresponds to cells between 1.126-1.5 mm, with an oxygen tension range of 1.8-1.0% O_2. From these data, there is a clear relationship between low oxygen tension and increased eGFP expression, with strata 4 experiencing oxygen tensions between 2%-1% O_2 and exhibiting significantly higher eGFP expression than the other three strata (**Fig. 3.5a**). There are statistically significant differences in eGFP intensity for strata 4 – 2, highlighting that hypoxic response is proportional for certain ranges of oxygen tension. The eGFP intensities of strata 2 and 1 are not significantly different.

When comparing eGFP expression between M231-HRE cells cultured in the absence of an oxygen gradient, cell populations along the border have a significantly higher ($p < 0.05$) eGFP intensity relative to those along the interior (**Fig. 3.5b**). It is unclear what causes this trend; however, eGFP expression for cells cultured in the presence of an oxygen gradient was significantly higher than cells cultured at ambient oxygen tensions (**Fig. B3.2**). These results are unsurprising, as cells cultures at ambient oxygen tensions have greatly attenuated HIF-1α expression relative to cultures experiencing less than 4% O_2.[13]The difference in eGFP expression in the gradient-present cultures validate that cells distributed vertically throughout the BLOCC are experiencing the imposed oxygen gradient, and that BLOCCs can be used to correlate spatial differences between hypoxic signaling and regional oxygen tensions.

3.4 Conclusions

In this work, we fabricated and characterized a modular fluidic chip platform capable of generating oxygen gradients across 3D cell cultures. The device consists of alternating layers of acrylic and silicone components, which can be compressed together with screws. The components are simple to design and fabricate, and allow for cultures to be readily assembled and disassembled for reuse of the device. Stable oxygen gradients are readily generated across the 3D cell cultures within the device and can be modulated by simply exchanging gasses. By incorporating hypoxia-responsive cells into this device, we were able to spatially correlate hypoxic signaling with oxygen tension. The accessibility and simplicity-in-design makes this device a promising resource for laboratories that lack microfluidic chip fabrication expertise or facilities but wish to develop cultures capable of relating cell phenotype to oxygen gradients.

3.5 Figures

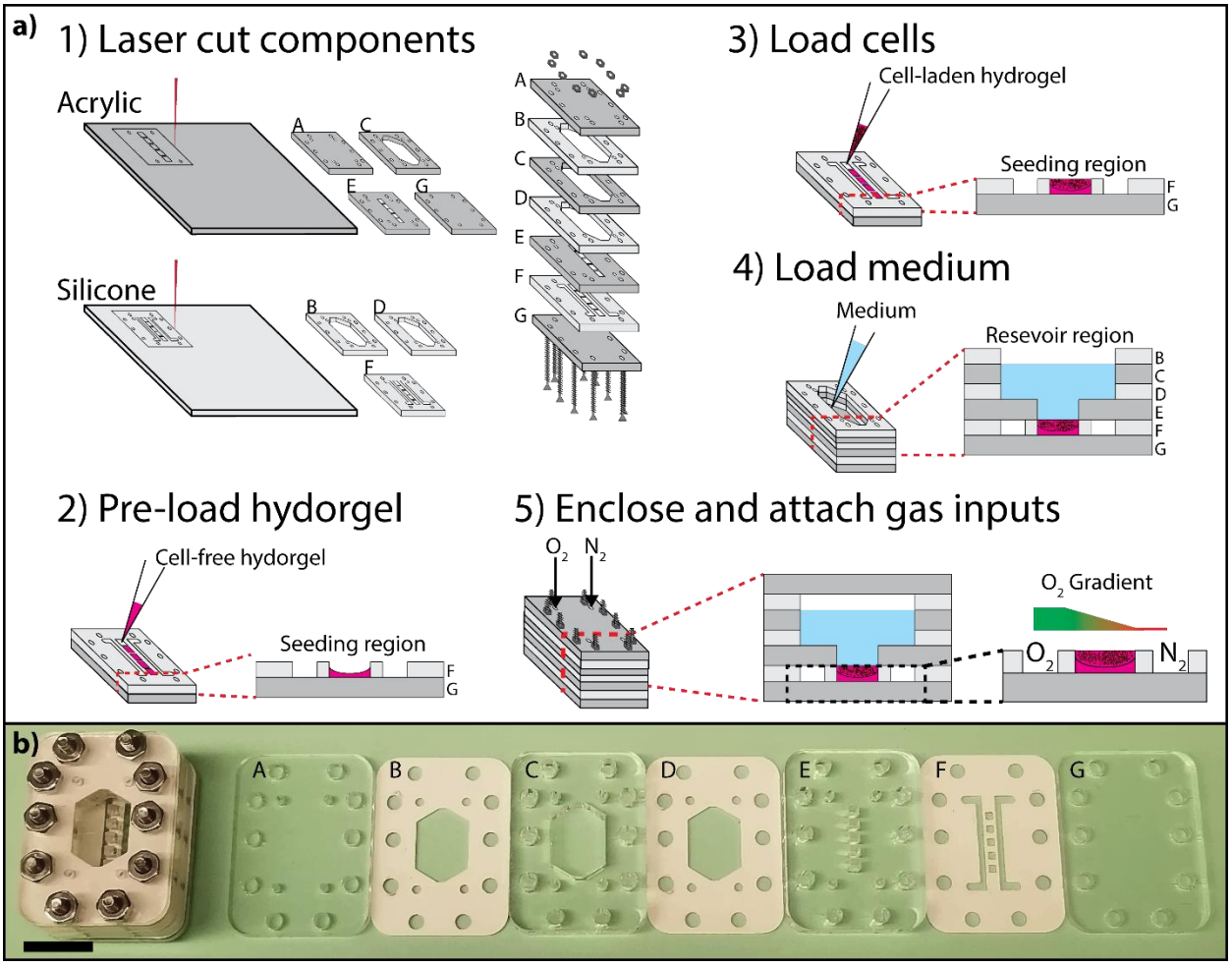

Figure 3.1 Schematic depicting the fabrication and assembly of a BLOCC. a) 1) Individual components are first cut out of the acrylic and silicone sheets using a laser cutter. 2) Components F and G are compressed together by hand and loaded with a cell-free hydrogel. 3) After the cell-free hydorgel has gelated, a cell-laden hydrogel is added to the cell seeding regions. 4) Components B-G are stacked and compressed together by hand, and 1 mL of culture medium is added to the resevoir. 5) Component A is added to the top and the entire chip is closed using nuts and screws. Oxygenated and deoxygenated gasses are applied to the inlets and an oxgen gradient is formed along the 3D cell culture. Note: the schematics are not drawn to scale. b) Each acrylic and silicone component used to construct a BLOCC is ordered from left to right (A-G) with the assembled chip on the far left. (Scale bar = 15 mm)

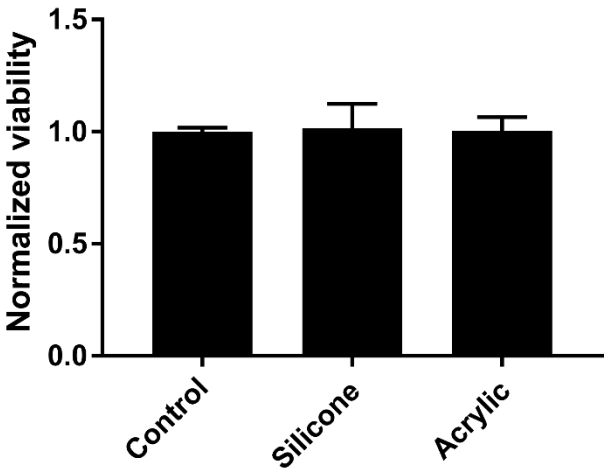

Figure 3.2 The biocompatibility of the silicone and acrylic components used to construct the BLOCCs was measured after a 48 h incubation. Each bar represents the percent of viable parental M231 cells, normalized to the control samples. No statistically significant difference was found for any of the culture conditions. (n = 3, error bars = SD)

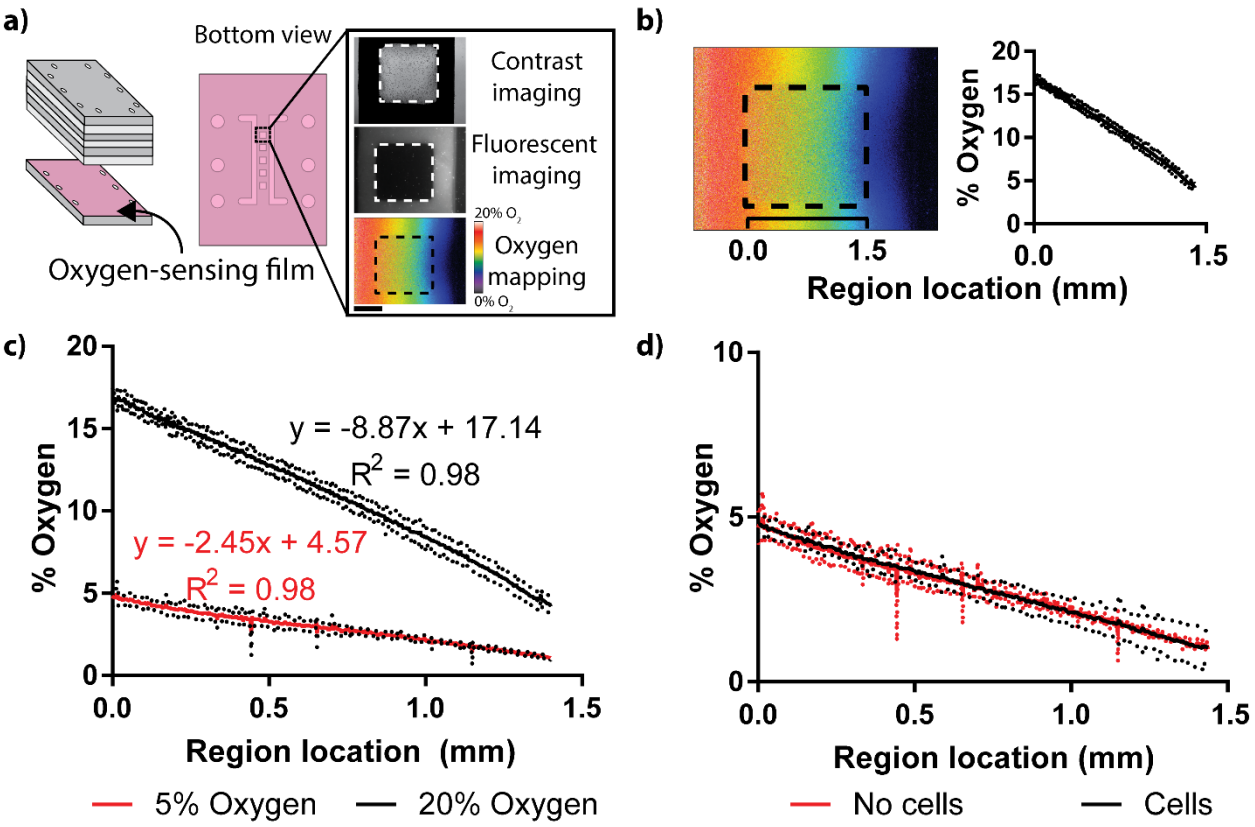

Figure 3.3 Characterization of oxygen gradients within an assembled BLOCC. a) Oxygen gradients were measured with an oxygen-sensing film, which was coated onto the bottom acrylic component of the BLOCC and placed in contact with the cell-containing regions. After the device is closed, phase contrast and fluoresence microscopy was used to visualize cell location and map the oxygen gradient, respectively. The scale bar in the image inset is equal to 0.75 mm. b) The 2D oxygen maps were converted into one-dimensional oxygen gradients along the 1.5 mm wells of the cell seeding region. c) Oxygen gradients were generated using 5% or 20% O_2 gas mixes in parallel with a 0% O_2 gas. (black dots = SD, n = 3) d) Oxygen gradients were generated in the presence and and absence of cells using a 5% oxygen mix, and no significant difference was seen between profiles. (black/red dots = SD, n = 3)

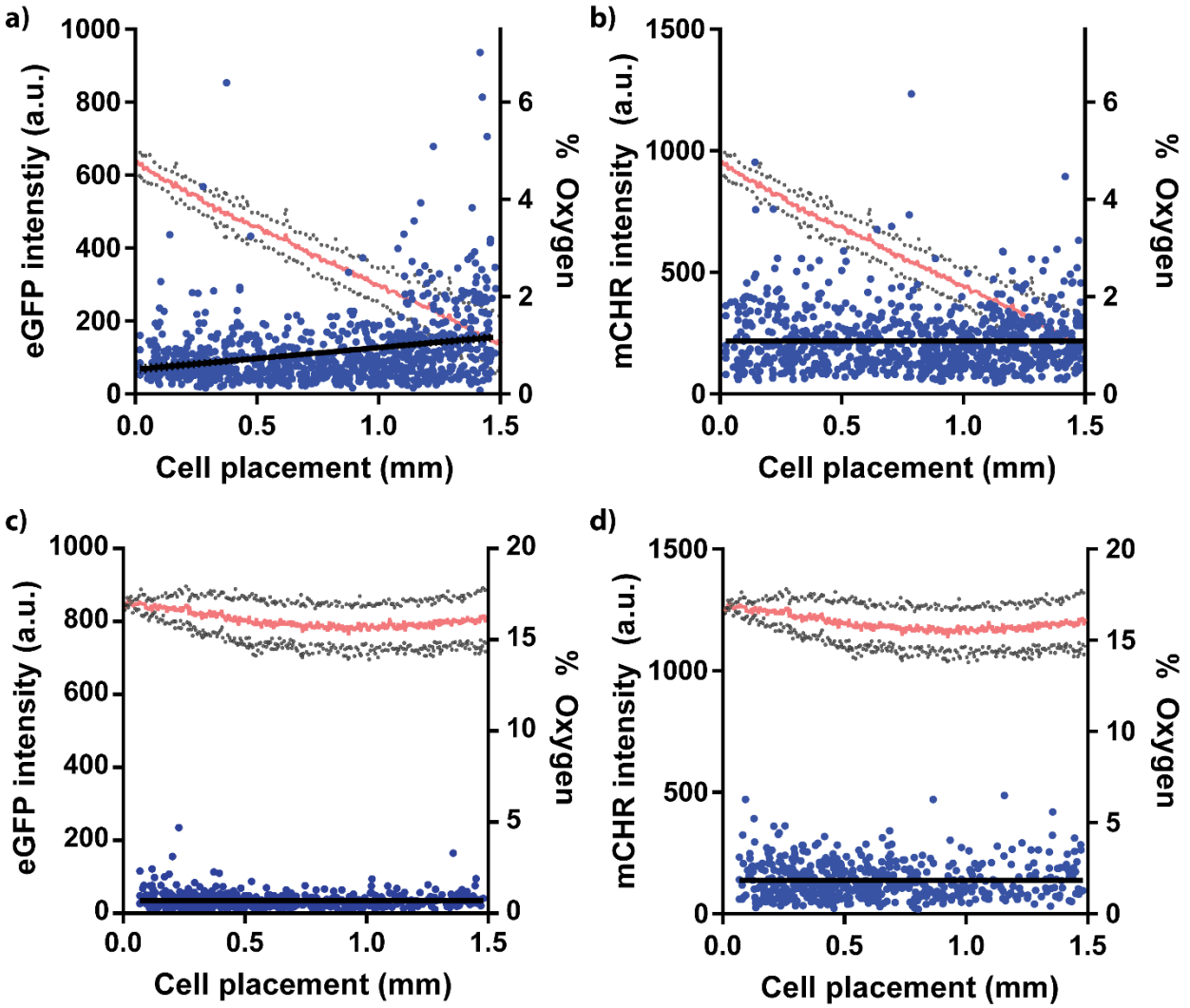

Figure 3.4. The eGFP and mCHR fluorescence intensities of single cells correlated to their spatial location for cultures under an oxygen gradient or ambient oxygen conditions. The (a) eGFP and (b) mCHR intensities of M231-HRE cells incubated under a 5% oxygen gradient. The eGFP cells exhibited a significant correlation relative to x-axis placement under the oxygen gradient (Pearson's r = 0.263, P < 0.0001); however, the mCHR cells did not exhibit a significant relationship. The (c) eGFP and (d) mCHR intensity of M231-HRE cells cultured under ambient oxygen conditions did not exhibit a significant correlation with spatial placement. (red line = average % oxygen, black dots = SD % oxygen, n = 3)

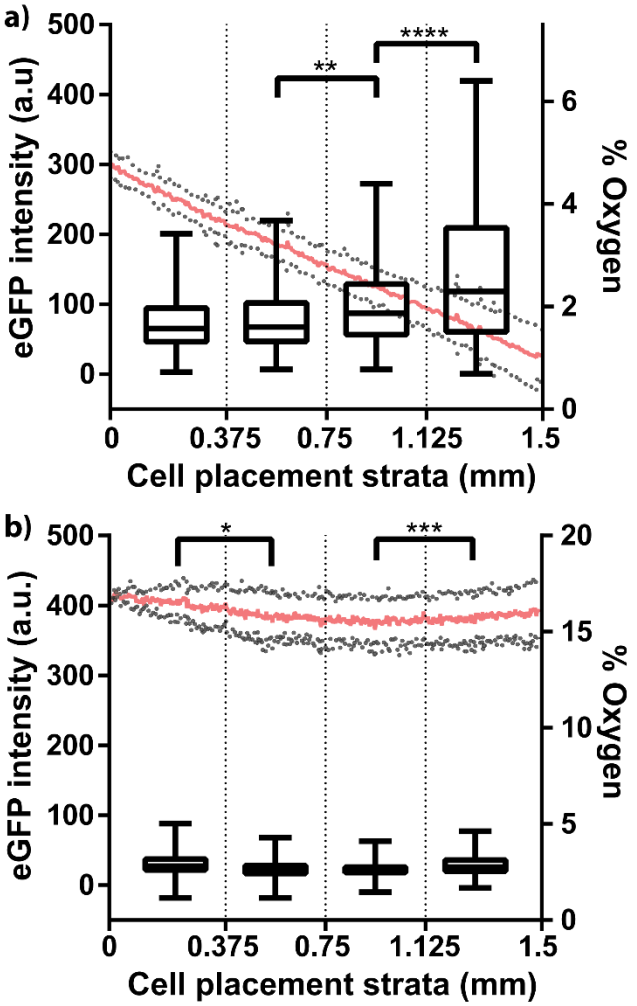

Figure 3.5 Correlating hypoxia-responsive signaling in M231-HRE cells to spatial placement along an oxygen gradient. M231-HRE cells were incubated in BLOCC assemblies with (a) an oxygen gradient or (b) under ambient oxygen conditions. The seeding region was stratafied into four consecutive regions with equal lengths, and the eGFP intensities were pooled within each region ($n \geq 95$). The eGFP intensities are represented by arbitrary units (a.u.), and the overlain oxygen gradients (red line = average % oxygen, black dots = SD) depict the oxygen tension range experienced within each stratified region. (* = $P < 0.05$, ** = $P < 0.01$, *** = $P < 0.001$, **** = $P < 0.0001$)

REFERENCES

(1) Fong, G. H. *Angiogenesis* **2008**, *11* (2), 121–140.

(2) Semenza, G. L. *Trends Mol. Med.* **2001**, *7* (8), 345–350.

(3) Semenza, G. L. *Annu. Rev. Pathol. Mech. Dis.* **2014**, *9* (1), 47–71.

(4) Semenza, G. L. *Physiology* **2009**, *24*, 97–106.

(5) Fukuda, R.; Zhang, H.; Kim, J. whan; Shimoda, L.; Dang, C. V.; Semenza, G. L. L. *Cell* **2007**, *129* (1), 111–122.

(6) Pugh, C. W.; Ratcliffe, P. J. *Nat. Med.* **2003**, *9* (6), 677–684.

(7) Bristow, R. G.; Hill, R. P. *Nat. Rev. Cancer* **2008**, *8* (3), 180–192.

(8) Semenza, G. L. *Trends Pharmacol Sci.* **2013**, *33* (4), 207–214.

(9) Semenza, G. L. *Annu. Rev. Pathol.* **2014**, *9* (1), 47–71.

(10) Rohwer, N.; Cramer, T. *Drug Resist. Updat.* **2011**, *14* (3), 191–201.

(11) Sullivan, R.; Graham, C. H. *Cancer Metastasis Rev.* **2007**, *26* (2), 319–331.

(12) Lunt, S. J.; Chaudary, N.; Hill, R. P. *Clin. Exp. Metastasis* **2008**, *26* (1), 19–34.

(13) Jiang, B. H.; Semenza, G. L.; Bauer, C.; Marti, H. H. *Am. J. Physiol.* **1996**, *271* (45), C1172–C1180.

(14) Lin, C.; McGough, R.; Aswad, B.; Block, J.; Terek, R. *J. Orthop. Res.* **2004**, *22*, 1175–1181.

(15) Kim, J. W.; Tchernyshyov, I.; Semenza, G. L.; Dang, C. V. *Cell Metab.* **2006**, *3* (3), 177–185.

(16) Minchenko, A.; Leshchinsky, I.; Opentanova, I.; Sang, N.; Srinivas, V.; Armstead, V.; Caro, J. *J. Biol. Chem.* **2002**, *277* (8), 6183–6187.

(17) Bracken, C. P.; Fedele, A. O.; Linke, S.; Balrak, W.; Lisy, K.; Whitelaw, M. L.; Peet, D. J. *J. Biol. Chem.* **2006**, *281* (32), 22575–22585.

(18) Brennan, M. D.; Rexius-Hall, M. L.; Elgass, L. J.; Eddington, D. T. *Lab Chip* **2014**, *14* (22), 4305–4318.

(19) Wang, L.; Liu, W.; Wang, Y.; Wang, J.; Tu, Q.; Liu, R.; Wang, J. *Lab Chip* **2013**, *13* (4),

695–705.

(20) Chang, C.-W.; Cheng, Y.-J.; Tu, M.; Chen, Y.-H.; Peng, C.-C.; Liao, W.-H.; Tung, Y.-C. *Lab Chip* **2014**, *14* (19), 3762–3772.

(21) Acosta, M. a; Jiang, X.; Huang, P.-K.; Cutler, K. B.; Grant, C. S.; Walker, G. M.; Gamcsik, M. P. *Biomicrofluidics* **2014**, *8* (5), 54117.

(22) Rexius-Hall, M. L.; Rehman, J.; Eddington, D. T. *Integr. Biol.* **2017**, *9*, 742–750.

(23) Uchida, H.; Sato, A.; Miyayama, A.; Tsukada, K. *Adv. Biomed. Eng.* **2013**, *2*, 143–149.

(24) Byrne, M. B.; Leslie, M. T.; Patel, H. S.; Gaskins, H. R.; Kenis, P. J. A. *Biomicrofluidics* **2017**, *11* (5).

(25) Lo, J. F.; Sinkala, E.; Eddington, D. T. *Lab Chip* **2010**, *10* (18), 2394–2401.

(26) Sackmann, E. K.; Fulton, A. L.; Beebe, D. J. *Nature* **2014**, *507* (7491), 181–189.

(27) Skolimowski, M.; Nielsen, M. W.; Emnéus, J.; Molin, S.; Taboryski, R.; Sternberg, C.; Dufva, M.; Geschke, O. *Lab Chip* **2010**, *10* (16), 2162.

(28) Hakkinen, K. M.; Harunaga, J. S.; Doyle, A. D.; Yamada, K. M. *Tissue Eng. Part A* **2011**, *17* (5–6), 713–724.

(29) Kenny, P. A.; Lee, G. Y.; Myers, C. A.; Neve, R. M.; Semeiks, J. R.; Spellman, P. T.; Lorenz, K.; Lee, E. H.; Barcellos-Hoff, M. H.; Petersen, O. W.; Gray, J. W.; Bissell, M. J. *Mol. Oncol.* **2007**, *1* (1), 84–96.

(30) Luca, A. C.; Mersch, S.; Deenen, R.; Schmidt, S.; Messner, I.; Schäfer, K. L.; Baldus, S. E.; Huckenbeck, W.; Piekorz, R. P.; Knoefel, W. T.; Krieg, A.; Stoecklein, N. H. *PLoS One* **2013**, *8* (3), 1–11.

(31) Gross, B.; Lockwood, S. Y.; Spence, D. M. *Anal. Chem.* **2017**, *89*, 57–70.

(32) Truong, A. S.; Lockett, M. R. *Analyst* **2016**, 3874–3882.

(33) Truong, A. S.; Lochbaum, C. A.; Boyce, M. W.; Lockett, M. R. *Anal. Chem.* **2015**, *87* (22), 11263–11270.

(34) Vordermark, D.; Shibata, T.; Brown, J. M. *Neoplasia* **2001**, *3* (6), 527–534.

(35) Capretto, L.; Mazzitelli, S.; Focaroli, S.; Nastruzzi, C.; Sciences, E. Chips & Tips : Wall plug inspired connectors for macro to microfluidic interfacing http://blogs.rsc.org/chipsandtips/2010/07/23/wall-plug-inspired-connectors-for-macro-to-microfluidic-interfacing/.

(36) Boyce, M. W.; Kenney, R. M.; Truong, A. S.; Lockett, M. R. *Anal. Bioanal. Chem.* **2015**, 1–8.

(37) Schneider, C. a; Rasband, W. S.; Eliceiri, K. W. *Nat. Methods* **2012**, *9* (7), 671–675
.

(38) Schindelin, J.; Arganda-Carreras, I.; Frise, E.; Kaynig, V.; Longair, M.; Pietzsch, T.; Preibisch, S.; Rueden, C.; Saalfeld, S.; Schmid, B.; Tinevez, J. Y.; White, D. J.; Hartenstein, V.; Eliceiri, K.; Tomancak, P.; Cardona, A. *Nat. Methods* **2012**, *9* (7), 676–682.

(39) Arganda-Carreras, I.; Kaynig, V.; Rueden, C.; Eliceiri, K. W.; Schindelin, J.; Cardona, A.; Seung, H. S. *Bioinformatics* **2017**, *33* (15), 2424–2426.

(40) Sin, A.; Chin, K. C.; Jamil, M. F.; Kostov, Y.; Rao, G.; Shuler, M. L. *Biotechnol Prog* **2004**, *20* (1), 338–345.

(41) Boyce, M. W.; Kenney, R. M.; Truong, A. S.; Lockett, M. R. *Anal. Bioanal. Chem.* **2016**, *408* (11), 2985–2992.

(42) Boyce, M. W.; LaBonia, G. J.; Hummon, A. B.; Lockett, M. R. *Analyst* **2017**, *142* (15), 2819–2827.

(43) McKeown, S. R. *Br. J. Radiol.* **2014**, *87* (1035), 1–12.

CHAPTER 4: ASSESSING CHEMOTHERAPEUTIC EFFECTIVENESS USING A PAPER-BASED TUMOR MODEL

4.1 Introduction

Cell-based screens used to identify potential chemotherapeutics rely heavily on two-dimensional (2D) assays in which cells are cultured as monolayers. These assays are easily assembled and amenable to screening libraries of potential therapeutics in a high-throughput and parallel manner. Despite their utility, monolayer cultures fail to replicate the complex chemical and physiological conditions that promote *in vivo* drug-resistance.[1–4] This disparity between 2D cultures and *in vivo* conditions is, in part, attributed to why a majority of therapeutic candidates fail in pre-clinical trials.[2] To better identify potential therapeutic candidates during the drug discovery phase, more predictive *in vitro* assays are needed.

A growing body of research suggests that three-dimensional (3D) cultures can be used to bridge the biological gap between monolayer cultures and animal models.[2,4–6] Cells cultured in 3D environments as aggregates (i.e., spheroids) or in hydrogel scaffolds develop distinct morphologies,[5] behaviors,[6] and chemosensitivities[4] that are more representative of cells found *in vivo*. Spheroids have been widely used to assess therapeutic efficacy and toxicity,[2,7–11] as mass-transport limitations within spheroids produce chemical gradients similar to those within poorly vascularized tumor tissue.[12,13] These chemical gradients lead to the formation of stratified zones of cells: proliferating cells along the exterior of the spheroid, quiescent cells in the spheroid's interior, and necrotic cells at the spheroid's core.[12–16] Each of these zones exhibit varying degrees of sensitivity to therapeutic dosing, and yield physiochemical conditions that

allow spheroids to better predict *in vivo* responses.[2,4,17–19] Despite their benefits, spheroids face a number of limitations: i) only a small subset of cell lines are capable of forming aggregates;[7] ii) deriving spatial information requires laborious histological sectioning; and iii) spheroids offer limited experimental control over the chemical gradients which form across the culture.

Paper-based cultures (PBCs) are an emerging 3D culture platform that overcomes many of the limitations associated with spheroids. PBCs are compatible with a wide range of cell types, because they are prepared by suspending cells in a hydrogel, which is then infused into sheets of wax-patterned filter paper. The paper fibers provide structural integrity to the hydrogel slabs, allowing the individual sheets to be stacked together in a modular fashion. Wax patterns on the paper act as hydrophobic barriers and provide discrete zones for seeding cells. By introducing impermeable barriers, diffusional exchange is limited to one side of the stacked culture, resulting in the formation of monotonic gradients similar to the chemical gradients found in poorly vascularized tumors.[20] The modularity of the PBCs also provide control over the chemical environment formed in the stacked cultures, as cell density, thickness, and orientation can be changed to suit experimental needs.

The ability to separate the stacks into individual layers after an experiment provides spatially resolved datasets relating cellular responses to the chemical environment experienced during incubation. Cell-containing sheets have been analyzed with a number of different readouts, including: quantitative polymerase chain reaction (qPCR), fluorescence microscopy, immunohistochemistry (IHC), enzyme-linked immunosorbent assay (ELISA), and mass spectrometry.[21–24] Due to the similarities between chemical environments in PBCs and avascular tissue, this platform has been used to investigate the invasion of breast and lung carcinomas,[21,23,25,26] cardiac ischemia,[27] and cancer metabolism.[24,28,29]

In this study, we used PBCs to relate differences in the chemoresistance of a colorectal carcinoma cell line to the oxygen environment experienced by those cells. The PBCs are described in **Fig. 4.1**, and were used to impose monotonic gradients of nutrients and wastes vertically along the stacked cultures. By adjusting the cell density of these cultures, we showed that we could manipulate the profile of the chemical gradients that form and tune the chemical environment. We confirmed our ability to modulate these gradients by quantifying oxygen profiles in cultures seeded at a high and low density: 84,000 cells/zone and 21,000 cells/zone, respectively. As expected, cultures seeded at lower densities experienced shallower oxygen gradients. By dosing these cultures with a chemotherapeutic agent, SN-38, we compared cellular viability between each scaffold. This information allowed us to relate spatial differences in relative chemoresistance to the layer's local oxygen environment. Our findings show that high-density cultures experiencing chronic hypoxia exhibit increased sensitivity to therapeutic dosing, while low density cultures have increased resistance. Through this work, we expand on the application of PBCs by demonstrating the ability of this platform to assess chemotherapeutic efficacy in a colon tumor model with varying chemical environments.

4. 2 Experimental

4.2.1 Cell culture

HCT116 colorectal carcinoma cell lines were obtained from the American Type Culture Collection (ATCC), and validated by Short Tandem Repeating (STR) sequencing in 2016. The cells were maintained as adherent cultures at 5 % CO_2 and 37 °C in McCoy's 5A medium with L-glutamine, supplemented with fetal bovine serum (10%, v/v) and penicillin-streptomycin (1%, v/v). Medium was exchanged approximately every 48 h, and cells were passaged at 70-80%

confluency. Cells were passaged by detachment with trypsin-EDTA (5 min, 37 °C). Cells were washed with serum-containing medium, pelleted, resuspended, and cultured in a fresh flask at a 1/10 dilution. All cell culture reagents, unless otherwise stated, were acquired from Gibco by Life Technologies.

Lines of HCT116 cells constitutively expressing mCherry fluorescent protein (HCT116 mCHR) were generated via transfection with a 3:1 ratio (g/L) of mCherry2-C1 plasmid to EndoFectin™ Max (GeneCopoeia). The mCherry2-C1 plasmid was a gift from Michael Davidson (Addgene, plasmid # 54563). The transfection was performed according to the manufacturer's suggested protocol. Stable lines were maintained with 500 μg/mL of Geneticin® (ThermoFisher) until a single clone was selected.

4.2.2 Paper scaffold and PET film preparation

Paper-based scaffolds were prepared as detailed previously.[21,30] Sheets of Whatman 105 lens paper were wax-patterned with a ColorQube 8570 printer (Xerox) and sterilized with ultra-violet (UV) light overnight prior to usage. Two paper designs were used in this study: i) a "9-zone scaffold," which contained nine circular zones (2.5 μm diameter) for seeding with cell-free or cell-laden Matrigel, and ii) a "single-zone scaffold", which contained one circular zone (2.5 mm diameter) for seeding. Schematics of the 9-zone scaffolds can be found in the Electronic Supplementary Information (ESI) of reference #21. Schematics of the single-zone scaffolds are provided in Appendix 3, **Fig. C4.1**.

Polyethylene terephthalate (PET) films (overhead transparency, Staples®) were prepared as detailed previously.[21,30] Two PET designs were used for this study: i) an "open" design, which

contained nine openings matching the locations of the zones in the 9-zone scaffold; and ii) a "closed" design, which prevented the exchange with medium by containing no openings.[30]

4.2.3 Assembling PBCs

Prior to seeding the 9-zone scaffold with HCT116 mCHR cells, the cells were suspended in Matrigel (Corning) at a density of either 168,000 cells/µL or 42,000 cells/µL. Once prepared, the Matrigel suspensions were stored on ice to prevent gelation. In the cell-containing paper scaffolds, five zones were seeded with 0.5 µL of the cell-laden Matrigel. The remaining four zones were filled with 0.5 µL of cell-free Matrigel and served as background controls for image analysis. In the cell-free scaffolds, all nine zones were filled with 0.5 µL of cell-free Matrigel. After seeding, the scaffolds were incubated in medium for 4 h before assembling the stack culture.

The stacked PBCs used in this study are detailed in **Fig. 4.1**. Each stack consisted of: i) an open PET film (top), ii) a 13-mm diameter, 0.4 µm pore size track-etched membrane (Whatman), iii) a cell-free paper scaffold, iv) 11 cell-laden paper scaffolds, and v) a closed PET film (bottom). The entire stack was placed between stainless steel holders, which ensured the individual scaffolds were in conformal contact throughout the experiment. Stacked cultures used for oxygen measurements contained either 1, 4, 8, or 12 paper scaffolds. In assemblies with 4, 8, and 12 scaffolds, the first scaffold was cell-fee with the remaining scaffolds containing either 84,000 cells/zone or 21,000 cells/zone.

Assembled cultures were placed in 6-well plates containing McCoy's 5A medium and incubated on an orbital shaker set to 300 rpm. Medium in each well was exchanged every three

days. Prior to fluorescence imaging or staining, the stacks were disassembled and each scaffold washed twice with phosphate buffer saline (PBS).

4.2.4 Immunocytochemistry

Within 15 min of disassembling a PBC, the individual scaffolds were fixed in PBS with 4% (v/v) paraformaldehyde for 15 min. Scaffolds were then blocked and permeabilized for 1 h in PBS containing 5% normal goat serum (Cell Signaling Technologies) and 0.3% Triton™ X-100 (Sigma-Aldrich) prior to immunostaining. Scaffolds were incubated in the primary antibody solution overnight at 4 ºC, and then incubated in the secondary antibody solution for 4 h at room temperature. Antibodies were diluted with PBS containing 1% (w/v) bovine serum albumin (Cell Signaling Technologies) and 0.3% Triton™ X-100: rabbit anit-Ki-67 (primary antibody, H-300, Santa Cruz, 1:100 dilution) and goat anti-rabbit IgG-CFL488 (secondary antibody, sc-516248, Santa Cruz, 1:500 dilution).

4.2.5 Oxygen sensor integration and interrogation

The oxygen sensors consisted of a palladium tetrakis (pentafluorophenyl) porphyrin (PdTFPP)-containing polystyrene thin film coated onto a PET sheet. The fabrication and characterization of these sensors are detailed in previous work.[20] Briefly, a 1 mM solution of PdTFPP in 18.75% (w/w) polystyrene-toluene was spin-coated onto a 13-mm circular PET sheet. Prior to incorporation into PBCs, the sensors were sterilized with UV light for 1 h.

The oxygen sensors were placed at the bottom of stacks containing 1-, 4-, 8-, or 12-scaffolds in lieu of the closed PET films, and the cultures were maintained at normal cell culture

conditions in 6-well plates. Oxygen measurements were collected at 24, 72, 96, 120, and 168 h after initial assembly. Medium was exchanged every three days.

4.2.6 SN-38 dose-response assay

A 5 mM stock solution of SN-38 (Cayman Chemical) was prepared in DMSO (Sigma-Aldrich). A range of SN-38 concentrations were prepared at 2x the working concentration (0, 0.001, 0.002, 0.01, 0.02, 0.1, 1, 10 µM) by dissolving the SN-38 stock solution into McCoy's 5A medium. Each SN-38 solution contained 0.2% (v/v) DMSO.

3D cultures were prepared by pipetting 0.5 µL of cell-laden Matrigel (20,000 cells/µL) into single-zone scaffolds (**Fig. C4.1**). Additional scaffolds were prepared with 0.5 µL of cell-free Matrigel to serve as background controls. The single-zone scaffolds were placed into individual wells of a 96-well plate containing 100 µL of McCoy's 5A medium and incubated for 24 h prior to dosing. Scaffolds were dosed with SN-38 by adding 100 µL of the respective concentrations to each well. After dosing for 48 h, scaffolds were transferred to wells containing 100 µL of culture medium.

2D cultures were prepared by adding 5,000 cells in 100 µL of medium to wells of a 96-well plate. Cultures were incubated for 24 h, then dosed with 100 µL of the respective SN-38 concentrations for 48 h. After dosing, 100 µL of medium was removed from each well.

Cellular viability was assessed with CellTiter-Glo™ (CTG, Promega). For the 3D and 2D cultures, 100 µL of CTG reagent was added to each cell-containing well. The plates were agitated on an orbital shaker at 800 rpm at room temperature for 15 min prior to analysis. Chemiluminescence was measured on a SpectraMax M5 (Molecular Devices) spectrophotometric plate reader with an integration time of 500 ms. Emission intensities from

wells without cells (2D cultures) or wells with cell-free single-zone scaffolds (3D cultures) were used as background. All background-subtracted intensities were averaged and normalized to the vehicle control.

4.2.7 Fluorescein penetration assay

Sodium fluorescein (Fluka) was dissolved in McCoy's 5A medium to prepare a 0.5 mg/mL solution. PBCs containing 12 scaffolds seeded at a cell density of 84,000 cells/zone were placed in a 6-well plate without additional medium and situated on the stage of an incubated inverted microscope (Axiovert 40 CFL, Zeiss). The wells of the top metal holder were filled with 100 µL of the fluorescein solution, and fluorescence images were of the bottom of the stack were recorded every minute for 11 h. Images were taken using an Axiovert 40 CFL (Zeiss) inverted microscope equipped with a LED light source (wLS-LG-MB, QImaging), 470±20 nm excitation filter, 540±40 nm emission filter, and monochrome 12-bit camera (QIC-F-12-C, QImaging).

4.2.8 Image acquisition and analysis

Fluorescence images of the individual scaffolds were acquired with a Typhoon 9400 scanner (GE Life Sciences) at a resolution of 200 µm. HCT116 mCHR cells were imaged using a 532 nm laser and 610±30 nm emission filter. The Ki-67 stained cells were imaged using a 488 nm laser and 526 nm short pass emission filter.

Viability measurements were performed by measuring the average mCHR fluorescence value of each zone using ImageJ software.[31] Reported fluorescence values for a single scaffold were obtained by subtracting the average fluorescence intensity of the four cell-free zones from the average fluorescence intensity of the five cell-containing zones. Relative proliferation was

determined by dividing Ki-67 images by their corresponding mCHR image. Reported values are a ratio of Ki-67 intensity to mCHR intensity.

Fluorescence images of the of the oxygen sensors and fluorescein penetration studies were taken using an Axiovert 40 CFL (Zeiss) inverted microscope equipped with a LED light source (wLS-LG-MB, QImaging) and monochrome 12-bit camera (QIC-F-12-C, QImaging). The oxygen sensors were imaged with a 546±12 nm excitation filter and 590 nm long pass filter. Fluorescein was imaged using a 470±20 nm excitation filter and 540±40 nm emission filter.

4.2.9 Statistical analysis

Unless otherwise stated, all reported values are the average and standard error of the mean (SEM). Datasets were analyzed with GraphPad Prism® v.7.01: a two-way ANOVA with Tukey's multiple comparison post-test was used to compare different data sets. A p value of < 0.05 was considered significant.

4.3 Results and discussion

4.3.1 Constructing a paper-based colon tumor model

In poorly vascularized tumor tissue, mass transport limitations of nutrients and waste products lead to the development of stratified cell populations.[32] Cells closest to the vasculature receive the supply of nutrients needed for proliferation, while cells further from the vasculature receive limited nutrients due to consumption outpacing diffusional delivery. Within these regions of depleted nutrients, cells adopt a quiescent phenotype or become necrotic. Chemotherapeutics that target proliferative cells by interfering with some aspect of the cell-cycle yield varying cellular responses in the stratified populations of a tumor.[33] There is a need for an *in vitro* culture

model that recapitulates the cellular heterogeneity found in tumors, but is as easily setup and analyzed as monolayer cultures. To mimic the diffusion-limited environment that gives way to population stratification in poorly vascularized tumors, we constructed PBCs of HCT116 mCHR cells suspended in Matrigel (**Fig. 4.1**).

We chose HCT116 cells because their response to various chemotherapeutics, including SN-38 used in this study, has been well characterized in both monolayer and spheroid cultures.[9,11,19,34] Engineering the HCT116 cells to constitutively express mCherry allowed us to relate fluorescence intensity to viability, as mCherry fluorescence intensity and cell number are linearly related for HCT116 mCHR cells imaged on a Typhoon scanner (**Fig. C4.2**). We chose Whatman 105 filter paper to fabricate the paper scaffolds because it has a large void volume (~80%) and low fiber density, allowing the scaffolds to readily retain the cell-laden Matrigel while still maintaining compatibility with fluorescence imaging.

The culture system used in this work is summarized in **Fig. 4.1**. Of the 12 paper scaffolds, 11 were seeded with cells to ensure hypoxia was reached in the stack.[35] The cell-free scaffold at the top of the stack provided a layer in which cells could expand into during incubation. A polycarbonate track etch membrane was placed at the top of the paper stack to retain cells in the paper scaffolds, ensuring that each culture was 360 μm thick. The PET films placed at the top and bottom of the culture allowed us to control diffusion of fresh medium into the culture and resulted in the formation of gradients along the stack. Stainless steel holders enclosed the entire culture and held the scaffolds together in conformal contact.

4.3.2 Proximity to a nutrient source affects spatiotemporal distribution of cells

Before evaluating drug resistance in the stacked cultures, we investigated the spatiotemporal evolution of viable HCT116 cells for culture periods of up to one week. Despite the linear trend between fluorescence intensity and number of mCHR-expressing cells under normoxic conditions (**Fig. C4.2**), we report viability in terms of mCHR fluorescence because environmental oxygen tensions can potentially attenuate mCherry expression. Specifically, hypoxic conditions have been shown to elicit a global down-regulation of protein synthesis.[36] Change in protein expression can make direct comparisons to calibration curves relating cell number and mCherry fluorescence prepared under normoxic conditions difficult for cell populations experiencing different oxygen tensions. The collected images allowed us to make relative comparisons of spatial and temporal changes in viable cell populations for cultures incubated at 24-, 72-, 120-, and 168-h intervals (**Fig. C4.2a**).

Increased periods of incubation resulted in notable changes in the distribution of viable cells (**Fig. 4.2a**). To help visualize relative changes in cell distributions across the multiple incubation intervals, we normalized the average fluorescence intensity of each incubation interval to the respective intensity at 24 h (**Fig. 4.2b**). From these data, three trends appear: i) cells in the first three scaffolds increase in number in the first 72 h, but experience a decrease in viability during the remainder of the incubation; ii) cells in scaffolds 4-6 remain static for the first 72 h, then decrease in viability; and iii) cells in scaffolds 7-12 decline in viability during the first 72 h, and remain static for the remainder of the incubation.

The rapid cellular growth followed by a decline in viability in the first three scaffolds is likely due to temporal imbalances between nutrient supply and cellular consumption. In the first 72 h, this region's close proximity to the nutrient-rich medium allows cells to rapidly proliferate.

After 72 h, we speculate that the rate of consumption outpaces diffusional delivery of nutrients, and that the observed decrease in viability is due to this nutrient shortage.

The temporal changes in viable cell populations within scaffolds 4-6 further support our hypothesis above. Within the first 72 h of the incubation, cell populations in scaffolds 4-6 had stable fluorescence intensities, suggesting that adequate nutrients were reaching this region. After 72 h, scaffolds 4-6 had a decrease in fluorescence intensity, reaching values similar to those measured in scaffolds 7-12. The similarity in fluorescence intensities suggests these regions are experiencing similar levels of nutrient restriction. Experiments mapping glucose concentrations throughout spheroids showed minimal glucose penetration into a spheroid after 120 μm.[37] This distance corresponds to scaffold 4 in the stacked culture, and further supports that nutrient consumption within scaffolds 1-3 is limiting nutrient supply to lower layers.

4.3.3 Proliferative populations occur within 90 μm of the nutrient source

To confirm the presence of proliferative subpopulations in the stacked culture, we stained individual scaffolds for Ki-67 after 24, 72, 120, and 168 h of incubation (**Fig. 4.2c**). We chose Ki-67 as it is a nuclear protein expressed during all stages of the cell cycle.[38] Proliferative cell populations were identified within the first three scaffolds after 72, 120, and 168 h of incubation. This region matches the increased number of viable cells in the first 72 h. Despite the decrease in the number of viable cells between scaffolds 1-3 after 72 h of incubation, proliferation markers in this region persisted for up to 168 h. It is possible that cells in these layers continue to proliferate but at a rate that is slower than the rate of cellular death, explaining why total viability declines over time.

Cell populations in layers 4-12 of the stacked cultures have limited Ki-67 staining. This data, in combination with the mCHR fluorescence intensities, indicate that cells in these regions were viable but not proliferative. The combination of these observations suggests that these cells are likely in a quiescent state to accommodate the limited supply of nutrients within this region. We expect these cells to exhibit an increased resistance to therapeutic dosing which accompanies with the development of a quiescent phenotype.[39]

4.3.4 Oxygen gradients can be modulated with cell density

To better understand the environmental conditions within our PBCs, we incorporated oxygen sensors into the stacked cultures and quantified extracellular oxygen tensions in different regions. We chose to quantify oxygen as it directly regulates hypoxia-inducible transcription factors (HIFs), which promote cellular survival in nutrient deficient conditions,[40] and the development of a chemoresistant phenotype.[41,42] These transcription factors are constitutively expressed by cells but degraded under normal oxygen tensions (i.e., normoxia). Under low oxygen tensions (i.e., hypoxia, < 5 mmHg O_2)—conditions commonly found in poorly vascularized tumor tissue—these factors are stabilized and affect transcription.[41] By quantifying oxygen tensions across our cultures, we can spatially relate cellular responses to the oxygen environment experienced by those cells.

The oxygen sensors used in this study were easily integrated into PBCs by simply placing them at the bottom of the PBC in lieu of the closed PET film in **Fig. 4.1**. These sensors were previously used to map the formation of oxygen gradients in PBCs with channel-type cultures.[43] These sensors are selective to molecular oxygen and highly sensitive at low oxygen tensions, with a resolution of 0.5 mmHg O_2 for measurements below 10 mmHg O_2.[20] In the stacked PBCs

oxygen gradients run normal to the sensor, limiting our measurements to a single point along the gradient. This limitation was overcome by preparing a number of stacked cultures with either 1, 4, 8, or 12 scaffolds, and using each of the readings to estimate the gradient formed across an entire culture with 12 scaffolds. In our setup, the luminescence intensity of the sensors was recorded with an inverted microscope and converted to oxygen tension using a Stern-Volmer relationship.

We measured the spatiotemporal evolution of oxygen gradients in 12-scaffold cultures seeded at two cell densities: 84,000 cells/zone, and 21,000 cells/zone. The oxygen measurements of the culture with 84,000 cells/zone confirm the presence of a steep oxygen gradient, with widespread hypoxia across all scaffolds and time points (**Fig. 4.3**). **Fig. C4.3** provides a graphical summary of the average oxygen tension and standard deviation values for each culture. Previous studies measuring oxygen gradients in tumor xenografts found that oxygen penetrates ~50 μm into tissue before reaching hypoxia,[44] so it was unexpected that these cultures would reach hypoxia in less than 30 μm from the oxygen source. We note that the track etch membranes placed at the top of cultures can act as a mass transport barrier and attenuate oxygen flux into the PBCs, resulting in steeper oxygen gradients than expected.

Despite the cultures experiencing similar oxygen tensions across all scaffolds, we still observed spatial differences in proliferative cell populations. These differences indicate that nutrients other than oxygen were also affecting cellular stratification. Glucose gradients could explain the spatial differences in proliferation we observed, as this molecule has been shown to penetrate further into avascular tumorous tissue than oxygen.[45] Additionally, HCT116 cells under hypoxic conditions have increased glycolytic activity via HIF-1α expression, allowing them to continue to proliferate despite a limited supply of oxygen.[46]

An advantage of the PBCs over spheroids is the ability to modulate the density of cells in each scaffold. Seeding PBCs at 21,000 cells/zone lowered overall cellular consumption and permitted oxygen to penetrate ~240 μm (**Fig. 4.3**). At this density, a 1-scaffold culture took 120 h to reach hypoxia, while a 4-scaffold culture took 72 h. By further modulating the cell density, we would expect oxygen penetration to change accordingly, allowing us to readily control the steepness and duration of these gradients. Additional chemical sensors capable of measuring nutrient, pH, and waste products are needed to corroborate the evolution of these gradients.

4.3.5 Different chemical conditions yield different chemoresistances

The ability to manipulate local chemical gradients in the stacked cultures allowed us to investigate how the chemical environment contributes to regional differences in phenotype and chemoresistance. To measure the drug sensitivity of HCT116 cells in 12-scaffold cultures, we exposed cultures seeded with two different cell densities (84,000 or 21,000 cells/zone) to varying concentrations of SN-38. SN-38 is a topoisomerase I inhibitor and the active metabolite of irinotecan, which is commonly used in combination therapies for colorectal cancer.[47] In these experiments, cultures were incubated for 24 h before being exposed to SN-38. After 48 h of dosing, the cultures were disassembled and mCHR fluorescence intensities were measured. Relative chemoresistance in each scaffold was determined by comparing the fluorescence intensity of SN-38 dosed scaffolds to the fluorescence intensity of scaffolds exposed to the vehicle.

Prior to performing the chemoresistance assays, we characterized: i) penetration of fluorescein, an SN-38 substitute, into the stacked cultures, and ii) the response of HCT116 mCHR cells to increasing doses of SN-38 in 3D and monolayer cultures. Small-molecule

penetration into the stacked cultures was assessed to ensure that differences in relative chemoresistance can be attributed to drug interactions rather than inaccessibility to SN-38. To estimate the penetration of SN-38 throughout the stacked culture, we substituted sodium fluorescein for SN-38. We chose fluorescein because it can be easily measured using fluorescence microscopy and possesses a diffusion coefficient similar to an SN-38 analogue.[48,49] For this assay, a 0.5 mg/mL solution of fluorescein was added to the top of a 12-scaffold PBC seeded at a density of 84,000 cells/zone. We recorded the fluorescence intensity at the bottom of a culture over a period of 11 hours (**Fig. C4.4**). After ~350 minutes the fluorescein signal became static, indicating that equilibrium had been reached throughout the culture. These data suggest that the top of the culture will see increased concentrations of SN-38 relative to the bottom scaffolds for the first 350 minutes of dosing, ~13% of the total incubation time. Additionally, HCT116 cells suspended in a 3D matrix have doubling times of approximately 74 hours, which means that cells will likely experience the full SN-38 concentration before completing a division.[50]

We determined the potency (half maximal inhibitory concentration, IC_{50}) of SN-38 for well-oxygenated HCT116 mCHR cells cultured in single-zone paper scaffolds and monolayers. While previous studies have already characterized the IC_{50} of SN-38 for HCT116 cells in 2D cultures, these values range three orders of magnitude (50 - 0.5 nM) making comparisons with literature values difficult.[34,51] The IC_{50} value for the HCT116 cells in the paper scaffolds (0.014 ± 0.006 μM) was much higher than for monolayer cultures (0.005 ± 0.001 μM). These data are summarized in **Fig. C4.5**. These results support previous findings that 2D cultures often overestimate the potency and efficacy of chemotherapeutics relative to 3D cultures and by extension, *in vivo* tumors.[4]

To assess regional chemoresistance in stacked PBCs, 12-scaffold cultures were dosed with increasing concentrations of SN-38: 0.014 μM, 0.14 μM, or 1.4 μM, representing 1x, 10x, or 100x of the 3D IC_{50} value. A vehicle control of 0.1% (v/v) DMSO in medium was also included in this assay. Fluorescence measurements from the chemoresistance assay show distinct differences in regional responses between scaffolds at different SN-38 dosages (**Fig. 4.4**). A table outlining statistical comparisons between dosages is provided in Appendix 3 (**Table C4.1**).

Cultures seeded with 84,000 cells/zone and dosed with 0.014 μM or 0.14 μM SN-38 had a significant decrease in viable cells between scaffolds 2-5. The decrease in viability was expected for scaffold 2 based on the Ki-67 staining; however, SN-38's effectiveness was less predictable for scaffolds 3-5 due to the limited proliferation measured within this region. This sensitivity to SN-38 in the non-proliferative region can be explained by SN-38's ability to inhibit HIF-1α expression.[52] While the mechanism is not well understood, increasing concentrations of SN-38 decrease levels of HIF-1α in the colorectal carcinoma cell lines HT29 and SW480. A similar dose-response relationship could be happening in our cultures. The attenuation of HIF-1α accumulation via SN-38 should decrease the induction of antiapoptotic pathways in the HCT116 mCHR cells between scaffolds 3-5, decreasing their overall chemoresistance.

Chemoresistance assays for 0.014 μM and 1.4 μM SN-38 were also performed on stacked cultures containing 21,000 cells/zone. From these data, there is a clear trend between the 0.014 μM SN-38 and the vehicle data, as scaffolds 2-12 were statistically similar. A table outlining statistical comparisons between all dosages is provided in Appendix 3 (**Table C4.2**). The only significant difference between the vehicle and 0.014 μM SN-38 data sets was the first scaffold, in which 0.014 μM SN-38 had significantly fewer viable cells. The similarity in viable

cells between scaffolds 2-12 suggests that cells further from the medium source exhibit increased chemoresistance.

Dosing the cultures seeded with different cell densities showed distinctly different trends: cells in the first scaffold were responsive to SN-38 at low-densities but not at high-densities. Additionally, cells deeper in the high-density culture were responsive to SN-38 dosing while cells in the low-density cultures were not. The disparity in these results highlight the shifting relationship between cancer chemoresistance and local chemical environment, and show the need for a model capable of accounting for environmental components when assessing chemotherapeutic effectiveness.

4.4 Conclusion

This work utilized stacked PBCs to relate chemoresistance of colorectal carcinoma cells to their local chemical environment. In these assemblies, monotonic gradients of nutrients and waste are formed across the stacked culture, providing a range of chemical environments that vary for each scaffold. By modulating the cell density of these PBCs, we can experimentally manipulate the spatiotemporal evolution of these gradients to suit experimental needs. We incorporated oxygen sensors into the cultures seeded with different cells densities to demonstrate this control, and found shallower oxygen gradients in cultures with lower cell densities. Cultures seeded at different cell densities were also dosed with SN-38. Interestingly, we found a significantly higher response to SN-38 dosing in high-density cultures experiencing hypoxia. The difference in response between these densities demonstrate the modularity of PBCs and their ability to easily assess spatial relationships between chemical environments and chemoresistance.

While there are a number of 3D culture platforms to assess chemotherapeutic effectiveness *in vitro*, the ability to i) manipulate the chemical environment *in situ*, and ii) easily section cultures into discrete layers, makes PBCs a promising analytical tool for screening therapeutics. The cultures described in this work used one cell line and one chemotherapeutic agent; however, the modularity of this platform allows cell lines and therapeutics to easily be interchanged or combined into a single assay. Additional biomarkers other than Ki-67 can also be investigated to relate specific phenotypic changes in the presence and absence of therapeutics. This work will serve as the first in a series of studies that focus on developing PBCs as a platform for screening therapeutics.

4.5 Figures

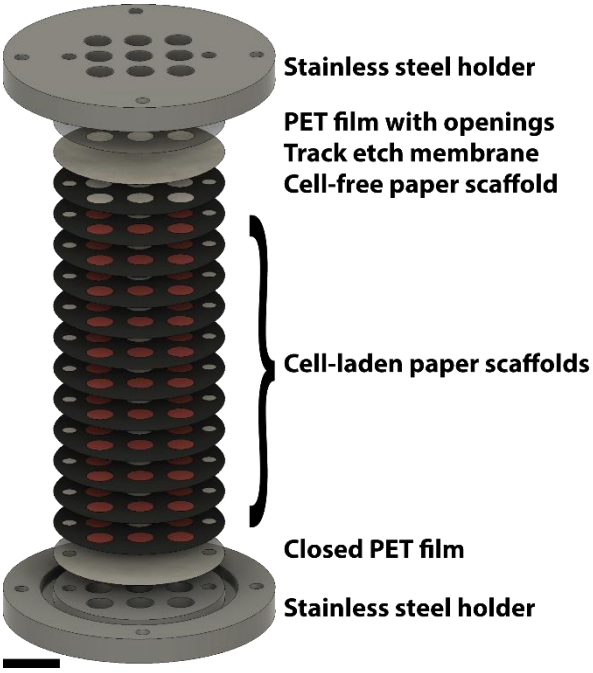

Figure 4.1 Schematic of the 12-scaffold PBC. The experimental setups used in this study consisted of 12 paper scaffolds, a track etch membrane, and two PET films sandwiched between two stainless steel metal holders. The paper-scaffolds were used to form the cultures by stacking together 11 cell-containing scaffolds with a cell-free scaffold at the top. The track etch membrane confined the HCT116 cells in the paper scaffolds. The two PET films limited the diffusional exchange with the surrounding medium to the top of the stack. The stainless-steel holders compressed the entire culture together, and ensured the scaffolds were in conformal contact throughout the experiment. (scale bar = 9 mm)

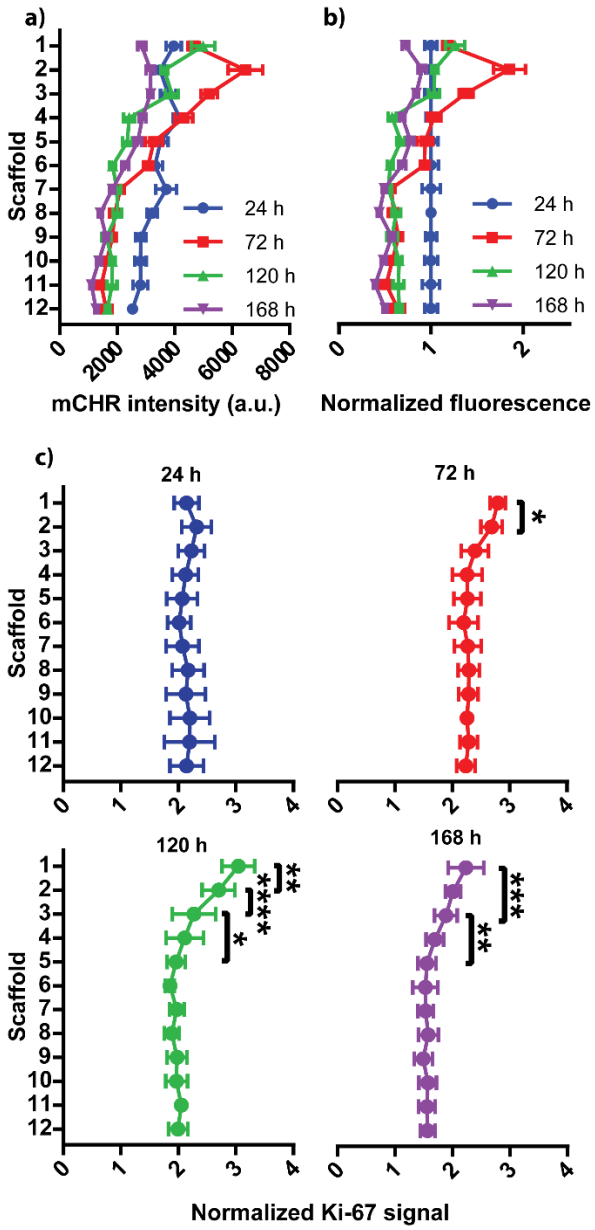

Figure 4.2 Stratification of viable and proliferative HCT116 cell populations after 24h, 72h, 120h, and 168h of incubation. In each graph, scaffold 1 is at the top of the stack and closest to the source of fresh medium. (a) mCHR fluorescence intensity was used to assess cellular viability in each scaffold of the stack, increased fluorescence correlates with increased viability. n = 14-29 replicate measurements, across multiple setups and cell passage numbers. (b) mCHR fluorescence intensities were normalized to the 24 h values to help visualize relative changes per scaffold over time. (c) Immunocytochemistry (Ki-67) was used to identify proliferative populations along the cultures. Fluorescence intensity of secondary labeled anti-Ki-67 antibodies were normalized to mCHR fluorescence intensity. Cells in the top 3 scaffolds exhibit increased Ki-67 expression after 24 h, indicating the presence of proliferative populations. n = 10-15 replicate measurements, across multiple setups and cell passage numbers. (* = $p < 0.05$, ** = $p < 0.01$, *** = $p < 0.001$, **** = $p < 0.0001$)

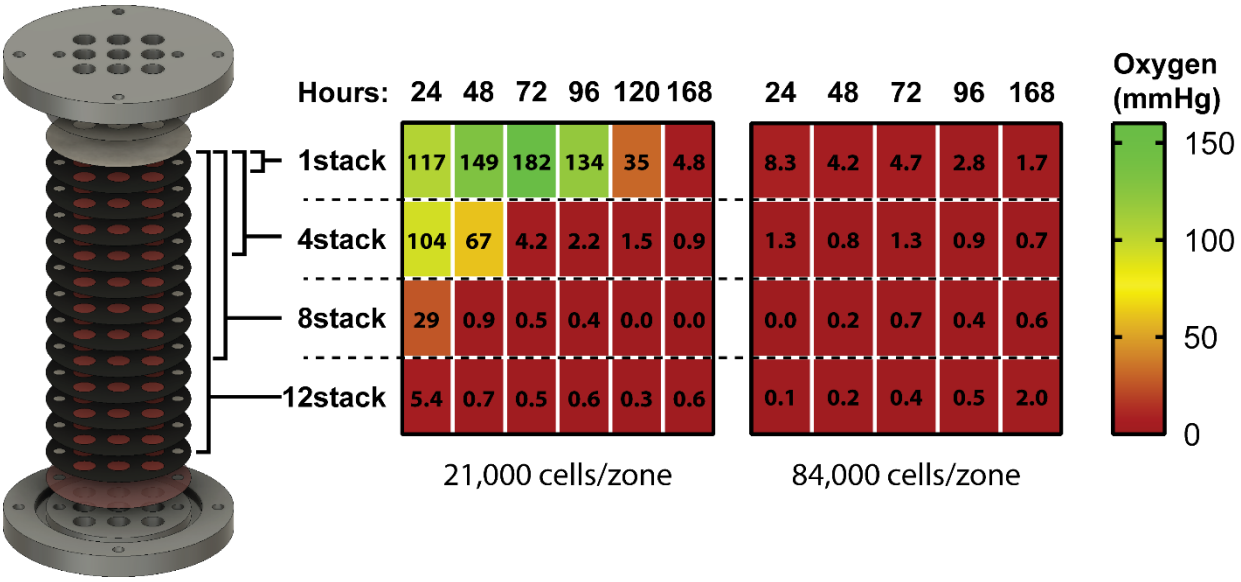

Figure 4.3. Mapping oxygen tension along stacked cultures containing different cell densities: 21,000 cells/zone (left) and 84,000 cells/zone (right). Oxygen sensors were placed at the bottom of cultures composed of 1-, 4-, 8-, and 12-stacked scaffolds. The corresponding heat maps and values represent the average oxygen tension at the bottom of these cultures, with green representing atmospheric oxygen tensions (160 mmHg) and red representing hypoxia (< 5 mmHg). n=5 replicate measurements, obtained from a single setup.

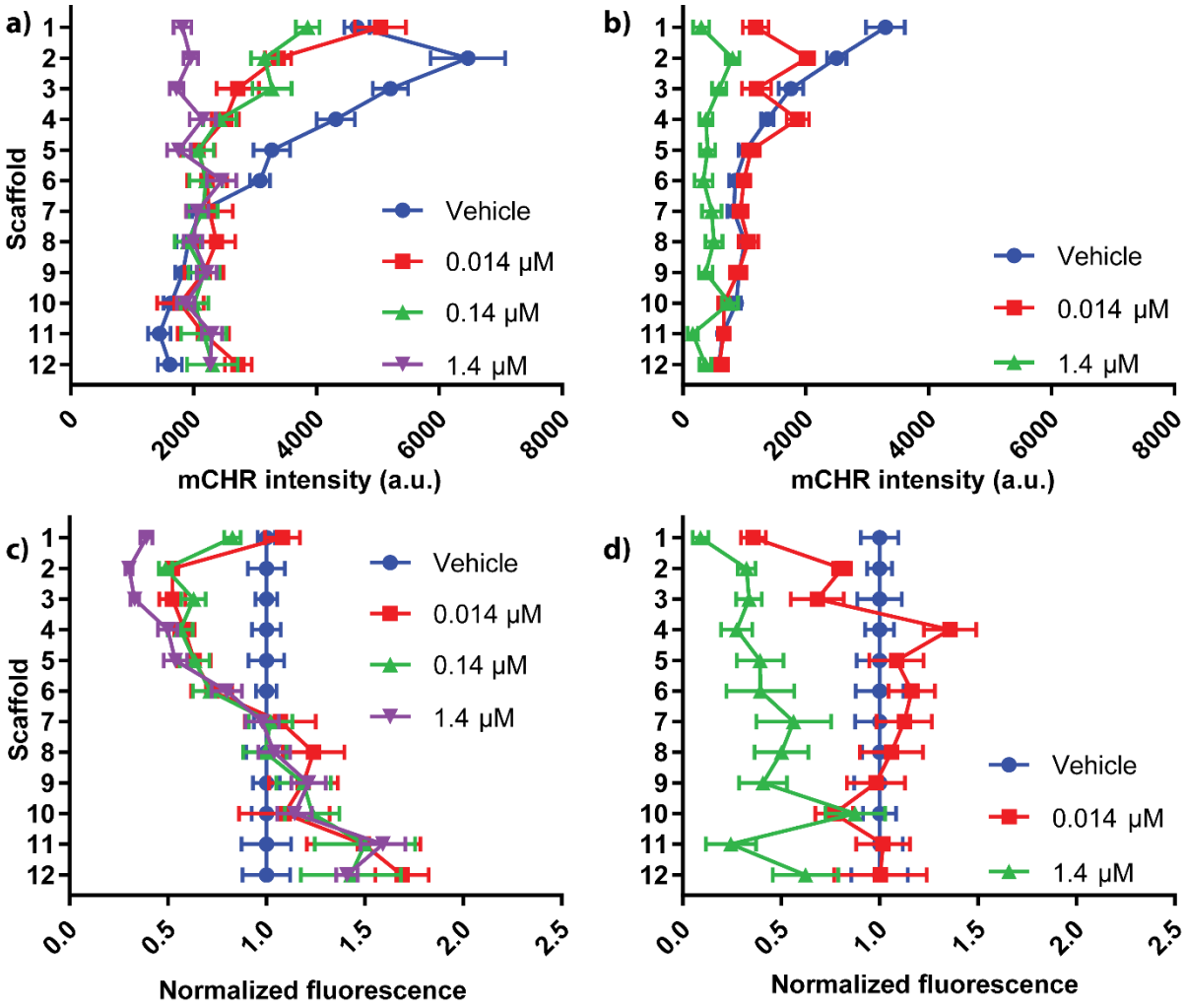

Figure 4.4 Density-dependent responses to SN-38 dosing. Stacked PBCs were seeded with either (a) 84,000 cells/zone or (b) 21,000 cells/zone and dosed with increasing concentrations of SN-38. The viability at each zone was measured using fluorescence imaging and compared to vehicle controls. mCHR fluorescence intensities were normalized to the 24 h values of the (c) 84,000 cells/zone and (d) 21,000 cells/zone cultures to help visualize relative changes for each dosage. n = 15 replicate measurements, across multiple setups and cell passage numbers.

REFERENCES

(1) Breslin, S.; O'Driscoll, L. *Drug Discov. Today* **2013**, *18* (5–6), 240–249.

(2) Edmondson, R.; Broglie, J. J.; Adcock, A. F.; Yang, L. *Assay Drug Dev. Technol.* **2014**, *12* (4), 207–218.

(3) Imamura, Y.; Mukohara, T.; Shimono, Y.; Funakoshi, Y.; Chayahara, N.; Toyoda, M.; Kiyota, N.; Takao, S.; Kono, S.; Nakatsura, T.; Minami, H. *Oncol. Rep.* **2015**, *33* (4), 1837–1843.

(4) Karlsson, H.; Fryknäs, M.; Larsson, R.; Nygren, P. *Exp. Cell Res.* **2012**, *318* (13), 1577–1585.

(5) Hakkinen, K. M.; Harunaga, J. S.; Doyle, A. D.; Yamada, K. M. *Tissue Eng. Part A* **2011**, *17* (5–6), 713–724.

(6) Luca, A. C.; Mersch, S.; Deenen, R.; Schmidt, S.; Messner, I.; Schäfer, K. L.; Baldus, S. E.; Huckenbeck, W.; Piekorz, R. P.; Knoefel, W. T.; Krieg, A.; Stoecklein, N. H. *PLoS One* **2013**, *8* (3), 1–11.

(7) Friedrich, J.; Seidel, C.; Ebner, R.; Kunz-Schughart, L. A. *Nat. Protoc.* **2009**, *4* (3), 309–324.

(8) Katt, M. E.; Placone, A. L.; Wong, A. D.; Xu, Z. S.; Searson, P. C. *Front. Bioeng. Biotechnol.* **2016**, *4* (February), 12.

(9) Liu, X.; Weaver, E. M.; Amanda B. Hummon. *Anal. Chem.* **2013**, *85* (13), 6295–6302.

(10) Liu, X.; Hummon, A. B. *Sci. Rep.* **2016**, *6* (December), 38507.

(11) LaBonia, G. J.; Lockwood, S. Y.; Heller, A. A.; Spence, D. M.; Hummon, A. B. *Proteomics* **2016**, *16* (11–12), 1814–1821.

(12) Grimes, D. R.; Kelly, C.; Bloch, K.; Partridge, M. *J. R. Soc. Interface* **2014**, *11* (92), 20131124.

(13) Hirschhaeuser, F.; Menne, H.; Dittfeld, C.; West, J.; Mueller-Klieser, W.; Kunz-Schughart, L. A. *J. Biotechnol.* **2010**, *148* (1), 3–15.

(14) Lin, R. Z.; Chang, H. Y. *Biotechnol. J.* **2008**, *3* (9–10), 1172–1184.

(15) Sutherland, R. M.; Sordat, B.; Bamat, J.; Gabbert, H.; Bourrat, B.; Mueller-Klieser, w. *Cancer Res.* **1986**, *46* (October), 5320–5329.

(16) Schroll, M. M.; Liu, X.; Herzog, S. K.; Skube, S. B.; Hummon, A. B. *Nutr. Res.* **2016**, *36*

(10), 1068–1080.

(17) Kunz-Schughart, L.; Freyer, J.; Hofstaedter, F.; Ebner, R. *J. Biomol. Screen.* **2004**, *9* (4), 273–285.

(18) Pampaloni, F.; Reynaud, E. G.; Stelzer, E. H. K. *Nat. Rev. Mol. Cell Biol.* **2007**, *8* (10), 839–845.

(19) Liu, X.; Hummon, A. B. *J. Am. Soc. Mass Spectrom.* **2015**, *26* (4), 577–586.

(20) Boyce, M. W.; Kenney, R. M.; Truong, A. S.; Lockett, M. R. *Anal. Bioanal. Chem.* **2016**, *408* (11), 2985–2992.

(21) Truong, A. S.; Lochbaum, C. A.; Boyce, M. W.; Lockett, M. R. *Anal. Chem.* **2015**, *87* (22), 11263–11270.

(22) Truong, A. S.; Lockett, M. R. *Analyst* **2016**, 3874–3882.

(23) Kenney, R. M.; Boyce, M. W.; Truong, A. S.; Bagnell, C. R.; Lockett, M. R. *Analyst* **2015**, *141*, 661–668.

(24) Rodenhizer, D.; Gaude, E.; Cojocari, D.; Mahadevan, R.; Frezza, C.; Wouters, B. G.; McGuigan, A. P. *Nat. Mater.* **2016**, *15* (2), 227–234.

(25) Mosadegh, B.; Lockett, M. R.; Minn, K. T.; Simon, K. A.; Gilbert, K.; Hillier, S.; Newsome, D.; Li, H.; Hall, A. B.; Boucher, D. M.; Eustace, B. K.; Whitesides, G. M. *Biomaterials* **2015**, *52* (1), 262–271.

(26) Camci-Unal, G.; Newsome, D.; Eustace, B. K.; Whitesides, G. M. *Adv. Healthc. Mater.* **2016**, *5* (6), 641–647.

(27) Mosadegh, B.; Dabiri, B. E.; Lockett, M. R.; Derda, R.; Campbell, P.; Parker, K. K.; Whitesides, G. M. *Adv Heal. Mater* **2014**, *3* (7), 1036–1043.

(28) Derda, R.; Laromaine, A.; Mammoto, A.; Tang, S. K. Y.; Mammoto, T.; Ingber, D. E.; Whitesides, G. M. *Proc. Natl. Acad. Sci. U. S. A.* **2009**, *106* (44), 18457–18462.

(29) Deiss, F.; Mazzeo, A.; Hong, E.; Ingber, D. E.; Derda, R.; Whitesides, G. M. *Anal. Chem.* **2013**, *85*, 8085–8094.

(30) Lloyd, C. C.; Boyce, M. W.; Lockett, M. R. *Curr. Protoc. Chem. Biol.* **2017**, *9*, 1–20.

(31) Schneider, C. a; Rasband, W. S.; Eliceiri, K. W. *Nat. Methods* **2012**, *9* (7), 671–675.

(32) Minchinton, A. I.; Tannock, I. F. *Nat. Rev. Cancer* **2006**, *6* (8), 583–592.

(33) Mitchison, T. J. *Mol. Biol. Cell* **2012**, *23* (1), 1–6.

(34) Jensen, N. F.; Agama, K.; Roy, A.; Smith, D. H.; Pfister, T. D.; Romer, M. U.; Zhang, H. L.; Doroshow, J. H.; Knudsen, B. R.; Stenvang, J.; Brunner, N.; Pommier, Y. *J. Exp. Clin. Cancer Res.* **2016**, *35* (1), 56.

(35) Colom, A.; Galgoczy, R.; Almendros, I.; Xaubet, A.; Farré, R.; Alcaraz, J. *J. Biomed. Mater. Res. - Part A* **2014**, *102* (8), 2776–2784.

(36) Koumenis, C.; Naczki, C.; Koritzinsky, M.; Rastani, S.; Diehl, A.; Sonenberg, N.; Koromilas, A.; Wouters, B. G. *Mol. Cell. Biol.* **2002**, *22* (21), 7405–7416.

(37) Milotti, E.; Chignola, R. *PLoS One* **2010**, *5* (11).

(38) Scholzen, T.; Gerdes, J. *J. Cell. Physiol.* **2000**, *182* (3), 311–322.

(39) Gordon, R. R.; Nelson, P. S. *Drug Resist. Updat.* **2012**, *15* (1–2), 123–131.

(40) Sullivan, R.; Graham, C. H. *Cancer Metastasis Rev.* **2007**, *26* (2), 319–331.

(41) Sullivan, R.; Paré, G. C.; Frederiksen, L. J.; Semenza, G. L.; Graham, C. H. *Mol. Cancer Ther.* **2008**, *7* (7), 1961–1973.

(42) Semenza, G. L. *Trends Pharmacol Sci.* **2013**, *33* (4), 207–214.

(43) Boyce, M. W.; Kenney, R. M.; Truong, A. S.; Lockett, M. R. *Anal. Bioanal. Chem.* **2015**, 1–8.

(44) Helmlinger, G.; Yuan, F.; Dellian, M.; Jain, R. K. *Nat. Med.* **1997**, *3* (2), 177–182.

(45) Gatenby, R. A.; Gillies, R. J. *Nat. Rev. Cancer* **2004**, *4* (11), 891–899.

(46) Dang, D. T.; Chen, F.; Gardner, L. B.; Cummins, J. M.; Rago, C.; Bunz, F.; Kantsevoy, S. V.; Dang, L. H. *Cancer Res.* **2006**, *66* (3), 1684–1693.

(47) Wallin, A.; Svanvik, J.; Holmulund, B.; Ferreud, L.; Sun, X.-F. *Oncol. Rep.* **2008**, *19* (6), 1493–1498.

(48) Kunadharaju, S.; Savva, M. *J. Chem. Eng. Data* **2010**, *55* (1), 103–112.

(49) Culbertson, C. T.; Jacobson, S. C.; Michael Ramsey, J. *Talanta* **2002**, *56* (2), 365–373.

(50) Fang, J. Y.; Tan, S.-J.; Wu, Y.-C.; Yang, Z.; Hoang, B. X.; Han, B. *J. Transl. Med.* **2016**, *14* (1), 38.

(51) Niizuma, S.; Tsukazaki, M.; Suda, H.; Murata, T.; Ohwada, J.; Ozawa, S.; Fukuda, H.;

Murasaki, C.; Kohchi, M.; Morikami, K.; Yoshinari, K.; Endo, M.; Ura, M.; Tanimura, H.; Miyazaki, Y.; Takasuka, T.; Kawashima, A.; Nanba, E.; Nakano, K.; Ogawa, K.; Kobayashi, K.; Okabe, H.; Umeda, I.; Shimma, N. *Bioorganic Med. Chem. Lett.* **2009**, *19* (7), 2018–2021.

(52) Murono, K.; Tsuno, N. H.; Kawai, K.; Sasaki, K.; Hongo, K.; Kaneko, M.; Hiyoshi, M.; Tada, N.; Nirei, T.; Sunami, E.; Takahashi, K.; Kitayama, J. *Anticancer Res.* **2012**, *32* (3), 865–872.

CHAPTER 5: FUTURE DIRECTIONS ADAPTING PAPER-BASED CULTURES FOR FLOW CYTOMETRY

5.1 Introduction

The future goal of the work outlined in this dissertation is to develop a single, comprehensive assay capable of i) evaluating the effectiveness of chemotherapeutics in a tumor-like environment, and ii) identifying how cells evade cytotoxic agents. Development of chemoresistance in cancer cells is a major obstacle to cancer treatment, and results from changes in drug metabolism,[1–3] expression of efflux pumps,[4–6] expression of drug targets,[7–10] genetic regulation via methylation or mutation,[11–15] and regulation of cell cycle/apoptosis.[16–18] While chemotherapeutics are often evaluated on their short-term efficacy in reducing tumor bulk, cells can acquire resistance to therapeutics during treatment and reemerge as a more aggressive cancer.[19,20] Additionally, cells can develop innate resistances to therapeutics through mechanisms involving the tumor microenvironment (TME).[21,22] Understanding the relationship between the TME environment and resistance to individual chemotherapeutics provides insight on potential combinatorial therapeutic regimes to prevent relapse.

Chapter 4 outlined a PBC setup designed to discern differences in chemosensitivity between cell populations experiencing different microenvironments.[23] In that assay, viable cells were identified based on their expression of a constitutively expressed fluorescent protein, mCherry. Despite being able to correlate fluorescence intensity to relative viability, the persistence of fluorescent proteins during the process of cellular death limits the accuracy of this

readout.[24] Additionally, this assay does not identify the specific cellular mechanisms that allowed cells to evade chemotherapeutic agents. Due to the limitations of the single end-point readout used in our initial work, a new readout is needed capable of simultaneously i) identifying viable, dead, and apoptotic cells and ii) assessing different phenotypes that contribute to chemoresistance. To develop this assay, I turned to flow cytometry.

Flow cytometry is a bioanalytical technique in which fluorescently-labeled cell suspensions are drawn into a microfluidics system, orientated into a line, and then individually interrogated with light. The ability to isolate and analyze single cells within a suspension enables this technique to study cellular heterogeneity within a population. Flow cytometry has been used to study chemosensitivity of cancer cells[25,26] and identify chemoresistant phenotypes, including: efflux pump activity,[27,28] apoptosis suppression,[29] and cell-cycle modulation.[30] Flow cytometric protocols have also been developed to discriminate between live and dead cells, and rely on three staining techniques: nuclear incorporation of DNA intercalating dyes, metabolism of fluorogenic substrates, and binding of amine-reactive dyes to intracellular proteins. While these staining techniques rely on different labeling mechanisms, they all differentiate live and dead cells based on whether the cell membrane is intact or compromised.

In this chapter, I outline my current work focused on adapting paper-based cultures (PBCs) for flow cytometric analysis. To develop this workflow, I adjusted the design of the paper scaffolds to accommodate for the number of cells necessary for flow cytometry (~$2x10^6$ cells). I then developed protocols to extract, and stain cells for viability and apoptosis. Future work will focus on incorporating additional stains to identify senescent cells and difference in the expression of efflux pumps. The resulting assay will consist of a paper-based culture capable of

correlating relative chemosensitivity to mechanisms that allow cells to escape cytotoxic molecules.

5.2 Ongoing work

5.2.1 Designing a paper-based culture for flow cytometry

To adapt the PBC outlined in Chapter 4 for flow cytometric analysis, I changed the design of both the paper scaffolds and the holders (**Fig. 5.1**). Changes to the paper were made to accommodate the large number of cells needed to accurately measure population distributions by flow cytometry. In the assay described in Chapter 4, the nine-zone scaffolds contained $4.2x10^5$ cells. While literature does not define the minimum number of cells needed to accurately assess population distributions by flow cytometry, protocols provided by flow cytometry facilities often recommend analyzing at least $5x10^4$ cells and starting assays with ~$2x10^6$ cells to account for losses during sample preparation/staining. Using these recommendations, I augmented the paper scaffolds to hold $2x10^6$ cells at the same cell density used in Chapter 4 (168,000 cells/µL). To achieve this cell number, I adjusted the diameter of the paper and removed the wax patterns. These changes allowed me to access more volume of the paper scaffolds, greatly increasing the number of cells a single scaffold can hold. It is worth noting two observations: the diameter of the paper scaffold can be changed with respect to cell density to ensure that $2x10^6$ cells are always seeded per scaffold; and wax patterns will disintegrate into particulate during post-incubation extraction and staining, which is why no new wax patterns were developed for assays described in this chapter.

Changes to paper design also required changes to the holder. For these experiments, I adopted fabrication techniques outlined in Chapter 3 and used laser-cut, biocompatible acrylic

holders. The opening on the top acrylic holder is readily modified to match the diameter of the paper scaffolds used for a particular assay. Relative to the metal holders depicted in Chapter 1, 2, and 4, fabrication of the acrylic holders is straightforward, as it does not require equipment or expertise necessary for machining stainless steel.

5.2.2 Extracting cells from a paper-based culture

Flow cytometric analysis of PBCs requires the cells to be extracted from their paper scaffolds. To recover the cells from their Matrigel environment, I used a proprietary solution specifically developed to depolymerize Matrigel (Cell Recovery Solution, Corning). Cells were recovered by incubating the scaffolds in the recovery solution for 4 h at 4 ºC with intermittent agitation. After the extraction, cells were centrifuged, washed, and prepared for staining. The conditions for staining were recommended by the manufacturer and provided a recovery rate of 84% of the cells.

To ensure cell viability was not affected by the extraction process, HCT-116 cells were incubated in either static medium or in the recovery solution with increasing amounts of agitation. Viability was determined by staining with a positive marker for live cells (fluorescein diacetate, FDA) and a positive marker for dead cells (7-aminoactinomycin D, 7-AAD). By using a two-dimensional analysis for viability, separation between the two populations becomes more pronounced and easier to identify. From the flow cytometric analysis of the live and dead cells, three populations were seen: cells positively stained for 7-AAD, cells positively stained for FDA, and cells negatively stained for both dyes. (**Fig 5.2**) The percent of unstained cells increased with agitation in recovery solution, suggesting that the recovery solution affected the metabolism of FDA. While it is not clear what inhibited this reaction, these results show that FDA should not be

used to positively identify viable cells post extraction. Comparing the distribution of positively stained 7-AAD cells across all replicates showed there is no significant increase in dead cell populations during the extraction (**Fig 5.3**). These findings indicate that the extraction does not cause cell death.

5.2.3 Discerning between live, dead, and apoptotic cells

Identification of viable cell populations was performed using two fluorescent stains: an amine reactive dye (Zombie Green™, BioLegend), and annexin V labeled with pacific blue (ThermoFisher). As described in Chapter 1, amine reactive dyes covalently bond to free amines on proteins; dead/dying cells with compromised membranes allow the dye to access intracellular proteins, greatly increasing staining relative to viable cells.[31] By incorporating annexin V into the staining regime, cells experiencing early-stage apoptosis with intact membranes can also be discerned from viable cells.[32] It is important to note that amine reactive dyes are compatible with cellular fixation and permeabilization; however, the staining regime proposed in this chapter will not require fixation or permeabilization.

After optimizing dye concentration via titrations, these dyes were used to assess relative chemosensitivity of colon carcinoma cells (HCT-116) in the PBCs described in section 5.2.1. For this work, the PBCs were assembled by stacking 9 cell-laden paper scaffolds and incubating the assembly for 24 h. After the initial incubation, the PBCs were dosed for 24 h with either a vehicle control or the active metabolite of a chemotherapeutic agent (14 nM SN-38). The assemblies were then taken apart, and the cells were extracted and stained.

Cytograms represent at least $5x10^4$ cells per analysis (**Fig. 5.4**), and data extracted from three different analyses were averaged together to compare chemoresistances across scaffolds

(**Fig. 5.5**). From these preliminary data, it becomes apparent that cells at the top of the stack—close to the nutrient and drug source—are sensitive to SN-38, while cells in the nutrient-poor region exhibit increased chemoresistance. While these results were similar to those seen in Chapter 4, flow cytometry was able to confirm the presence of viable cell populations in scaffolds furthest from the nutrient source.

5.3 Future work

5.3.1 Identifying senescent cell populations

Accumulation of DNA damage from chemotherapeutics can induce response pathways within cancer cells that lead to apoptosis or permanent growth arrest (i.e., senescence).[16] Cells that undergo senescence exhibit unique phenotypes which include increased cell size, granularity, β-galactosidase activity, and secretion of signaling molecules.[16,33] While the induction of senescence can be seen as a means to suppress cancer, senescent cells exhibit increased chemoresistance and have been shown to promote tumor progression through the secretion of cytokines, growth factors, and proteases.[33] Using the assays described in this chapter, stacked PBCs can be used to better understand how local environmental conditions correlate with the induction of cellular senescence.

The most common methods for identifying senescent cells via flow cytometry involves measuring the activity of β-galactosidase.[28,34] These assays are similar to staining with FDA, in that a non-fluorescent galactopyranoside substrate is metabolized into a fluorescent product. The substrates can be labeled with fluorescein or resorufin to modulate their spectral properties, and can also be conjugated to a 12-carbon chain or thiol-reactive moiety to improve cell retention. For assays involving PBCs, I will use resorufin-labeled galactopyranoside, because it is

spectrally compatible with the viability dyes outlined in 5.2.3, and exhibits improved reaction kinetics relative to fluorescein-conjugated substrate.[35] Additionally, the traditional galactopyranoside substrates do not require as much sample preparation relative to substrates modified with cell-retention moieties, as the modified substrates require hypotonic shock to load the dyes into the cell.

Important considerations when using this stain include optimizing the dye loading time and incorporating proper positive controls. The increased secretion of senescent cells promotes the efflux of fluorescent products from the cells,[36] and will require optimization for determining the proper timing of dye loading and analysis. Verapamil, a calcium-channel blocker, can also be used during staining to decrease efflux.[37] During flow cytometric analysis, positive controls will be necessary for determining population gating. Protocols have been developed using camptothecin to induce senescence in HCT-116 cells cultured in two-dimensional (2D);[38] however, it is unclear how β-galactosidase activity translates between 2D and three-dimensional (3D) cultures. Protocols for the induction of senescence in 3D cultures may be necessary for evaluating positive staining in the stacked PBCs.

5.3.2 Evaluating efflux pumps

Hypoxia within cancer cells has been shown to activate multidrug resistant (MDR) genes, which increase the expression of ATP-binding cassette proteins (ABC)—efflux pumps with broad specificity.[21] Increased expression of this transport protein allows cancer cells to expel a wide range of cytotoxic agents, and is associated with the development of a multi-drug resistant phenotype.[39] These proteins are usually more abundant in cancers derived from healthy tissues that normally express ABCs, which includes epithelial colon cells.[5] Overexpression of ABCG2,

a specific ABC, has been shown to impart SN-38 resistance to colon carcinomas, including HCT-116 cells.[40]

Flow cytometric analysis of efflux pumps can be done through two mechanisms: assessment of overall ABC activity through the efflux of fluorescent molecules, or immunostaining with fluorescently-labeled antibodies. A breadth of fluorogenic molecules have been evaluated to optimize assays studying efflux pump activity;[41] however, these assays are time sensitive, and have poor resolution between cells expressing increased levels of ABCs relative to basal levels.[42] Antibodies developed to recognize extracellular sequences of ABCs provide a more direct assessment of changes in efflux pump expression, albeit they do not indicate pump activity. A number of fluorescently-labeled commercial antibodies are available for ABCs, including ABCG2. Due to the availability and simplicity of antibody staining, changes in efflux pump expression will be evaluated in the PBC assay using antibodies recognizing ABCG2.

5.4 Conclusions

The work outlined in this section details current and ongoing efforts to study differential cellular responses to chemotherapeutic dosing of cancer cells. By adapting PBCs for flow cytometric analysis, a comprehensive assay can be developed that is capable of identifying i) heterogenicity in cancer cell responses to therapeutics under different chemical environments, and ii) the cellular mechanisms—senescence induction and efflux pump expression—that cause these differences. While there are other mechanism that affect cellular responses to chemotherapeutics, this work will serve as a foundation for future assays investigating additional mechanisms for chemotherapeutic effectiveness.

5.5 Figures

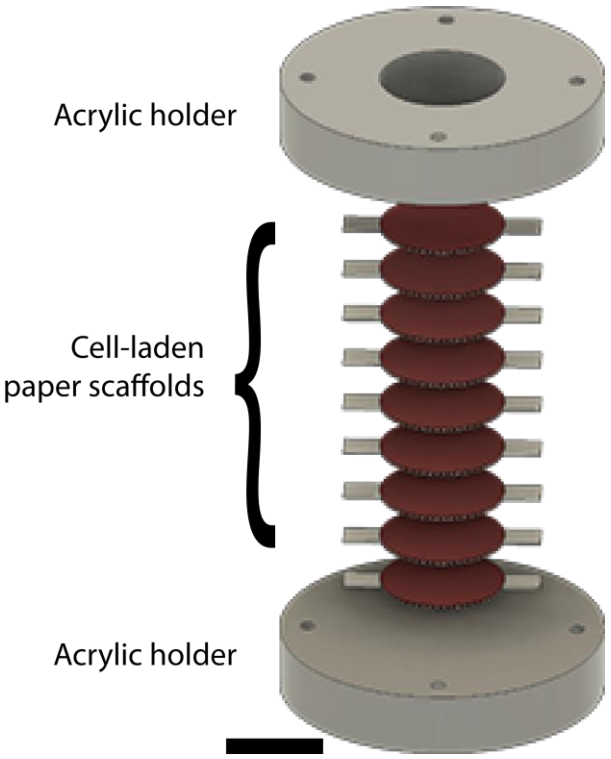

Figure 5.1 Schematic of new PBC design used for flow cytometric analysis. For this assembly, cells were seeded in the circular regions of the paper scaffolds, and assembled between two acrylic holders. The bottom acrylic holder was thread, and the entire enclosure was held together with screws. (scale bar = 10 mm)

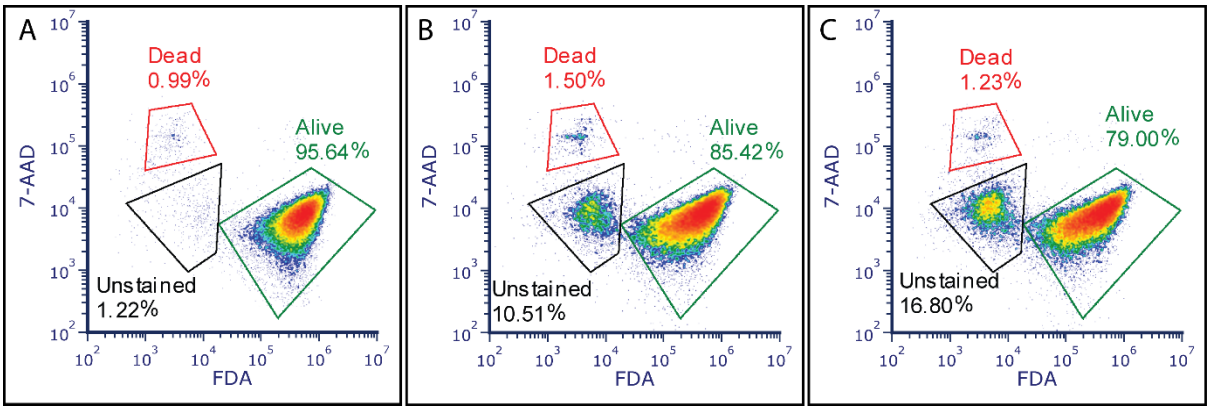

Figure 5.2 Representative cytograms showing the viability of HCT-116 cells incubated in (A) static medium, (B) static cell recovery solution, and (C) vortexed cell recovery solution. Cells were incubated for 4 h, then stained with FDA and 7-AAD to determine viability.

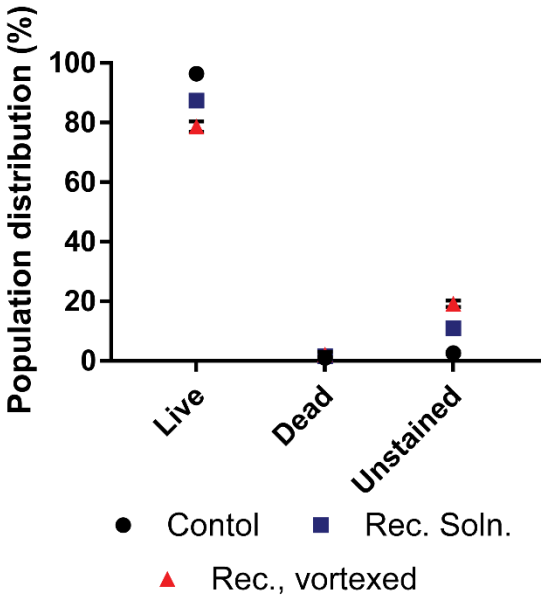

Figure 5.3 The distribution of live, dead, and unstained cells were compared between HCT-116 cells incubated in static medium (Control), cell recovery solution (Rec. Soln.), and vortexed cell recovery solution (Rec., vortex). Cells positively stained for FDA were considered alive, cells positively stained for 7-AAD were considered dead, and double negative stains were considered unstained. Using a two-way ANOVA test with Tukey correction for multiple comparisons, no significant differences were measured amongst the dead stains. (n = 3, error bars = standard deviation)

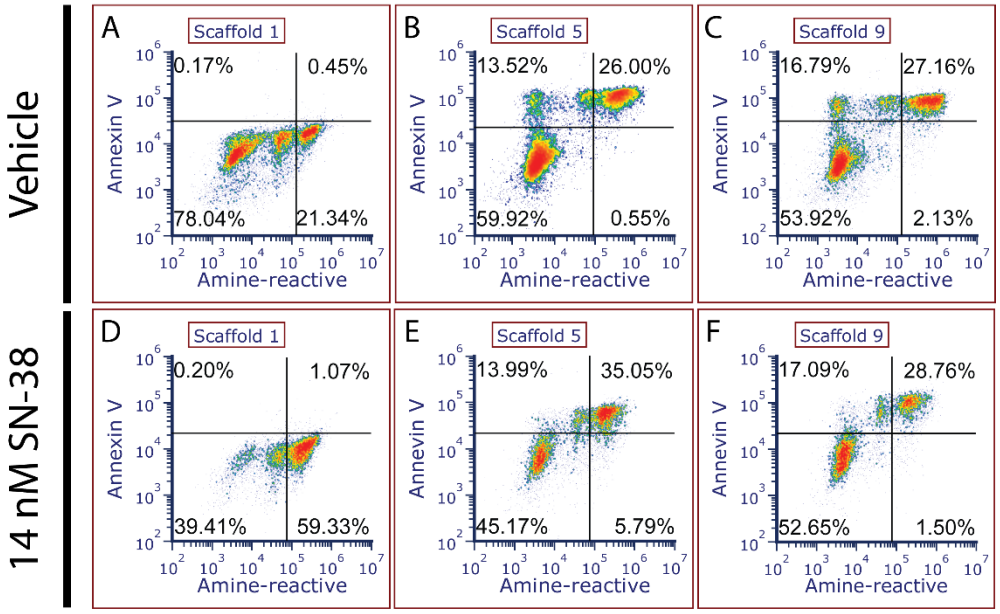

Figure 5.4 Representative cytograms of cell populations extracted from PBCs incubated in either a vehicle control (A-C) or cytotoxic molecule (14 nM SN-38, D-F). Cytograms were taken from scaffolds 1 (A,D), 5 (B,E), and 9 (C,F). Cells in the bottom-left corner were double negatively stained and considered viable. Cells in top-left corner were positively stained for Annexin V and negatively stained with the amine reactive dye; cells in this quadrant were considered apoptotic. Cells in the top- and bottom-right quadrants were positively stained for the amine-reactive dye and were considered dead.

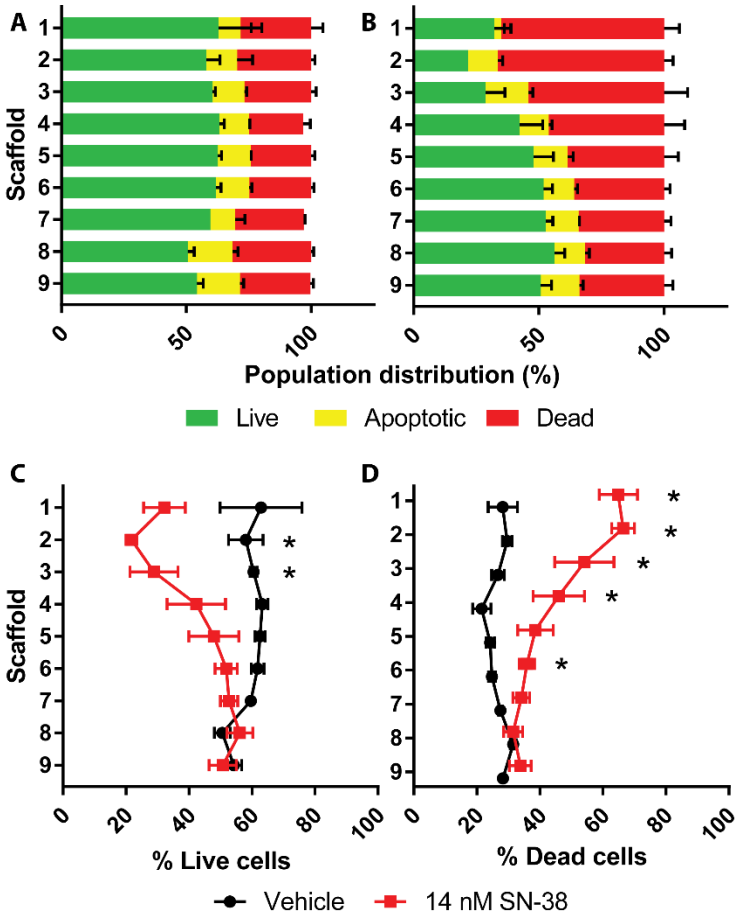

Figure 5.5 Comparison of relative chemosensitivity between stacked PBCs. Live, apoptotic, and dead cell populations were measured via flow cytometry and compared between PBCs incubated in the presence of a (A) vehicle or (B) cytotoxic molecule (14 nM SN-38). Changes in (C) Live and (D) dead cell populations were compared between the normal and dosed cultures to evaluate difference in response relative to placement within the stack. (* = $p < 0.05$, n = 3, error bars = standard deviation)

REFERENCES

(1) Cullen, K. J.; Newkirk, K. A.; Schumaker, L. M.; Aldosari, N.; Rone, J. D.; Haddad, B. R. **2003**, No. 16, 8097–8102.

(2) Cummings, J.; Boyd, G.; Ethell, B. T.; Macpherson, J. S.; Burchell, B.; Smyth, J. F.; Jodrell, D. I. *Biochem. Pharmacol.* **2002**, *63* (4), 607–613.

(3) Xu, Y.; Villalona-Calero, M. A. *Ann. Oncol.* **2002**, *13* (12), 1841–1851.

(4) Gottesman, M. M.; Fojo, T.; Bates, S. E. *Nat. Rev. Cancer* **2002**, *2* (1), 48–58.

(5) Thomas, H.; Coley, H. M. *Cancer Control* **2003**, *10* (2), 159–165.

(6) Rumjanek, V. M.; Trindade, G. S.; Wagner-Souza, K.; De-Oliveira, M. C.; Marques-Santos, L. F.; Maia, R. C.; Capella, M. A. *An. Acad. Bras. Ci.* **2001**, *73* (1), 57–69.

(7) Copur, S.; Aiba, K.; Drake, J. C.; Allegra, C. J.; Chu, E. *Biochem Pharmacol* **1995**, *49* (10), 1419–1426.

(8) Boyer, J.; McLean, E. G.; Aroori, S.; Wilson, P.; McCulla, A.; Carey, P. D.; Longley, D. B.; Johnston, P. G. *Clin. Cancer Res.* **2004**, *10* (6), 2158–2167.

(9) Deffie, A. M.; McPherson, J. P.; Gupta, R. S.; Hedley, D. W.; Goldenberg, G. J. *Biochem. Cell Biol.* **1992**, *70* (5), 354–364.

(10) Jansen, W. J.; Kolfschoten, G. M.; Erkelens, C. a; Van Ark-Otte, J.; Pinedo, H. M.; Boven, E. *Int. J. Cancer* **1997**, *73* (6), 891–896.

(11) Teitz, T.; Wei, T.; Valentine, M. B.; Vanin, E. F.; Grenet, J.; Valentine, V. A.; Behm, F. G.; Look, A. T.; Lahti, J. M.; Kidd, V. J. *Nat. Med.* **2000**, *6* (5), 529–535.

(12) Fulda, S.; Küfer, M. U.; Meyer, E.; Van Valen, F.; Dockhorn-Dworniczak, B.; Debatin, K. M. *Oncogene* **2001**, *20* (41), 5865–5877.

(13) Fink, D.; Aebi, S.; Howell, S. *Clin. Cancer Res.* **1998**, *4* (1), 1–6.

(14) Plumb, J. A.; Strathdee, G.; Sludden, J.; Kaye, S. B.; Brown, R. *Cancer Res.* **2000**, *60*, 6039–6044.

(15) Shirota, Y.; Stoehlmacher, J.; Brabender, J.; Xiong, Y. P.; Uetake, H.; Danenberg, K. D.; Groshen, S.; Tsao-Wei, D. D.; Danenberg, P. V; Lenz, H. J. *J Clin Oncol* **2001**, *19* (23), 4298–4304.

(16) Gordon, R. R.; Nelson, P. S. *Drug Resist. Updat.* **2012**, *15* (1–2), 123–131.

(17) Bunz, F.; Hwang, P. M.; Torrance, C.; Waldman, T.; Zhang, Y.; Dillehay, L.; Williams, J.; Lengauer, C.; Kinzler, K. W.; Vogelstein, B. *J. Clin. Invest.* **1999**, *104* (3), 263–269.

(18) Longley, D. B.; Boyer, J.; Allen, W. L.; Latif, T.; Ferguson, P. R.; Maxwell, P. J.; McDermott, U.; Lynch, M.; Harkin, D. P.; Johnston, P. G. *Cancer Res.* **2002**, *62* (9), 2644–2649.

(19) Chiodi, I.; Belgiovine, C.; Donà, F.; Scovassi, A. I.; Mondello, C. *Cancers (Basel).* **2011**, *3* (1), 1111–1128.

(20) Al-Hajj, M.; Becker, M. W.; Wicha, M.; Weissman, I.; Clarke, M. F. *Curr. Opin. Genet. Dev.* **2004**, *14* (1), 43–47.

(21) Trédan, O.; Galmarini, C. M.; Patel, K.; Tannock, I. F. *J. Natl. Cancer Inst.* **2007**, *99* (19), 1441–1454.

(22) Zahreddine, H.; Borden, K. L. B. *Front. Pharmacol.* **2013**, *4* (28), 1–8.

(23) Boyce, M. W.; LaBonia, G. J.; Hummon, A. B.; Lockett, M. R. *Analyst* **2017**, *142* (15), 2819–2827.

(24) Steff, A. M.; Fortin, M.; Arguin, C.; Hugo, P. *Cytometry* **2001**, *45* (4), 237–243.

(25) Galderisi, F.; Stork, L.; Li, J.; Mori, M.; Mongoue-Tchokote, S.; Huang, J. *J. Clin. Oncol.* **2010**, *53* (4), 543–550.

(26) Gupta, V.; Zhang, Q.-J.; Liu, Y.-Y. *Methods Mol Biol* **2011**, *716* (9), 179–191.

(27) García-Escarp, M.; Martínez-Muñoz, V.; Sales-Pardo, I.; Barquinero, J.; Domingo, J. C.; Marin, P.; Petriz, J. *Cytom. Part A* **2004**, *62* (2), 129–138.

(28) Achuthan, S.; Santhoshkumar, T. R.; Prabhakar, J.; Nair, S. A.; Pillai, M. R. *J. Biol. Chem.* **2011**, *286* (43), 37813–37829.

(29) Oh, C. K.; Lee, S. J.; Park, S. H.; Moon, Y. *J. Biol. Chem.* **2016**, *291* (19), 10173–10183.

(30) Milanovic, M.; Fan, D. N. Y.; Belenki, D.; Däbritz, J. H. M.; Zhao, Z.; Yu, Y.; Dörr, J. R.; Dimitrova, L.; Lenze, D.; Monteiro Barbosa, I. A.; Mendoza-Parra, M. A.; Kanashova, T.; Metzner, M.; Pardon, K.; Reimann, M.; Trumpp, A.; Dörken, B.; Zuber, J.; Gronemeyer, H.; Hummel, M.; Dittmar, G.; Lee, S.; Schmitt, C. A. *Nature* **2018**, *553* (7686), 96–100.

(31) Perfetto, S. P.; Chattopadhyay, P. K.; Lamoreaux, L.; Nguyen, R.; Ambrozak, D.; Koup, R. A.; Roederer, M. *J. Immunol. Methods* **2006**, *313* (1–2), 199–208.

(32) George, T. C.; Basiji, D. A.; Hall, B. E.; Lynch, D. H.; Ortyn, W. E.; Perry, D. J.; Seo, M. J.; Zimmerman, C. A.; Morrissey, P. J. *Cytom. Part A* **2004**, *59A* (2), 237–245.

(33) Coppé, J.-P.; Desprez, P.-Y.; Krtolica, A.; Campisi, J. *Annu. Reveiws Pathol.* **2010**, *5*, 99–118.

(34) Cahu, J.; Sola, B. *J. Vis. Exp.* **2013**, No. 78, 1–6.

(35) Hofmann, J.; Sernetz, M. *Anal. Chim. Acta* **1984**, *163*, 67–72.

(36) Yang, N.; Hu, M. *Anal. Biochem.* **2004**, *325*, 337–343.

(37) Poot, M.; Arttamangkul, S. *Cytometry* **1997**, *28*, 36–41.

(38) Han, Z.; Wei, W.; Dunaway, S.; Darnowski, J. W.; Calabresi, P.; Sedivy, J.; Hendrickson, E. A.; Balan, K. V; Pantazis, P.; Wyche, J. H. **2002**, *277* (19), 17154–17160.

(39) Wilson, T. R.; Longley, D. B.; Johnston, P. G. *Ann. Oncol.* **2006**, *17* (SUPPL. 10), 315–324.

(40) Andeil, L. C.; Ourdier, I. G.; Eyron, D. P.; Ezzio, N. V; Opois, V. C.; Ibeau, F. B.; Rsetti, B. O.; Cheffer, G. L. S.; Chou, M. Y.; Han, Q. A. K.; Ommier, Y. P.; Au, B. P.; Artineau, P. M.; Io, M. D. E. L. R. *Int. J. Cancer* **2004**, *109*, 848–854.

(41) Strouse, J. J.; Ivnitski-steele, I.; Waller, A.; Young, S. M.; Perez, D.; Evangelisti, A. M.; Ursu, O.; Bologa, C. G.; Carter, M. B.; Salas, V. M.; Tegos, G.; Larson, R. S.; Oprea, T. I.; Edwards, B. S.; Sklar, L. A. *Anal. Biochem.* **2013**, *437*, 77–87.

(42) Wolosin, J. M.; Zamudio, A.; Wang, Z. *PLoS One* **2017**, *12* (4), 1–19.

APPENDIX A: SUPPLEMENTAL INFORMATION FOR CHAPTER 2

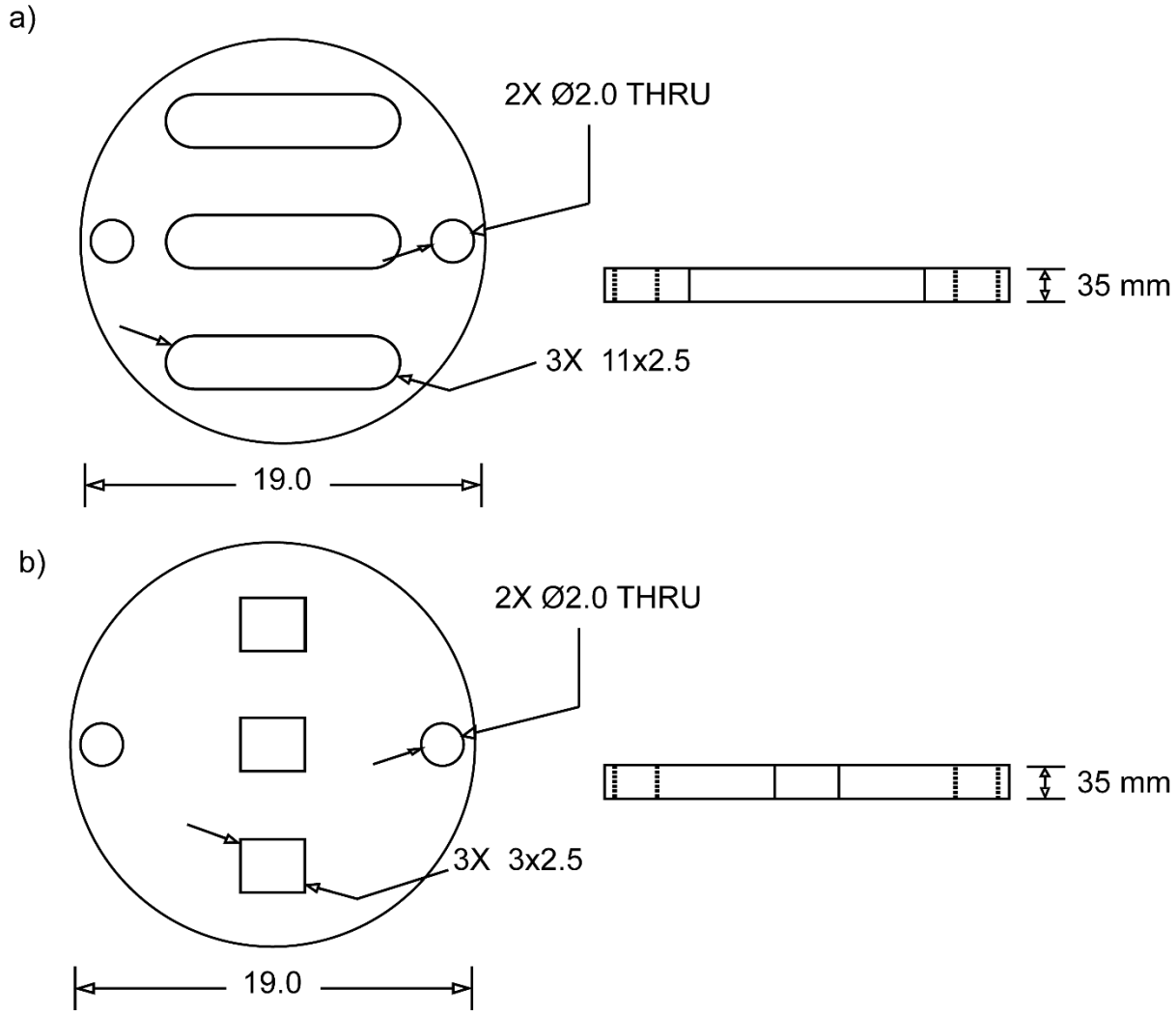

Figure A2.1 A schematic of paper-based scaffolds used in the oxygen sensing experiments. a) Each channel of the channel scaffolds was filled with Matrigel prior to culture assembly. b) Cells suspended in Matrigel were seeded in each rectangular zone of the imprint scaffold. These rectangular zones allowed us to reproducibly seed cells. The two 2.0 mm holes were used to assist in culture assembly. Designs were prepared in Abode Illustrator. Unless otherwise stated, all units are in millimeters.

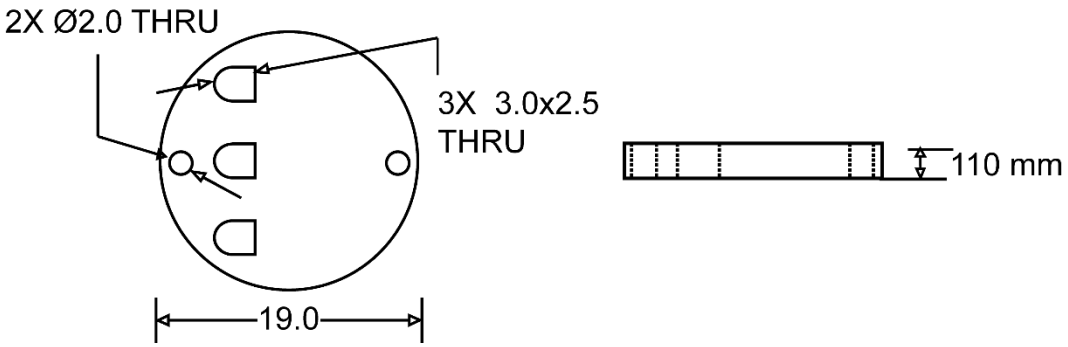

Figure A2.2 A schematic of the cellulose acetate sheet design used in the oxygen sensing experiments. The three 3.0 x 2.5 mm openings allow for exchange between fresh culture medium and the cell-containing paper scaffold. The two 2.0 mm openings are used to assist in assembly. Designs were prepared in Abode Illustrator. Unless otherwise stated, all units are in millimeters.

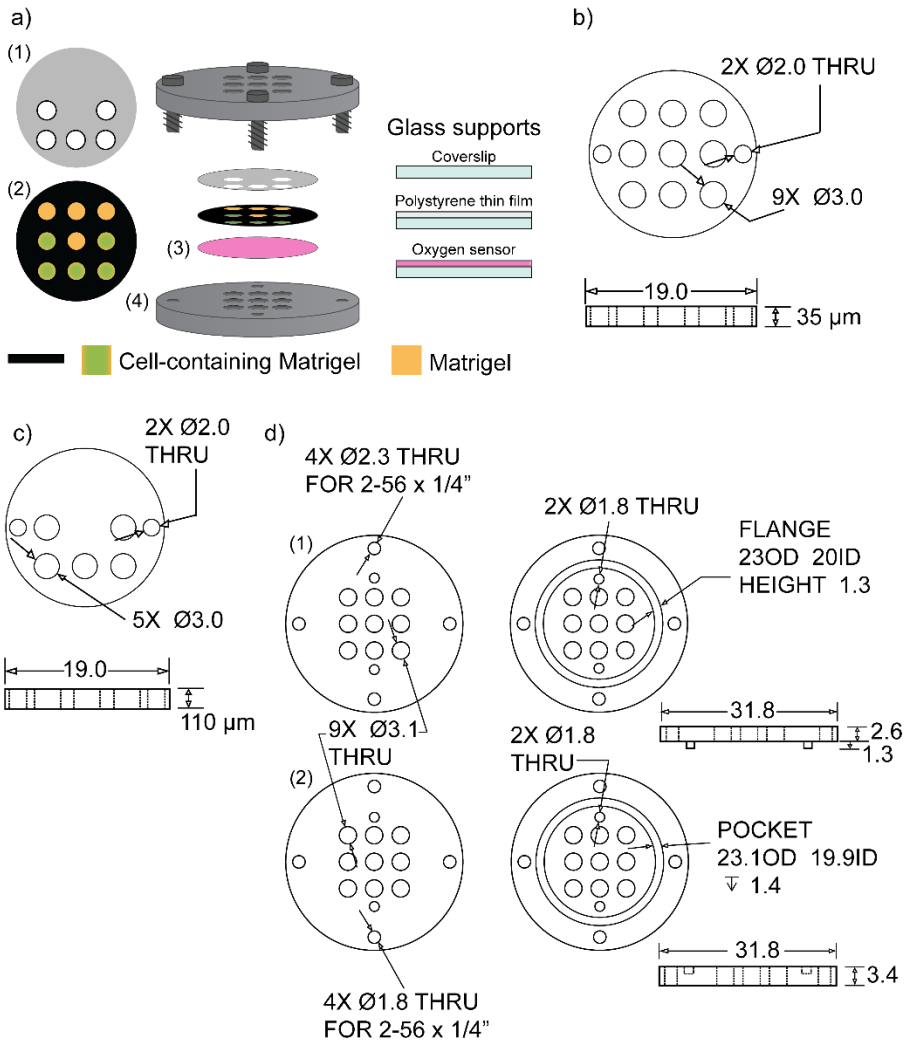

Figure A2.3 Schematic of the experimental setup and components used for cytotoxicity experiments. a) The experimental setup for measuring cytotoxicity. A (1) cellulose acetate sheet with openings to allow for free exchange between medium and seeded cells was placed on top of a (2) paper-based scaffold, which had cells seeded along 5 circular zones and cell-free Matrigel in the reaming zones. A (3) glass support was placed at the bottom of the stack, and was either a coverslip, a coverslip with a polystyrene thin film, of an oxygen sensor. The entire stack was then enclosed in a (4) custom stainless-steel holder. Scale bar = 9 mm. b) Schematic of the scaffolds used for cytotoxicity measurements. Five of the nine zones were seeded with cell-suspended Matrigel and the remaining four were filled with Matrigel. c) Schematic of the cellulose acetate sheet used for the cytotoxicity assay. The sheets had five 3 mm circular openings, which overlapped with regions in the paper-based scaffold where cells were seeded. d) Schematic of the holders used to enclose the paper-based cultures for cytotoxicity measurements. The holder's (1) top and (2) bottom halves interlock through a flange along the top half, and the nine 3.0 mm circular holes allow for medium to reach the paper scaffolds while assembled. Holders were held together with four 2-56 x ¼" screws, and the two 1.8 mm holes were used to assist in assembly. Designs were prepared in Abode Illustrator. Unless otherwise stated, all units are in millimeters.

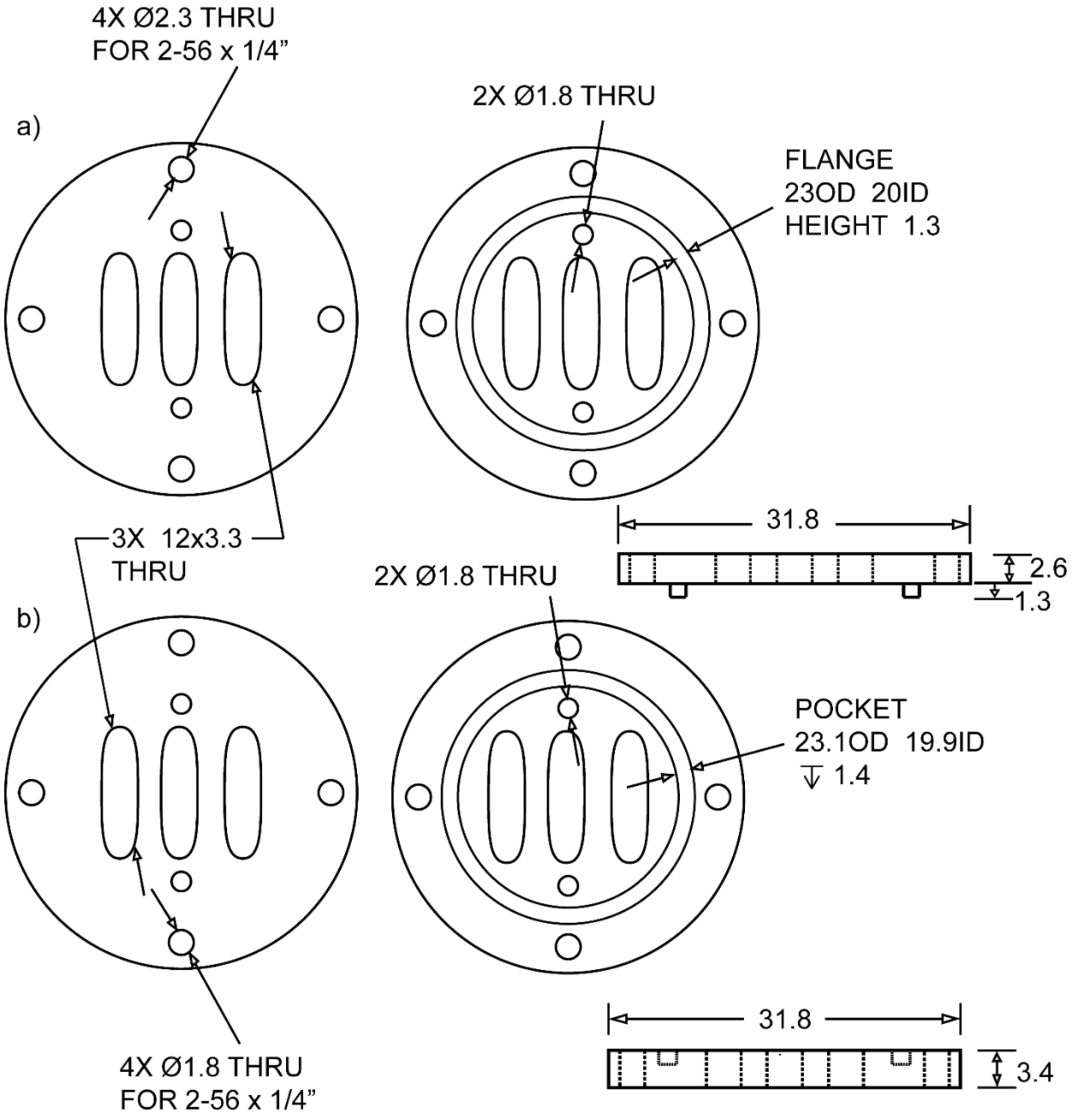

Figure A2.4. Schematic of the stainless-steel holders used to enclose the paper-based cultures. The holder's (a) top and (b) bottom halves interlock through a flange along the top half, and the three 12 x 3.3 mm openings present on each half allowed for visualization of the channels in the paper-based scaffolds when the holder is assembled. Holders were secured with a four 2-56 x ¼" screws, and the two 1.8 mm holes were used to assist in assembly. Designs were prepared in Abode Illustrator. Unless otherwise stated, all units are in millimeters.

APPENDIX B: SUPPLEMENTAL INFORMATION FOR CHAPTER 3

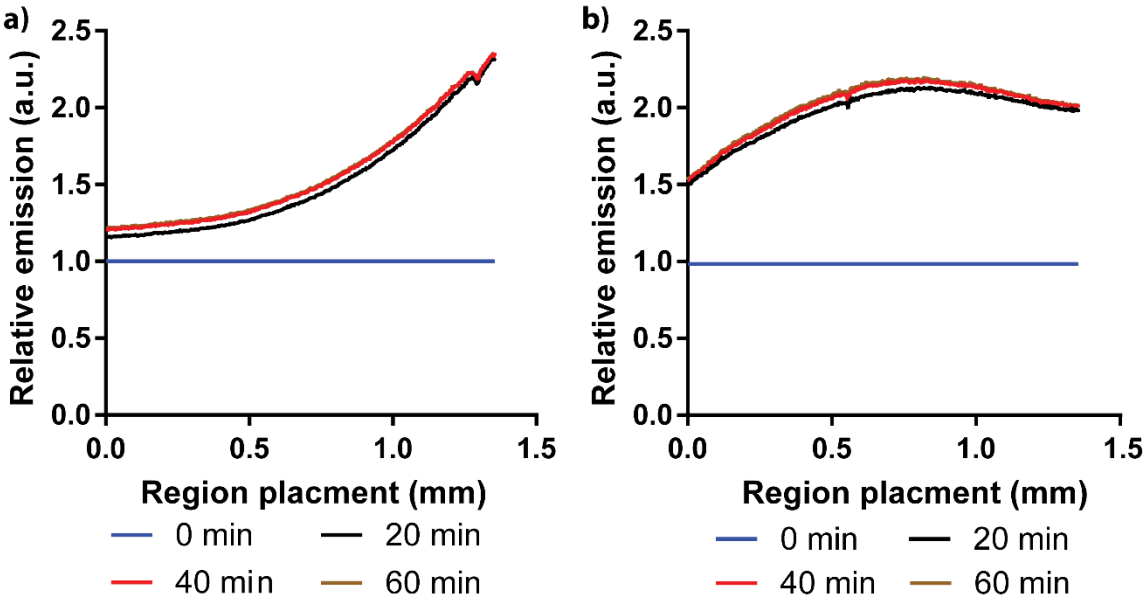

Figure B3.1. Equilibration times for generating stable oxygen gradients in the BLOCCs. Oxygen gradients were generated by flowing (a) 20% or (b) 5% O_2 gas mixtures through one channel of the left fluidic channel and a 0% O_2 gas mixture through the right channel. Emission intensities represent plot profiles parallel to the oxygen gradients as imaged directly from the oxygen sensing films, and were normalized to the initial reading at ambient conditions. Both gas mixtures reached equilibrium within 60 min.

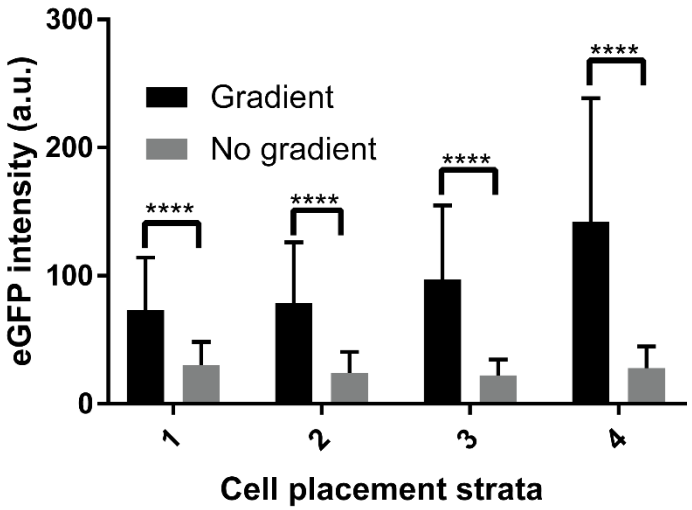

Figure B3.2 BLOCCs incubated with under an oxygen gradient exhibit increased eGFP expression across all strata of the chip. The average center-point intensity values of eGFP were compared between BLOCCs incubated with an oxygen gradient or under ambient oxygen conditions. All strata in the BLOCCs experiencing an oxygen gradient had significantly higher eGFP intensity, which corresponds to an increase in hypoxia response. (error bars = standard deviation, **** = $p < 0.0001$)

APPENDIX C: SUPPLEMENTAL INFORMATION FOR CHAPTER 4

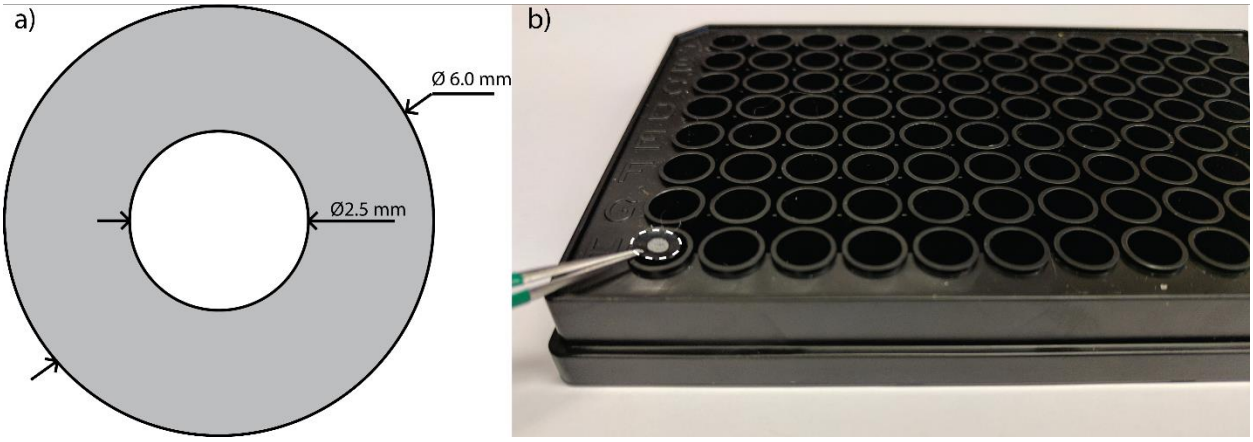

Figure C4.1 a) Schematic of single-zone scaffolds, prepared using previously described protocols.[1] Each circular scaffold is 6 mm in diameter with a 2.5 mm diameter zone for seeding cells. The grey color corresponds to the wax-patterned region of the scaffold. b) Photograph of the single-zone scaffold (white outline) being placed into the well of a 96-well plate.

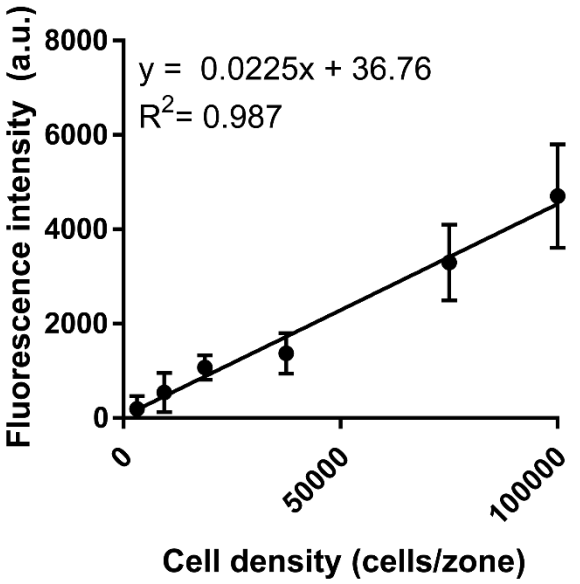

Figure C4.2 Calibration curve relating mCHR fluorescence intensity to number of the number of HCT116 mCHR cells in a zone of a paper-based scaffold, imaged with a Typhoon 9400 scanner. These measurements utilized scaffolds patterned with the 9-zone format: five zones contained 0.5 µL of cell-laden Matrigel with increasing densities of HCT 166 mCHR cells, the remaining four zones contained 0.5 µL of cell-free Matrigel. Each point on the curve represents the average and standard deviation of n = 5 zones.

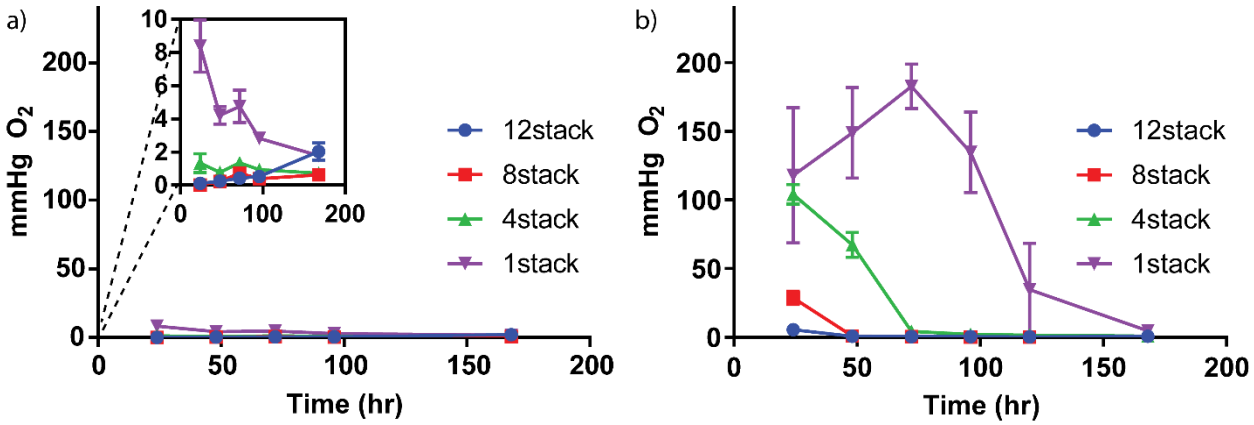

Figure C4.3 Oxygen tensions at the bottom of stacked cultures containing 1, 4, 8, or 12 scaffolds. These cultures were seeded at cell densities of either a) 84,000 cells/zone or b) 21,000 cells/zone, and incubated for up to 168 h. The inset of a) is to better visualize differences in oxygen tension for cultures with 84,000 cell/zone. Each point represents the average and standard deviation of n = 5 measurements from the same experimental setup.

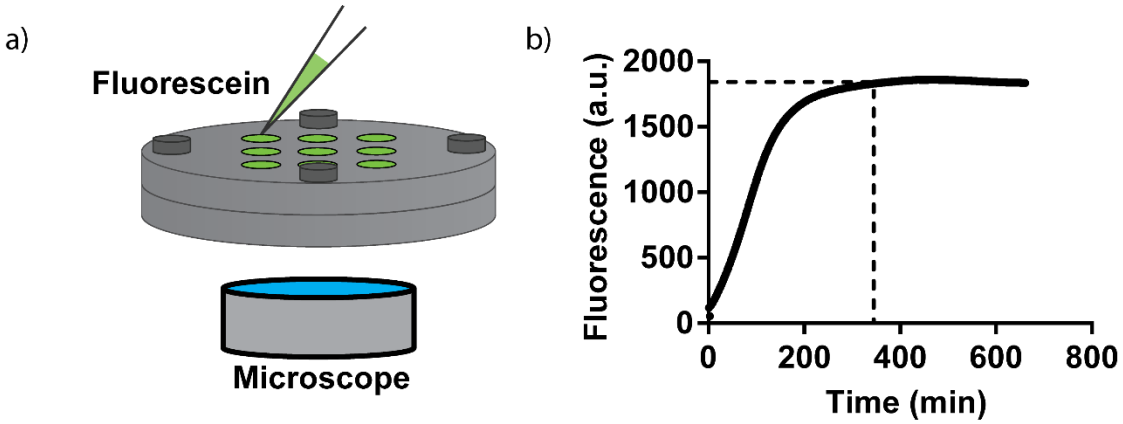

Figure C4.4 Measuring the penetration of fluorescein into stacked paper-based cultures (PBCs) using fluorescence microscopy. a) Experimental setup. A 12-stack PBC culture was assembled, 100 µL of a 0.5 mg/mL fluorescein was added to the top of each culture, and images of the bottom collected with an inverted fluorescence microscope. b) Fluorescence intensity at the bottom over an 11 h incubation period at 37 ºC. Images were collected in 1-minute increments. The constant fluorescence intensity after ~350 minutes indicates that an equilibrium in fluorescein had been reached.

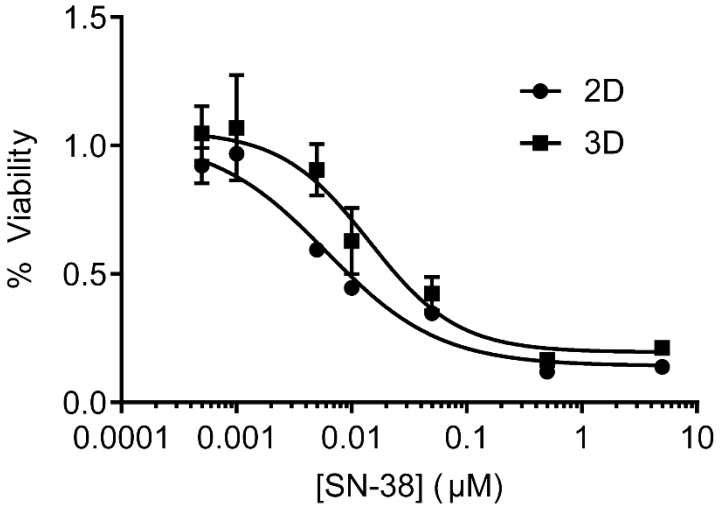

Figure C4.5 Dose-response curves for SN-38 treatment of HCT116 mCHR cells in 2D and 3D cultures. Doses of SN-38 were administered at increasing concentrations to adherent (2D; 5,000 cells/well) and Matrigel-suspended (3D; 20,000 cells/zone) HCT116 mCHR cells. The resulting IC_{50} values for 2D and 3D conditions were 0.006±0.001 and 0.014±0.006, respectively. Each point represents the average and standard error of the mean of n = 4 measurements.

Table C4.1: Statistical comparisons between mCHR fluorescence intensity of cultures seeded at 84,000 cells/zone and dosed with different concentrations of SN-38.[a]

	Vehicle vs.			1.4 µM vs.		0.14 µM vs.
Scaffold[b]	1.4 µM	0.14 µM	0.014 µM	0.14 µM	0.014 µM	0.014 µM
1	****	-	-	****	****	*
2	****	****	****	**	***	-
3	****	****	****	****	*	-
4	****	****	****	-	-	-
5	****	**	**	-	-	-
6	-	-	-	-	-	-
7	-	-	-	-	-	-
8	-	-	-	-	-	-
9	-	-	-	-	-	-
10	-	-	-	-	-	-
11	*	-	-	-	-	-
12	-	-	*	-	-	-

[a] The comparisons in this table correspond to the data presented in **Figure 4.4a** of the main text. (* = $p < 0.05$, ** = $p < 0.01$, *** = $p < 0.001$, **** = $p < 0.0001$)

[b] Scaffold 1 was closest to the source of fresh medium, and scaffold 12 was the furthest from the source of fresh medium.

Table C4.2: Statistical comparisons between mCHR fluorescence intensity of cultures seeded at 21,000 cells/zone and dosed with different concentrations of SN-38.[a]

	Vehicle vs.		1.4 µM vs.
Scaffold[b]	1.4 µM	0.014 µM	0.014 µM
1	****	****	**
2	****	-	****
3	****	-	*
4	****	-	****
5	**	-	****
6	*	-	****
7	-	-	*
8	**	-	*
9	**	-	**
10	-	-	-
11	***	-	****
12	-	-	-

[a] The comparisons in this table correspond to the data presented in **Figure 4.4b** of the main text. (* = $p < 0.05$, ** = $p < 0.01$, *** = $p < 0.001$, **** = $p < 0.0001$)

[b] Scaffold 1 was closest to the source of fresh medium, and scaffold 12 was the furthest from the source of fresh medium.